The SASKTRAN Thermal Infrared Radiative Transfer Model with Analytic Jacobian Calculations

A Thesis Submitted to the

College of Graduate and Postdoctoral Studies

in Partial Fulfillment of the Requirements

for the degree of Master of Science

in the Department of Physics and Engineering Physics

University of Saskatchewan

Saskatoon

By

Taran Warnock

Permission to Use

In presenting this thesis in partial fulfilment of the requirements for a Postgraduate degree from the University of Saskatchewan, I agree that the Libraries of this University may make it freely available for inspection. I further agree that permission for copying of this thesis in any manner, in whole or in part, for scholarly purposes may be granted by the professor or professors who supervised my thesis work or, in their absence, by the Head of the Department or the Dean of the College in which my thesis work was done. It is understood that any copying or publication or use of this thesis or parts thereof for financial gain shall not be allowed without my written permission. It is also understood that due recognition shall be given to me and to the University of Saskatchewan in any scholarly use which may be made of any material in my thesis.

Requests for permission to copy or to make other use of material in this thesis in whole or part should be addressed to:

Head of the Department of Physics and Engineering Physics

163 Physics Building, 116 Science Place

University of Saskatchewan

Saskatoon, Saskatchewan S7N 5E2 Canada

Or

Dean

College of Graduate and Postdoctoral Studies

University of Saskatchewan

116 Thorvaldson Building, 110 Science Place

Saskatoon, Saskatchewan S7N 5C9 Canada

Abstract

The SASKTRAN radiative transfer framework is a set of software tools for modelling the propagation of electromagnetic radiation through the atmosphere. It is an important tool in modelling the measurements made by remote sensing instruments in order to retrieve information about the structure and composition of the atmosphere from observations of spectral radiance. The primary goals of this thesis are to expand the capabilities of SASKTRAN to modelling the infrared spectral regime and test this new suite of modelling software for use with real atmospheric remote sensing data. This model will be used to retrieve information on the concentrations of greenhouse gases from measurements made by the Limb Imaging Fourier transform spectrometer Experiment (LIFE), a remote sensing instrument developed at the University of Saskatchewan.

The Thermal InfraRed (TIR) model, developed in this thesis, incorporates the absorption and emission of radiation from greenhouse gases to solve the radiative transfer problem. The fundamental output of this model is the spectral radiance that is incident on an observer positioned at a given location and looking in a given direction through the atmosphere. Radiative transfer is a non-linear problem and complex inverse methods are needed to determine atmospheric composition from instrument measurements. The inversion requires the computation of Jacobians, which quantify how the spectral radiance changes when changes are made to the atmospheric state parameters. Analytic Jacobian calculations are implemented in the TIR model and simultaneously calculated alongside the modelled radiance. With analytic calculations significant computational savings are achieved because the model does not need to be executed for each parameter that is changed. The TIR model supports the computation of analytic Jacobians for vertical profiles of greenhouse gas composition and temperatures.

Fourier Transform Spectrometers (FTS) measure interferograms of light that are converted into radiances via Fourier transform. LIFE employs the FTS technique to measure vertical images of atmospheric spectral radiance in the thermal infrared regime. This instrument is a primary motivation for the development of the TIR model, which is to be implemented to retrieve information about the vertical composition of greenhouse gases such as methane, water vapor, ozone, and nitrous oxide. In this thesis the TIR model is used

to simulate LIFE measurements and demonstrate the feasibility of retrieving greenhouse gas profiles with the aid of analytic Jacobian calculations.

ACKNOWLEDGEMENTS

CONTENTS

List of Tables

LIST OF FIGURES

LIST OF ABBREVIATIONS

AFGL	Air Force Geophysics Laboratory
API	Application Programming Interface
ARTS	Atmospheric Radiative Transfer Simulator
BRDF	Bidirectional Reflectance Distribution Function
CSA	Canadian Space Agency
ECMWF	European Centre for Medium-range Weather Forecasts
FOV	Field of View
FTS	Fourier Transform Spectrometer
GLORIA	Gimballed Limb Observer for Radiance Imaging of the Atmosphere
GOSAT	Greenhouse gases Observing SATellite
HITRAN	HIgh-resolution TRANsmission molecular absorption
HWHM	Half Width at Half Maximum
ILS	Instrument Line Shape
KOPRA	Karlsruhe Optimized and Precise Radiative transfer Algorithm
LIFE	Limb Imaging Fourier transform spectrometer Experiment
LOS	Line of Sight
LTE	Local Thermodynamic Equilibrium
MCT	Mercury Cadmium Telluride
MIPAS	Michelson Interferometer for Passive Atmospheric Sounding
MLS	Microwave Limb Sounder
MPD	Maximum Path Difference
MSIS	Mass Spectrometer and Incoherent Scatter radar
NESR	Noise Equivalent Spectral Radiance
OPD	Optical Path Difference
OSIRIS	Optical Spectrograph and InfraRed Imaging System
SASKTRAN-HR	SASKTRAN High Resolution engine
SASKTRAN-TIR	SASKTRAN Thermal InfraRed engine
SZA	Solar Zenith Angle
TIR	Thermal InfraRed
UTLS	Upper Troposphere and Lower Stratosphere
VMR	Volume Mixing Ratio
WGS	World Geodetic System
ZPD	Zero Path Difference

1 INTRODUCTION

Remote sensing instruments play an important role in research of the structure, composition, and dynamics of Earth's atmosphere. Obtaining accurate knowledge of the quantities of greenhouse gases such as methane and carbon dioxide makes it possible to establish links to climate change. Greenhouse gases absorb and emit radiation with spectral signatures that are unique to each molecular species. The technique of Fourier transform spectroscopy (FTS) has been developed to observe these signatures in the infrared regime. An FTS measures interference patterns of light which can be converted into spectral radiances through Fourier transforms. The Michelson Interferometer for Passive Atmospheric Sounding (MIPAS) is one of the pioneering implementations of a satellite-based FTS for observing thermal emissions through the atmospheric limb (Endemann, 1999). Airborne remote sensing instruments such as MIPAS look through the atmospheric region between the surface of the Earth and outer space, referred to as the *limb*. The limb measurement technique is useful in determining the vertical structure of atmospheric constituents.

Recent experiments have employed advancements in detector technology to obtain more detailed measurements using the FTS technique. The Gimballed Limb Observer for Radiance Imaging of the Atmosphere (GLORIA) utilized a two dimensional array of detectors to simultaneously image across multiple altitudes and horizontal look directions (Riese et al., 2014). GLORIA provided inspiration for the development of the Limb Imaging FTS Experiment (LIFE). LIFE, developed at the University of Saskatchewan through a collaboration with the Canadian Space Agency (CSA) and ABB Canada, is designed for imaging the atmospheric limb from a high altitude balloon (Runge, 2018). The primary goals of the LIFE project are to develop an infrared imaging FTS at a reduced cost while obtaining precise measurements at a high spatial and temporal resolution. In the future LIFE will be adapted to measure the limb from a satellite in space, allowing for measurements over a much greater area.

Development of LIFE is a large project with a core team comprised of three graduate students, one postdoctoral researcher, two faculty members, and one research staff member. The prototype LIFE instrument launched on a stratospheric balloon in September 2019 from Timmins, Ontario and successfully obtained measurements. Processing and analysis of the measurements is the subject of ongoing work, with the contents of this work providing the modeling foundation upon which to begin retrieving atmospheric quantities.

An essential component in the analysis of remote sensing atmospheric experiments is a forward model capable of simulating the measurements of an instrument. Remote sensing instruments typically measure the intensity of light as a function of a spectral unit such as wavelength, wavenumber, or frequency. The goal is to obtain information about the structure and composition of the atmosphere from these measurements. However, the atmospheric radiative transfer problem is fundamentally non-linear, making it generally difficult to directly solve for the desired quantities. Instead, the measurements are recreated by a forward model and techniques of inversion theory are applied to determine the atmospheric state. Often this process involves multiple iterations of the forward model until convergence is achieved. The forward model consists of a radiative transfer model and an instrument model. Given information about the contents and structure of the atmosphere, a radiative transfer model describes the electromagnetic radiation seen from an observation position. The instrument model transforms this radiance to resemble the measurements at the precision and resolution of the instrument in question.

The SASKTRAN radiative transfer framework, developed at the University of Saskatchewan, provides a forward model which has been used to retrieve vertical distributions of ozone and aerosols from measurements in the ultraviolet (UV) and visible regimes (Bourassa et al., 2008). It was primarily developed for use with data from the Optical Spectrograph and InfraRed Imaging System (OSIRIS), an instrument which measures scattered sunlight through the atmospheric limb (Bourassa et al., 2007). SASKTRAN is described as a framework meaning that the software package is structured so that new features and algorithms can be easily implemented as standalone components. The primary components are *engines* which execute the radiative transfer model but utilize different algorithms to account for various factors such as the physics of different spectral regimes, the geometry of a measurement, or

the required accuracy.

Currently, SASKTRAN contains engines that are intended for use with UV and visible radiance measurements. Supporting data analysis for LIFE requires the addition of a new engine, optimized for the thermal infrared regime. This new engine, the SASKTRAN Thermal InfraRed (TIR) engine is the subject of this work. This engine is designed for TIR measurements at wavelengths in the 7 to 14 μm range where LIFE measures. In this regime, solar scattering is negligible and the observed radiation is mostly the result of thermal emissions from greenhouse gases.

1.1 Outline

Chapter 2 begins with the background knowledge required for the development of the TIR engine. It provides an overview of the radiative transfer problem in both the visible and thermal spectroscopic regimes. A description of the spectral structure of emission and absorption by greenhouse gases is performed and its implementation detailed. The algorithm developed for the TIR engine is described and tested in Chapter 3 where the engine is compared with established models to verify its accuracy. Chapter 4 details the implementation of analytic Jacobian calculations in the TIR engine. Jacobians are calculations of the derivatives of the model output with respect to atmospheric parameters, such as temperature or a greenhouse gas density. Computing Jacobians analytically is important for vastly reducing the computational resources required to retrieve atmospheric quantities from radiance measurements. The TIR engine is implemented as a forward model of the LIFE instrument in Chapter 5. In this chapter, the feasibility of retrieving target parameters from simulated LIFE measurements is investigated with the goal of providing a framework for future retrievals from real data. Chapter 6 provides a summary of the model capabilities and results as well as an overview of the future research projects that will make use of this model.

2 Background

2.1 The Earth's Atmosphere

Studying the composition of Earth's atmosphere is an important step in developing a greater understanding of the physical and chemical processes that govern its structure. This research makes it possible to study dynamic weather processes as well as climate change and the effects of anthropogenic pollution. In this section the fundamentals of atmospheric science are reviewed, starting with the structure of the atmosphere, then concepts that are of particular importance in the infrared regime, such as the greenhouse effect, are discussed. Lastly, remote sensing techniques for measuring atmospheric composition are described.

2.1.1 Structure and Composition

Earth's atmosphere is divided into four main regions, based on the variations in temperature with respect to altitude. From lowest to highest altitude the layers are the troposphere, stratosphere, mesosphere, and thermosphere. This structure is illustrated in Figure 2.1.

The troposphere is the layer extending from the surface to an altitude around 15 or 20 km. This region is where most weather systems develop because it contains the majority of the atmosphere's water vapour, facilitating the development of clouds. The troposphere is mainly heated by radiation from the Earth's surface. As the heated air rises the decreasing atmospheric pressure causes it to expand and cool. Therefore, the temperature in the troposphere decreases as height increases. The top of troposphere is known as the tropopause and it is defined as the altitude at which temperature is no longer decreasing with height.

The stratosphere is the layer extending from the tropopause to approximately 50 km. In this region, temperature increases with height due to the absorption of ultraviolet light by the ozone layer, with the density of ozone molecules reaching a maximum in the 20 to 30 km
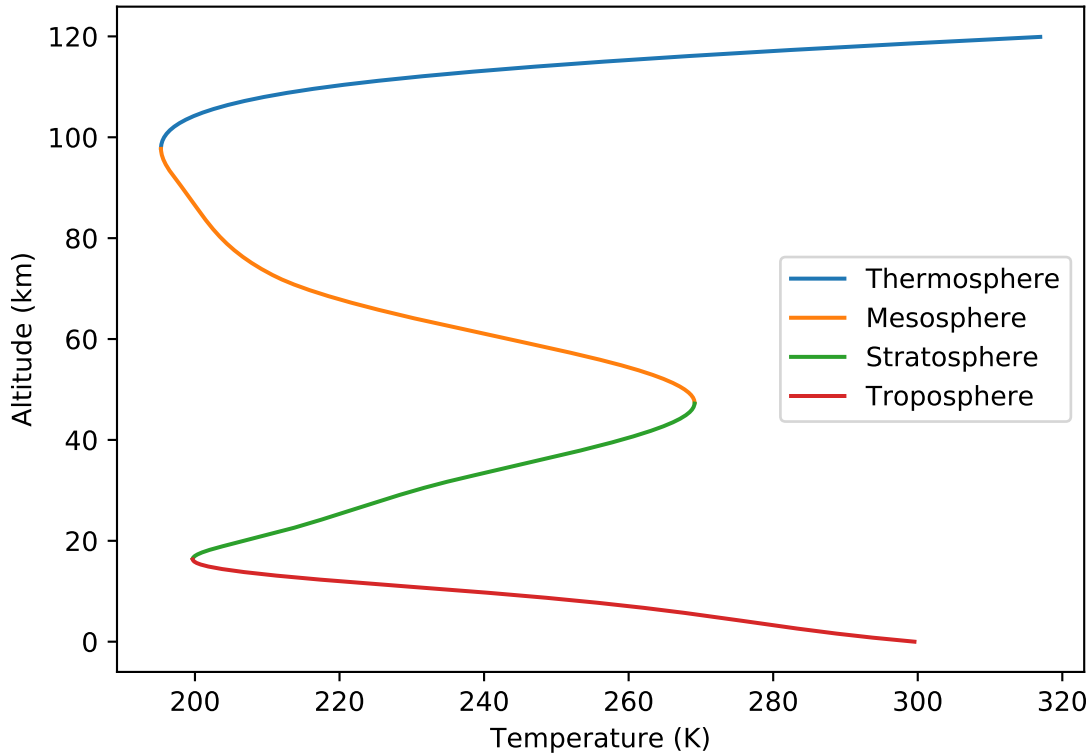
Figure 2.1: Layers of the atmosphere demonstrated using a typical temperature profile from the MSIS-90 atmospheric model (Hedin, 1991).

region. Ultraviolet radiation arrives from the sun at the top of the stratosphere, resulting in more absorption and larger temperatures at higher altitudes. The altitude where temperature ceases to increase with height is defined as the stratopause.

The mesosphere is the region above the stratopause, and reaches to an altitude of approximately 100 km. In this layer temperature decreases with height as a result of cooling from carbon dioxide radiation and because warming from ultraviolet absorption is insignificant as a result of lower ozone density. Similarly, the top of the mesosphere is called the mesopause and defines the point where temperature begins to increase with height again. The region above this point is the thermosphere, in which temperature increases with altitude before eventually reaching a constant value around 250 km.

The Upper Troposphere and Lower Stratosphere (UTLS) is a region that is given special designation due its impact on the global climate. Study of the UTLS structure and compo-

sition from instrument measurements is important for research on climate change and the impact of human pollution. In particular, changes in the concentration of greenhouse gases such as ozone and water vapour is known to change the radiative balance of the planet (Riese et al., 2005).

2.1.2   Radiative Balance and the Greenhouse Effect

Radiative balance describes the thermal equilibrium of the Earth in terms of incoming and outgoing radiative energy. To maintain equilibrium, the Earth must lose radiative energy at the same rate that it is acquired. The incoming energy arrives in the form of solar radiation which is dominated by wavelengths in the ultraviolet, visible, and near infrared regions. While much of the ultraviolet light is absorbed by ozone in the stratosphere, the majority of visible and near infrared light reaches the surface, where it is either absorbed or reflected. Light that is reflected travels back through the atmosphere into space, with no net effect on the Earth's energy balance.

Earth can be modelled as a black body that radiates isotropically with an average surface temperature. The surface temperature of the Earth is much lower than the 5772 K effective temperature of the Sun, and therefore most of the emitted radiation is at lower energy infrared wavelengths (Williams, 2016). Without an atmosphere, radiative processes result in a mean global temperature of 254 K, for which the derivation is described in Appendix A. However, the actual surface temperature is much warmer due to the presence of atmospheric species that absorb and re-radiate the longwave infrared radiation emitted from the surface. The radiation re-emitted primarily from particles in the lower atmosphere results in a net warming effect at the Earth's surface, known as the greenhouse effect. Likewise, the absorbing species are called greenhouse gases, and the warming caused by their interaction with infrared radiation results in a global surface temperature of approximately 288 K (Williams, 2016).

Over long periods of time the average temperature can change due to changes in the global radiative forcing, which describes the difference between incoming and outgoing radiative energy. An increase in radiative forcing results in a global warming and increase in the mean temperature. This warming is largely the result of increased concentrations of greenhouse gases with carbon dioxide, methane, and nitrous oxide being three of the largest

contributors to radiative forcing (Joos and Spahni, 2008). Water vapour also has a significant effect on radiative forcing in the troposphere. Due to the impact of these species on climate change and the recent increase in anthropogenic emissions, it is important to obtain accurate measurements of atmospheric composition to improve the understanding of atmospheric processes and structure.

2.1.3 Infrared Remote Sensing

Remote sensing instruments provide valuable information about the composition of the atmosphere by measuring the light that is scattered, absorbed, or emitted by gaseous particles. These instruments are capable of performing observations from distant locations, making it easier to obtain measurements covering large areas in comparison to local in situ measurements. Instruments may be placed on a variety of platforms including satellites and high altitude balloons or aircraft. Observations from satellites make it possible to measure a large area and achieve global coverage, while measurements from balloons and aircraft allow for measurements with better spatial resolution. These factors are important considerations for research missions, along with the higher budgets and development times required for satellite missions.

A measurement taken from a particular time and location with an instrument pointed in a particular direction is called a *line of sight* or *viewing geometry*. There are three main viewing geometries used to measure atmospheric composition. The first type is a nadir geometry, in which the instrument is pointed directly towards the ground, with a vertical or nearly vertical line of sight. Nadir measurements are preferred when high spatial resolution in the horizontal direction is desired. However, the vertical resolution is limited because each line of sight passes through the entire vertical extent of the atmosphere. For this reason, nadir measurements are often used to retrieve column densities of atmospheric species. An example is the Greenhouse Gases Observing Satellite (GOSAT) which has a spatial resolution of 0.5 km and whose measurements have been used to determine dry air mole fractions of carbon dioxide and methane (Yokota et al., 2009). Nadir lines of sight intersect the ground which has a significant impact on the signals these instruments measure. At visible wavelengths sunlight is reflected from the surface into the instrument line of sight, while at infrared wavelengths

the thermal emissions from the surface have a more significant effect.

Limb-viewing geometry is the second atmospheric observation technique. A limb measurement is performed by looking through the *limb* of the atmosphere, such that the line of sight does not reach the ground, but instead extends from the observer through the atmosphere and into space. The limb geometry is characterized by its tangent altitude, which is the lowest altitude reached by the line of sight where the line is tangent to the surface of the earth. This geometry is demonstrated in Figure 2.2. The line of sight covers a large horizontal distance, resulting in lower horizontal resolution than a nadir geometry. However, vertical resolution is greatly improved which makes limb measurements ideal for determining vertical profiles of atmospheric species and studying the different regions of the atmosphere. High vertical resolution is possible due to the exponential decrease in air particle density. In general, a limb measurement depends largely on the concentration of species near the tangent altitude. At visible wavelengths, the primary contribution to limb-viewing measurement is light scattered from atmospheric particles. At infrared wavelengths, the signal is mainly due to thermal emissions from greenhouse gases.

For example, the The Michelson Interferometer for Passive Atmospheric Sounding (MIPAS) is a satellite instrument that is capable of infrared limb measurements with a vertical resolution as small as 3 km (Endemann, 1999). The technique of measuring light using interferometers and converting them to spectra using Fourier transforms is common in infrared sounding as opposed to the diffraction grating spectrometers used in the ultraviolet and visible light regimes by instruments such as OSIRIS (Llewellyn et al., 2004). See Section 2.4.1 for an overview of the Fourier transform spectrometer (FTS). Similar to other limb experiments like OSIRIS, MIPAS constructs a measurement profile by scanning vertically through the atmosphere.

Recent instruments have taken advantage of advances in infrared detector technology to create imaging systems that capture simultaneous measurements over a range of tangent altitudes instead of scanning. An imaging instrument can obtain profiles with less horizontal extent than scanning instruments because all tangent altitudes are measured instantly while a scanning instrument can travel large distances during a single scan. The Gimballed Limb Observer for Radiance Imaging of the Atmosphere (GLORIA) contains a two-dimensional
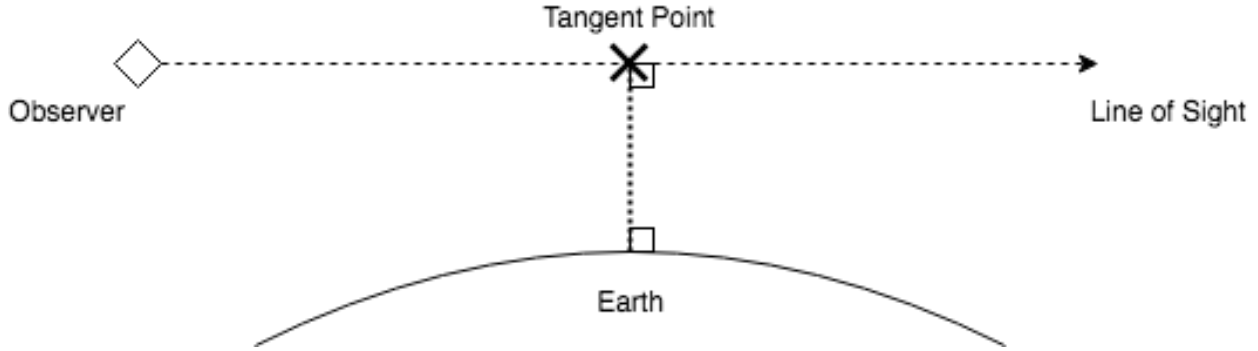
Figure 2.2: The limb viewing geometry for atmospheric remote sensing. The tangent point is located where the line of sight is parallel to the surface of the Earth and reaches its lowest altitude.

detector array that captures light interferograms on 128 vertical pixels and 48 horizontal pixels (Riese et al., 2014) at once. From a high altitude aircraft, GLORIA is able to obtain vertical resolutions as good as 300 m and a horizontal resolution of 20 km. Improving the horizontal resolution helps address one of the primary disadvantages of the limb-viewing technique.

The third viewing type is solar occultation, which is a specific case of a limb geometry in which the instrument is looking through the atmosphere directly at the sun. In this geometry, instruments measure the extinction of sunlight due to scattering and absorption along the line of sight. The primary advantage of this geometry is the increase in signal intensity with a major drawback being that occultation is only possible at sunrise and sunset in order for lines of sight through the limb to be directed towards the sun. Therefore, measurements may only be performed twice per orbit, making it difficult and more time consuming to achieve global coverage.

2.2   Radiative Transfer

To determine the physical composition of a medium from remote sensing measurements, it is necessary to understand the behaviour of light as it propagates through the atmosphere. In radiative transfer theory, this problem is formulated by solving for the spectral radiance observed at a particular point in space while looking through a medium, such as the atmosphere, in a given direction. Spectral radiance describes the electromagnetic energy per

unit time, area, and solid angle moving through a point in space. It is also defined for an infinitesimal spectral interval. The spectral radiance, I_λ, is often described for a wavelength interval, dλ, and therefore has units

$$[I_\lambda] = \frac{\text{photons}}{\text{s cm}^2 \text{ nm sr}}, \tag{2.1}$$

where area is expressed in cm^2 and wavelength in nm. There are numerous variations in how the units are expressed, such as using Joules instead of photons to describe the radiative energy. In IR applications the spectral interval is often expressed using wavenumbers, ν, with units of cm^{-1} and with energy in Joules instead of photons. Replacing Joules per second with Watts, the radiance units become

$$[I_\nu] = \frac{\text{W}}{\text{cm}^2 \text{ cm}^{-1} \text{ sr}}. \tag{2.2}$$

In the field of radiative transfer, the term "radiance" generally implies a spectral radiance and this convention is used throughout this work.

2.2.1   The Radiative Transfer Equation

Radiance, $I(\vec{r}, \hat{\Omega})$, is a five dimensional quantity; it depends on a position, $\vec{r}$, and a look direction, $\hat{\Omega}$. Three dimensions arise from the position and two dimensions are contained in the look direction, which can be specified by an azimuthal angle, ϕ, and a zenith angle, θ. A path coordinate, s, is used to express radiative transfer variables in terms of their distance along a ray defined by the look direction. The value of s is zero at the observer and increases in the look direction, opposite to the direction of light propagation. These coordinates are illustrated in Figure 2.3. The blue vector indicates the look direction, or line of sight, of an observer positioned at $s = 0$. In a simple radiative transfer model the origin of this coordinate system is the centre of the Earth, but more sophisticated models account for the ellipsoid shape of the Earth (see Section 2.6.3).

Consider a layer of infinitesimal thickness ds along the direction of radiation propagation, which contains particles capable of either absorbing radiation or scattering it away from the line of sight. After moving through this material, the radiance, $I(s)$, is changed by an amount, dI. The probability per unit length that a photon travelling through the layer will

10
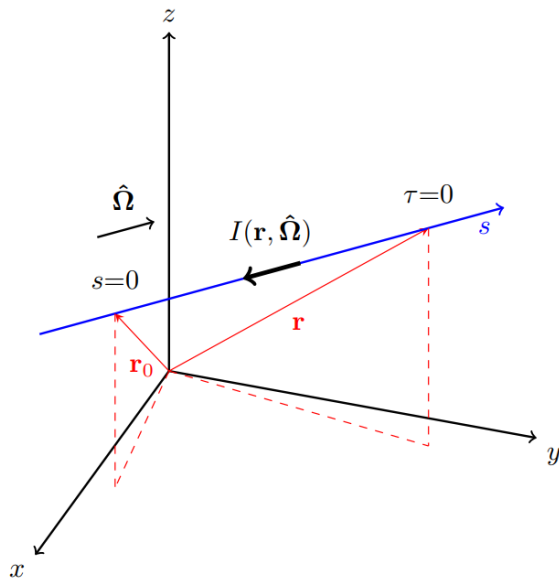
Figure 2.3: Geometry configuration for radiative transfer (Jensen, 2015).

interact with the medium and be scattered or absorbed is described by the extinction, $k(s)$. Extinction combines absorption, $k_a(s)$, and scattering, $k_s(s)$, probabilities and is given by their sum,

$$
\begin{aligned}
k(s) &= k_s(s) + k_a(s), \\
&= \sum_i \sigma_{si}(s) n_{si}(s) + \sum_j \sigma_{aj}(s) n_{aj}(s),
\end{aligned}
\tag{2.3}
$$

where the first summation is over the cross sections, $\sigma_{si}(s)$, and number densities, $n_{si}(s)$, of all scattering species present in the layer while the second summation is over all absorbing species present. Note that cross sections depend on the wavelength of radiation, and therefore the extinction and radiance have a wavelength dependence. For simplicity of notation, the wavelength dependence is not shown. The details of the absorption cross section calculation are described in Section 2.3. Once extinction is calculated, the change in radiance across the layer is

$$
dI = -I(s)k(s)ds.
\tag{2.4}
$$

The radiance removed from the line of sight is equal to the initial radiance multiplied by the probability of extinction per unit length, multiplied by the thickness of the layer. Consider

a layer with finite thickness, Δs, and constant extinction, k. If the incoming radiance is I_0, Equation (2.4) can be solved for the outgoing radiance, I_f,

$$I_f = I_0 e^{-k\Delta s}. \tag{2.5}$$

The term $k\Delta s$ is called the optical depth of the layer and is represented by τ. For a nonuniform extinction, the optical depth between two points is given by

$$\tau(s_1, s_2) = \int_{s=s_1}^{s=s_2} k(s)\mathrm{d}s. \tag{2.6}$$

Therefore, in the absence of any radiation sources between s_1 and s_2 the attenuated radiance is

$$I(s_2) = I(s_1)e^{-\tau(s_1,s_2)}. \tag{2.7}$$

It is also possible for the radiance to be increased by the layer if there exists a source of radiation in the medium. The source function, $J(s)$, is added to Equation (2.4) to obtain the general differential form of the radiative transfer equation,

$$\mathrm{d}I = -I(s)k(s)\mathrm{d}s + J(s)\mathrm{d}s. \tag{2.8}$$

Through an application of integrating factors, the radiative transfer equation is solved for the radiance, $I(\vec{r_0}, \hat{\Omega})$, at the observer,

$$I(\vec{r_0}, \hat{\Omega}) = I(s_{\mathrm{end}})e^{-\tau(s_{\mathrm{end}},0)} + \int_{s_{\mathrm{end}}}^{0} J(s)e^{-\tau(s,0)}\mathrm{d}s, \tag{2.9}$$

where s_{end} is the distance from the observer to the end of the line of sight and is negative by convention. Depending on the look direction, the end point is either where the line of sight intersects the ground or where it leaves the atmosphere and enters space. Each optical depth in Equation (2.9) is the total optical depth from the observer to a point along the line of sight. Therefore, observed radiance is the sum of the radiance from the end of the line of sight attenuated back to the observer and the attenuated radiation source from every point along the line of sight.

The source function, $J(s)$, can be the result of several different physical phenomena. Potential radiation sources include: sunlight scattered from particles into the line of sight, thermal emissions from gas species, and photochemical emissions. Depending on the spectral

region of interest, different sources will dominate the measured radiance. Photochemical emissions occur at specific wavelengths, such as the oxygen A-band from 759 to 771 nm, and are not considered because this work is focused on IR wavelengths. Scattered sunlight dominates the signal at visible and near IR wavelengths, while the contribution from thermal emissions becomes increasingly significant at longer IR wavelengths. This result is due to the difference in temperature between the Sun and Earth. With extreme temperatures near 5800 K, solar radiation peaks in the visible spectrum, while atmospheric temperatures between 200 and 300 K cause molecular emissions to peak in the IR near 10 μm.

The following sections describe the source functions for including scattered sunlight and thermal emissions in the radiative transfer equation.

2.2.2 Scattered Sunlight

As photons from the sun travel through the atmosphere, there is a chance that they will scatter from atmospheric particles. Scattering affects the trajectory of photons, and any photons that are scattered from particles along the line of sight can be redirected towards the observer. Photons that are scattered directly from the sun into the line of sight contribute to the solar scattering source term, $J_{ss}(s)$. Higher scattering orders, in which photons scatter more than once before being added to the line of sight, will be added later.

Let $F_{\text{sun}}(\hat{\Omega}')$ be the solar irradiance propagating in the direction $\hat{\Omega}'$. From Equation (2.7), the solar irradiance that arrives at point s along the line of sight is $F_{\text{sun}}e^{-\tau(\text{sun},s)}$. The primed coordinates are used here to indicate that initial propagation direction of sunlight differs from the line of sight vector. Multiplying this term by the scattering probability $k_s(s)$ gives the amount of solar photons that will be scattered at this location, in all directions. Finally, the expression is multiplied by a phase function, $p(\hat{\Omega}', \hat{\Omega})$. The phase function describes the probability that a photon travelling in the direction of $\hat{\Omega}'$ will be scattered in the direction of $\hat{\Omega}$. Combining these factors results in the following expression for the single scatter source term,

$$J_{ss}(s) = F_{\text{sun}}e^{-\tau(\text{sun},s)}k_s(s)p(\hat{\Omega}_{\text{sun}}, \hat{\Omega}), \tag{2.10}$$

where $\hat{\Omega}_{\text{sun}}$ is the vector pointing towards the sun and $\hat{\Omega}$ is the vector pointing along the

line of sight towards the observer. The phase function is a normalized distribution across all possible scattering angles and depends on a number of factors, such as photon wavelength and the size of scattering particles.

Multiple Scattering

It is important to consider higher orders of scattering when evaluating the scattered sunlight source term. For example, a photon could scatter from multiple particles in the atmosphere before being scattered into the line of sight. Therefore, at any point along the line of sight photons may be approaching from all directions and not only from the direction of the sun. To evaluate the multiple scattering source term at point s the incoming radiance must be known for all directions, $\hat{\Omega}'$, over the unit sphere. Similar to Equation (2.10), the incoming radiances are multiplied by the phase function and scattering probability to determine their contribution to the line of sight radiance. Integrating over the unit sphere gives the multiple scattering source function,

$$J_{ms}(s) = k_s(s) \int_{4\pi} I(s, \hat{\Omega}')p(\hat{\Omega}', \hat{\Omega})\mathrm{d}\hat{\Omega}'. \tag{2.11}$$

This equation contains $I(s, \hat{\Omega}')$ which is calculated using Equation (2.9) but instead of calculating for a single look direction, it must be determined for all incoming directions given by $\hat{\Omega}'$. The coupled nature of Equations (2.9) and (2.11) demonstrates the complexity of the multiple scattering calculation.

Ground Scattering

In addition to being scattered from airborne particles in the atmosphere, sunlight is also reflected from the surface of the Earth. If the line of sight ends at the ground, sunlight will be directly scattered from the surface into the line of sight. However, even if the line of sight ends outside the atmosphere there will still be a ground-reflection contribution due to multiple scattering effects. Photons can be initially reflected by the ground then scattered towards the observer from atmospheric particles.

The reflection of light from a surface is described by a bidirectional reflectance distribution function (BRDF), which is used to determine the direction and intensity of scattered

radiation. Depending on the shape and composition of the ground, the BRDF can take different forms. However, a simple and generally accurate approximation for the surface of the Earth is to assume a Lambertian BRDF. The Lambertian BRDF describes a surface which appears to be the same brightness, regardless of viewing direction. Define the spectral flux density, $F(s, \hat{n})$, as the projection of a radiance field, I, along a direction $\hat{n}$ normal to the surface and integrated over the hemisphere on the above-ground side of the surface. The spectral flux density is then

$$F(s, \hat{n}) = \int_{2\pi} I(s, \hat{\Omega}') \cos(\theta') \mathrm{d}\Omega', \tag{2.12}$$

where θ' is the angle between incoming radiance and the surface normal. For a radiance I with units of [photon/(s cm^2 nm sr)], F has units of [photon/(s cm^2 nm)] as it is the result of integrating I over a 2π steradian solid angle above the ground.

To determine an expression for the radiance, I_{out}, reflected by a Lambertian surface, begin by finding an expression for F_{up}, the upward flux density given by inserting I_{out} into equation (2.12). For a Lambertian surface I_{out} does not depend on the incoming direction $\hat{\Omega}'$ and can therefore be moved outside the integral, resulting in

$$\begin{aligned} F_{\mathrm{up}}(s, \hat{n}) &= I_{\mathrm{out}}(s) \int_{2\pi} \cos(\theta') \mathrm{d}\Omega', \\ &= \pi I_{\mathrm{out}}(s). \end{aligned} \tag{2.13}$$

Next, let a be the fraction of photons reflected by the ground to the total number of incident photons, known as the albedo. In other words, albedo is the ratio of the reflected upward flux, F_{up}, to the incident downward flux, F_{down},

$$a = \frac{F_{\mathrm{up}}}{F_{\mathrm{down}}}. \tag{2.14}$$

Combining Equations (2.13) and (2.14) allows the radiance reflected from a Lambertian surface to be written as

$$I_{\mathrm{out}}(s) = \frac{a}{\pi} F_{\mathrm{down}}(s, \hat{n}). \tag{2.15}$$

In general, albedo is a function of wavelength, but it is common to assume a scalar value across across the visible and near IR. The scalar value depends on the surface composition. For example, snow-covered ground has a much higher albedo. Typical values of albedo for some different surface types are shown in Table 2.1 (McEvoy et al., 2003).

Surface type	Albedo
Dry grass	0.28-0.32
Bare soil	0.17
Asphalt	0.15
Fresh snow	0.80-0.90
Old snow	0.45-0.70

Table 2.1: Typical albedo values for various ground types (McEvoy et al., 2003).

There are two main cases to consider when calculating F_{down}. The first case is when light directly from the sun is reflected from the ground. In this case the incoming light will be the solar irradiance attenuated to the ground, which is $F_{\text{sun}}e^{-\tau(\text{sun},s)}$ as discussed in Section 2.2.2. Since the sunlight comes from a single direction, the integral in (2.12) collapses to single value, resulting in

$$F_{\text{down}} = F_{\text{sun}}e^{-\tau(\text{sun},s)}\cos(\theta_{\text{sza}}), \tag{2.16}$$

where θ_{sza} is the angle between the surface normal and the direction of incoming sunlight, called the solar zenith angle (SZA). In atmospheric geometry, the vector normal to the surface of the earth is generally referred to as the vertical or zenith direction.

The second case to consider when calculating F_{down} occurs for light that is reflected from the ground after being scattered one or more times in the atmosphere. In this situation radiation will be incoming from all directions in the hemisphere above the surface. The downward flux is determined by Equation (2.12) where $I(s, \hat{\Omega}')$ is the multiple-scattered light from every direction.

Scattering Orders

One method for modeling the radiance contribution from multiply scattered sunlight is the successive orders technique implemented in SASKTRAN (Bourassa et al., 2008). In the successive orders method the observed radiance described by Equation (2.9) is rewritten as

$$I(0) = \int_{s_{\text{end}}}^{0} \left[\sum_{i=1}^{\infty} J_i(s,\hat{\Omega})\right] e^{\tau(s,0)}\mathrm{d}s + \left[\sum_{i=1}^{\infty} \tilde{I}_i(s_{\text{end}})\right] e^{-\tau(s_{\text{end}},0)}, \tag{2.17}$$

where the index i indicates the scattering order. For example, J_1 is the source term contribution from light that has been scattered once and J_2 is from light that has been scattered twice. Similarly, $\tilde{I}_i$ is the contribution from the end of the line of sight, which is nonzero only when the line of sight intersects the ground. Light that reaches the ground without scattering from the atmosphere and is then redirected towards the observer is denoted $\tilde{I}_1$ while higher indexes describe photons that encountered one or more scattering events before reaching the ground.

The successive orders technique is an iterative method for calculating the observed radiance. First determine the first order contribution from ground-scattered photons:

$$\tilde{I}_1(s_{\text{end}}) = \frac{a}{\pi} F_{\text{sun}}(\hat{\Omega}_{\text{sun}}) e^{-\tau(\text{sun}, s_{\text{end}})} \cos(\theta_{sza}). \tag{2.18}$$

The single scattered light source term at each point along the line of sight is

$$J_1(s, \hat{\Omega}) = k_s(s) F_{\text{sun}}(\hat{\Omega}_{\text{sun}}) e^{-\tau(\text{sun}, s)} p(\hat{\Omega}_{\text{sun}}, \hat{\Omega}), \tag{2.19}$$

resulting in an overall first-order solution of

$$I_1(0) = \int_{s_{\text{end}}}^{0} J_1(s, \hat{\Omega}) e^{-\tau(s, 0)} ds + \tilde{I}_1(s_{\text{end}}) e^{-\tau(s_{\text{end}}, 0)}. \tag{2.20}$$

Next, higher order source terms are calculated by scattering the radiance from the previous order, resulting in

$$J_i(s, \hat{\Omega}) = k_s(s) \int_{4\pi} I_{i-1}(s, \hat{\Omega}') p(\hat{\Omega}', \hat{\Omega}) d\hat{\Omega}'. \tag{2.21}$$

This calculation must be performed at every point in the atmosphere, as $I_{i-1}(s, \Omega')$ must be known for every possible direction. Multiply scattered light may also be reflected by the ground into the line of sight, as given by

$$\tilde{I}_i(s_{\text{end}}) = \frac{a}{\pi} \int_{2\pi} I_{i-1}(s_{\text{end}}, \hat{\Omega}') \cos(\theta') d\hat{\Omega}', \tag{2.22}$$

resulting in an ith order radiance contribution of

$$I_i(0) = \int_{s_{\text{end}}}^{0} J_i(s, \hat{\Omega}) e^{-\tau(s, 0)} ds + \tilde{I}_i(s_{\text{end}}) e^{-\tau(s_{\text{end}}, 0)}. \tag{2.23}$$

Therefore, the total radiance seen by the observer is

$$I(0) = \sum_{i=1}^{\infty} I_i(0). \tag{2.24}$$

17

Rayleigh Scattering

Rayleigh scattering is an approximation that can be applied when photons scatter from particles which are orders of magnitude smaller than the wavelength of incident light. Earth's atmosphere is composed primarily of nitrogen and oxygen molecules, making Rayleigh scattering the dominant form of scattering for visible and near IR light. The phase function is

$$p(\Theta) = \frac{3}{4}(1 + \cos^2(\Theta)), \tag{2.25}$$

where Θ is the scattering angle, the angle between the photons velocity vector before and after being scattered. The Rayleigh scattering cross section is

$$\sigma_s = \frac{128\pi^5}{3}\frac{\alpha^2}{\lambda^4}, \tag{2.26}$$

where α is the polarizability of the scattering particle. Bates (1984) describes a commonly used method for calculating the scattering cross section of dry air by computing a weighted average over the relevant atmospheric species, where each specie's cross section is weighted by its relative abundance. An important feature of Equation (2.26) is the $1/\lambda^4$ dependence, which indicates that smaller wavelengths will be scattered more effectively and provides an explanation for the blue appearance of the sky.

Mie Scattering

Larger particles, such as atmospheric aerosols, cannot be described with the Rayleigh scattering approximation. The particles are large enough that it can no longer be assumed that the electric field from the incident radiation is constant at every point inside the particle. Instead, the particles are treated as spheres and the incident radiation is treated as a plane wave. Mie (1908) developed a solution for the scattered wave. The inclusion of aerosol scattering is important for radiative transfer calculations in the visible and near-infrared spectral regions. For example, profiles of stratospheric aerosol concentration have been retrieved from OSIRIS measurements at visible and near IR wavelengths (Bourassa et al., 2007). However, the contribution to the overall radiance from aerosol scattering becomes negligible at larger wavelengths. Unless clouds are included in the simulation, scattering can be safely ignored (Griessbach et al., 2013). Cloud scattering is beyond the scope of this thesis.

2.2.3 Thermal Radiation

At longer wavelengths it becomes necessary to consider the thermal emission of photons from molecules of atmospheric species as a significant component of the radiative transfer source function. Therefore, let $J_{\text{thermal}}(s)$ be the thermal emission source term which describes how much radiation of a wavelength λ is added to the line of sight at position s. The contribution is from photons that are emitted by molecules when they transition from a higher energy state to a lower energy state. Such energy transitions may occur spontaneously or be induced via interactions with other particles. Due to the quantized nature of molecular energy levels, specific energy transitions are permitted which depend on the structure of the molecule. The allowed energies determine the wavelengths of the photons that may be emitted, making the thermal radiation source term highly dependent on the species present in the atmosphere. Section 2.3 describes these microphysics in greater detail.

The description of thermal radiation begins with a discussion of two major assumptions which greatly simplify the resulting source function. First, the assumption of Local Thermodynamic Equilibrium (LTE) states that the atmosphere may be partitioned into sections that are small enough that thermodynamic equilibrium can safely be assumed within each section. Therefore, the atmosphere within each small section can be interpreted as a black body in which the emitted radiation is proportional to Planck's radiation function. In a typical black body model, the constant of proportionality is called the emissivity and varies with wavelength according the allowed energy transitions of the emitting matter. The second assumption uses the principle of detailed balance to show that to maintain balance the amount of photons emitted must be equal to the amount absorbed in a given time. Therefore, the collective emissivity of all of the particles in this section must be equal to their absorptivity at all wavelengths. The resulting thermal radiation source is the black body radiation, $B(T)$, multiplied by the absorption, k_a,

$$J_{\text{thermal}}(s) = k_a(s)B(T(s)), \tag{2.27}$$

where the temperature, T, is also dependent on the current position, s. Appendix B provides a derivation of the Planck function for the radiation emitted by a black body with temperature T.

Surface Emission

When the observer's line of sight intersects the ground, there will be a radiance contribution due to the thermal radiation emitted by the ground. Since the surface of the Earth is a solid, it can modelled as a black body with a continuous spectra given by the Planck function, under the assumption of LTE. Therefore the thermal contribution to the radiance from the end of the line of sight, $I(s_{\text{end}})$ in Equation (2.9), is given by

$$I_{\text{thermal}}(s_{\text{end}}) = \varepsilon_{\text{surf}} B(T_{\text{surf}}(s_{\text{end}})), \tag{2.28}$$

where T_{surf} is the surface temperature and $\varepsilon_{\text{surf}}$ is the surface emissivity. The emissivity is a parameter between 0 and 1 which may vary with wavelength, although it is often assumed to be a constant value across a narrow spectral window with a value determined by the surface composition. For example, surfaces covered by vegetation, water, and ice have emissivities greater than 0.95 while desert areas can have emissivities below 0.85 (Hulley et al., 2015).

Combining Thermal and Solar Sources

Now that the primary radiation sources have been described, they can be combined in the radiative transfer calculation. At near infrared wavelengths in the 2 to 5 μm range, both sources must be considered for an accurate model. Combining the terms is achieved by adding the thermal source (Equation (2.27)) and the source term from single-scattered sunlight (Equation (2.10)), resulting in

$$
\begin{aligned}
J(s) &= J_{\text{solar}}(s) + J_{\text{thermal}}(s), \\
&= F_{\text{sun}} e^{-\tau(\text{sun},s)} k_s(s) p(\hat{\Omega}_{\text{sun}}, \hat{\Omega}) + k_a(s) B(T(s)).
\end{aligned}
\tag{2.29}
$$

If multiple orders of scattering are to be calculated, this expression becomes the first order source term in the successive orders calculation. In doing so, the thermal radiation is scattered along with the sunlight. If the line of sight ends at the ground, the surface emissions from Equation (2.28) are simply added to the first order ground scattered sunlight in (2.18).

2.3　Absorption and Emission Spectroscopy

This section describes the interaction of electromagnetic radiation with molecular particles. The processes by which photons are absorbed or emitted by molecules, including the allowed energy levels of these photons, are detailed. These concepts are applicable to all spectral regimes but an emphasis is placed on their application to infrared radiative transfer. Spectral lines and their importance in determining absorption cross sections are reviewed.

2.3.1　Radiative Processes

There are three main processes by which the energy state of a molecule can be changed due to interaction with electromagnetic radiation. The first occurs when an incident photon interacts with a molecule and is absorbed, resulting in a increase in energy from a lower energy state, l, to a higher energy state, u. This process is called induced absorption and the molecule gains energy equal to the energy of the incident photon. The second possibility is that interaction with a photon causes the molecule to emit a photon, dropping from a higher energy level to a lower energy level, and is called induced emission. The third process is called spontaneous emission and occurs when the molecule transitions from a higher energy state to a lower energy state, through no external interaction, and emits a photon with energy equal to the difference between upper and lower energy levels. In all processes the energies of the emitted and absorbed photons are limited due to the quantization of energy levels. The light associated with a transition between two particular energy states has a specific energy, or wavelength, and is called a spectral line.

Consider a collection of molecules immersed in a radiation field in which the assumption of local thermodynamic equilibrium (LTE) holds true. In LTE the kinetic energy of the gas is in equilibrium with the radiation field. Therefore, the energy radiated by this gas is described by a black body with the same temperature, T, which describes the combined kinetic motion of the molecules in the region. We will investigate molecules in this gas transitioning between lower quantum state l and upper quantum state u. Let n_l be the number of molecules per unit volume in state l, Similarly, let n_u be the population of state u per unit volume in state u.

It is shown in Appendix B that the radiation field in the frequency interval $[f, f + \mathrm{d}f]$, assuming LTE, has a spectral energy density, $u(f)$, given by Equation (B.17) and restated here:

$$u(f) = \frac{8\pi h f^3}{c^3} \frac{1}{e^{hf/kT} - 1} \left[\frac{\mathrm{J}}{\mathrm{m}^3 \cdot \mathrm{Hz}} \right]. \tag{2.30}$$

Here, f, is the frequency of a photon with energy equal to difference between the upper state energy, E_u, and the lower state energy, E_l, or

$$f = \frac{E_u - E_l}{h}, \tag{2.31}$$

$u(f)$ describes the energy of the radiation interacting with molecules in the gas through the processes of induced absorption and induced emission.

2.3.2   Einstein Coefficients

The probability that a transition will occur between the two states is described by one of the three Einstein coefficients. The coefficient $A_{u \to l}$ describes the probability of spontaneous emission per unit time, $B_{u \to l}$ is the coefficient of induced emission, and $B_{l \to u}$ is the coefficient of induced absorption. $B_{l \to u}$ is defined such that the product $u(f)B_{l \to u}$ is the probability per unit time of a transition from state l to u from induced absorption for single molecule. This product has units of $[\mathrm{s}^{-1}]$ and therefore $B_{l \to u}$ must have units of $[(\mathrm{m}^3 \cdot \mathrm{Hz})/(\mathrm{J} \cdot \mathrm{s})]$. Similarly, the probability of a transition from u to l as a result of induced emission is given by $u(f)B_{u \to l}$. Lastly, $A_{u \to l}$ is the probability of a spontaneous emission producing a transition from u to l. There is no multiplication by $u(f)$ because there is no interaction with the radiation field during this process and therefore $A_{u \to l}$ has units of $[\mathrm{s}^{-1}]$. The coefficient subscripts indicate the energy state transition, with $l \to u$ indicating a transition from a lower state to a higher one and vice-versa for $u \to l$.

Multiplying these transition probabilities by the number of molecules in each state gives the number of transitions between u and l. Specifically, the number of molecules that transition from state l to u per unit time and volume is

$$\text{absorption rate} = n_l u(f) B_{l \to u}, \tag{2.32}$$

and the transitions from u to l are given by the sum of spontaneous and induced emission,

$$\text{emission rate} = n_u[A_{u \to l} + u(f)B_{u \to l}]. \tag{2.33}$$

In equilibrium, the rate of emission must be equal to the rate of absorption. Therefore, Equations (2.32) and (2.33) can be equated and rearranged to get

$$\frac{n_l}{n_u} = \frac{A_{u \to l} + u(f)B_{u \to l}}{u(f)B_{l \to u}}. \tag{2.34}$$

Boltzmann statistics states that the expected number of particles per unit volume with energy E_l, in thermal equilibrium, is equal to

$$n_l = \frac{g_l e^{-E_l/kT}}{Z}n, \tag{2.35}$$

where Z is the partition function and n is total number of molecules per unit volume. g_l is the degeneracy of state l, or the number of unique quantum states that have energy E_l. Similarly, n_u can be defined using Boltzmann statistics, resulting in a second expression of the ratio n_l/n_u,

$$\frac{n_l}{n_u} = \frac{g_l}{g_u}e^{-(E_l-E_u)/kT}, \tag{2.36}$$

which may also be written as

$$\frac{n_l}{n_u} = \frac{g_l}{g_u}e^{hf/kT}, \tag{2.37}$$

by substituting in the photon energy from Equation (2.31). Equating (2.34) and (2.37) and solving for $u(f)$ gives

$$u(f) = \frac{A_{u \to l}/B_{u \to l}}{\frac{B_{l \to u}}{B_{u \to l}}\frac{g_l}{g_u}e^{hf/kT} - 1}. \tag{2.38}$$

By comparing this result with Equation (2.30) the following expressions relating the Einstein coefficients are obtained:

$$A_{u \to l} = B_{u \to l}\frac{8\pi h f^3}{c^3},$$
$$B_{l \to u} = B_{u \to l}\frac{g_u}{g_l}. \tag{2.39}$$

Solving to eliminate $B_{u \to l}$ results in

$$A_{u \to l} = B_{l \to u}\frac{g_l}{g_u}\frac{8\pi h f^3}{c^3}. \tag{2.40}$$

2.3.3 Spectral Line Strength

Now that the relationships between the Einstein coefficients have been developed, the spectral line strength can be determined. It is shown in Equation (B.19) that the radiant energy directed through a surface per unit time per steradian for frequencies between f and $f + \mathrm{d}f$ is equal to $u(f)c/(4\pi)$. Let $k_L(f)$ be the absorption coefficient describing the probability per unit length for photons with frequency f to be absorbed. The energy absorbed per unit volume per unit time is then obtained by integrating $k_L(f)u(f)c/(4\pi)$ over all solid angles and the frequency interval Δf where $k_L(f)$ is nonzero,

$$\int_{\Delta f} \int_{\Omega} k_L(f)u(f)\frac{c}{4\pi}\,\mathrm{d}f\mathrm{d}\Omega = c\int_{\Delta f} k_L(f)u(f)\,\mathrm{d}f. \tag{2.41}$$

This expression can be divided by the energy of a photon, hf, to obtain the number of photons absorbed per unit volume per unit time,

$$n_{tr} = c\int_{\Delta f} \frac{k_L(f)u(f)}{hf}\mathrm{d}f. \tag{2.42}$$

By assuming that the frequency interval, Δf, is small enough that $u(f)$ can safely be taken as a constant value, absorbed photons can be approximated by

$$n_{tr} \approx \frac{cu(f)}{hf}\int_{\Delta f} k_L(f)\mathrm{d}f. \tag{2.43}$$

n_{tr} may also be thought of as the net number of induced transitions from from state l to u. Therefore, it can be expressed in terms of the Einstein B coefficients,

$$n_{tr} = (n_l B_{l\rightarrow u} - n_u B_{u\rightarrow l})u(f). \tag{2.44}$$

The integrated line strength of the l to u transition, S'_{lu}, is defined as the absorption coefficient integrated over the frequency interval. It is obtained by combining Equations (2.43) and (2.44) and rearranging the result to find

$$S'_{lu} \equiv \int_{\Delta f} k_L(f)\mathrm{d}f = (n_l B_{l\rightarrow u} - n_u B_{u\rightarrow l})\frac{hf}{c}, \tag{2.45}$$

which can be rearranged into the following form,

$$S'_{lu} = n_l B_{l\rightarrow u}\left(1 - \frac{n_u}{n_l}\frac{B_{u\rightarrow l}}{B_{l\rightarrow u}}\right)\frac{hf}{c}. \tag{2.46}$$

From equations (2.37) and (2.39) it can be seen that

$$\frac{n_u}{n_l}\frac{B_{u\to l}}{B_{l\to u}} = e^{-hf/kT}, \tag{2.47}$$

and therefore

$$S'_{lu} = n_l B_{l\to u}\left(1 - e^{-hf/kT}\right)\frac{hf}{c}. \tag{2.48}$$

In the thermal infrared regime, spectral line strengths are often expressed in terms of the wavenumber, ν. Substituting frequency with wavenumber, by $f = c\nu$, results in

$$S'_{lu} = n_l B_{l\to u}\left(1 - e^{-hc\nu/kT}\right)h\nu \ \left[\mathrm{m}^{-1}\,\mathrm{s}^{-1}\right]. \tag{2.49}$$

The final form of spectral line intensity, S_{lu}, is obtained by dividing by c and the the number of molecules per unit volume, n,

$$S_{lu} = \frac{n_l}{n}B_{l\to u}\left(1 - e^{-hc\nu/kT}\right)\frac{h\nu}{c} \ \left[\mathrm{m}^2\,\mathrm{m}^{-1}\right]. \tag{2.50}$$

The units are written as $[\mathrm{m}^2\,\mathrm{m}^{-1}]$ to explicitly indicate the spectral unit is wavenumbers in m^{-1}.

Calculating Spectral Line Intensity

The HIgh-resolution TRANsmission molecular absorption (HITRAN) database provides the parameters needed to compute the spectral line intensity (Gordon et al., 2017). It is the culmination of spectroscopic research over many years and contains information for many species, including those with significant impact in the thermal infrared such as water vapour, carbon dioxide, ozone, and methane. The database is available directly from the HITRAN website at `https://hitran.org` or through a python API. This API has been implemented into SASKTRAN, allowing the model to be easily incorporate updates to the HITRAN database.

The HITRAN database provides data files where each entry contains information about a specific transition for a given isotopologue of a molecular species. Some of the most important parameters in each entry are the transition wavenumber, ν_{lu}, the Einstein coefficient of spontaneous emission, $A_{u\to l}$, the lower state energy, E_l, and the upper state degeneracy, g_u.

Equation (2.50) may be rewritten in terms of these parameters by changing $B_{l \to u}$ to $A_{u \to l}$ from Equation (2.40) and substituting for n_l from Equation (2.35). The result is

$$S_{lu} = \frac{A_{lu}}{8\pi c \nu_{lu}^2} \frac{g_u e^{-E_l/kT}(1 - e^{-hc\nu_{lu}/kT})}{Z(T)}. \tag{2.51}$$

Another parameter supplied by HITRAN for each transition line is the spectral line intensity at a reference temperature, T_{ref}, of 296 K. This parameter provides a method for calculating S_{lu} at an arbitrary temperature, T. Taking the ratio of the spectral line intensity at the desired temperature, $S_{lu}(T)$ to the reference value, $S_{lu}(T_{\text{ref}})$ and solving for $S_{lu}(T)$ gives

$$S_{lu}(T) = S_{lu}(T_{\text{ref}}) \frac{Z(T_{\text{ref}})}{Z(T)} \frac{\exp\left(\frac{-E_l}{kT}\right)}{\exp\left(\frac{-E_l}{kT_{\text{ref}}}\right)} \frac{1 - \exp\left(-\frac{hc\nu_{lu}}{kT}\right)}{1 - \exp\left(-\frac{hc\nu_{lu}}{kT_{\text{ref}}}\right)} \quad [\text{cm}^2 \text{ cm}^{-1}]. \tag{2.52}$$

Note that the spectral line intensities supplied by HITRAN have units of $[\text{cm}^2 \text{ cm}^{-1}]$ and have been scaled by the relative abundance of the isotopologue. Most species in the HITRAN database contain multiple isotopologues, which are the different isotope combinations that may form a molecule of the species in question. For example, there are two isotopologues of SO_2 in the database. One contains a sulphur isotope with 32 neutrons, giving it the chemical formula $^{32}S^{16}O_2$ while the other contains sulphur with 34 neutrons, written as $^{34}S^{16}O_2$. For a typical atmosphere the most common isotopologue, $^{32}S^{16}O_2$ has a relative abundance of 0.945678, indicating that 94.5678% of the sulphur dioxide molecules in the atmosphere will be of this form (imekov et al., 2006).

The total internal partition sums, $Z(T)$, are stored as a table of values for each species over a range of temperatures. The current version of HITRAN provides a FORTRAN program for interpolating from these tables at a specified temperature (Gordon et al., 2017).

2.3.4 Spectral Line Shape

The quantization of molecular energy levels results in transitions occurring at discrete wavelengths. In reality, the spectral lines undergo broadening due to a number of physical factors. Therefore, the radiant emission or absorption from a single spectral line will be observed at wavenumbers near ν_{lu}. The two most important effects to consider are Doppler broadening and Lorentz broadening. These effects are described by normalized lineshape functions,

$\phi(\nu_{lu} - \nu)$, which describe the contribution of a spectral line at ν_{lu} to the cross section calculated at ν. In the following sections $\nu_{lu} - \nu$ is often written as $\Delta\nu$. The lineshape function is normalized such that

$$\int_{-\infty}^{\infty} \phi(\nu_{lu} - \nu)\mathrm{d}\nu = 1. \tag{2.53}$$

Therefore, $\phi(\Delta\nu)$ has units of [cm] and multiplying it by the line strength from Equation (2.52) gives the absorption cross section $\sigma_a(\nu)$ contribution from the spectral line. Natural, Lorentz, and Doppler broadening mechanisms are discussed in the following sections. Although natural broadening has a negligible effect, it is introduced because similar concepts are applied to Lorentz broadening.

Natural Broadening

Natural broadening accounts for the energy uncertainty that occurs as a result of the time a molecule spends in an excited energy state before spontaneous emission of a photon causes a transition to a lower energy state. By the time-energy uncertainty principle, the uncertainties of the time spent in the excited state, Δt, and the energy of this state, ΔE, are related by

$$\Delta E \Delta t \geq \frac{h}{2\pi}. \tag{2.54}$$

The energy uncertainty can be related to the wavenumber uncertainty, $\Delta\nu$, from the photon energy equation,

$$\Delta E = hc\Delta\nu. \tag{2.55}$$

Substituting ΔE into Equation (2.54) shows that the wavenumber uncertainty is

$$\Delta\nu \approx \frac{1}{2\pi c \Delta t}. \tag{2.56}$$

By definition, the Einstein coefficient for spontaneous emission, $A_{u \to l}$, states that the number of molecules in the upper state, N_u, evolves over time by

$$\frac{\mathrm{d}N_u}{\mathrm{d}t} = -A_{u \to l} N_u. \tag{2.57}$$

This differential equation has the solution,

$$N_u(t) = N_u(0)e^{-A_{u \to l}t} = N_u(0)e^{-t/\tau}, \tag{2.58}$$

where the time constant, $\tau = A_{u \to l}^{-1}$, is the lifetime of the state. In the thermal infrared regime, values of $A_{u \to l}^{-1}$ given by HITRAN are on the order of $10 \, \text{s}^{-1}$ at most. Therefore, the smallest lifetimes observed are on the order of $0.1 \, \text{s}$. Inserting a time uncertainty of $0.1 \, \text{s}$ into Equation (2.56) results in a maximum wavenumber uncertainty on the order of $10^{-11} \, \text{cm}^{-1}$. Compared to other broadening effects, this amount is negligible.

Pressure Broadening

While natural broadening can be ignored for atmospheric conditions in the infrared, the concept of time-energy uncertainty is relevant to pressure broadening. Also known as collisional broadening, pressure broadening accounts for the energy uncertainty related to the lifetime of energy states as a result of collisions between molecules. When molecules collide they interact with each other, creating a combined system with different energy levels where absorption or emission of photons at the energy levels of the isolated molecules is no longer possible. Therefore, any absorption and emission processes must take place in the time between collisions. It is assumed that the collision process is significantly smaller than the time between collisions. When the rate of collisions is increased, the uncertainty in the lifetime of an energy state must decrease so that a transition may occur between collisions. As a result, there is a larger uncertainty in the energy level, or wavenumber associated with the transition.

Both natural and pressure broadening are types of Lorentz broadening, a line shape which accounts for uncertainty in the lifetime, τ, of a state. For natural broadening τ refers to the lifetime of a state before spontaneous emission occurs, while in the pressure broadening process τ is the time between collisions with other molecules. The probability that an electron will transition from its excited state in time t is t/τ. Therefore, the probability for no transitions to occur in time t is given by the Poisson distribution,

$$P(t) = \lim_{N \to \infty} \left(1 - \frac{t}{N\tau} \right)^N = e^{-t/\tau}. \tag{2.59}$$

The time dependence of the electromagnetic wave resulting from a transition at frequency f_0 will then be proportional to

$$E(t) \propto P(t) e^{j 2\pi f_o t}, \tag{2.60}$$

and taking its Fourier transform results in a frequency dependence of

$$E(f) \propto \int_0^\infty e^{-t/\tau} e^{j2\pi f_0 t} e^{-j2\pi ft} = \frac{1}{1/\tau + 2\pi j(f - f_0)}. \tag{2.61}$$

The resulting intensity of this wave is

$$I(f) \propto E(f)E^*(f) \propto \frac{\tau^2}{1 + 4\tau^2\pi^2(f - f_0)^2}. \tag{2.62}$$

The intensity shows the frequency distribution of the electromagnetic wave resulting from this energy transition. The Lorentz line shape describing this process can be obtained by normalizing Equation (2.62) for all frequencies between 0 and infinity. The result that is obtained is

$$\phi_L(f - f_0) = \frac{1}{\pi + 2\tan^{-1}(2\pi f_0 \tau)} \times \frac{1/\pi\tau}{1/4\pi^2\tau^2 + (f - f_0)^2}. \tag{2.63}$$

The expression for ϕ_L can be simplified by assuming that the central frequency, f_0, is orders of magnitude greater than τ^{-1}, which will be in the thermal infrared where $f_0 \sim 10^{13}$ Hz. Therefore,

$$\tan^{-1}(2\pi f_o \tau) \approx \frac{\pi}{2}, \;\; f_0 \gg \frac{1}{\tau}, \tag{2.64}$$

and Equation (2.63) simplifies to

$$\phi_L(f - f_0) = \frac{1/2\pi^2\tau}{1/4\pi^2\tau^2 + (f - f_0)^2}. \tag{2.65}$$

Converting from frequency to wavenumber (by $\phi_L(f - f_0)\mathrm{d}f = \phi_L(\nu - \nu_0)\mathrm{d}\nu$) the final form of the Lorentz line shape is

$$\phi_L(\Delta\nu) = \frac{1}{\pi} \frac{2\gamma_L}{4\gamma_L^2 + (f - f_0)^2}, \tag{2.66}$$

where

$$\gamma_L = \frac{1}{4\pi c\tau}, \tag{2.67}$$

is half width at half maximum (HWHM) of the distribution. When τ is the lifetime of an excited state, Equation (2.66) describes natural broadening. If τ is replaced with the mean time between collisions, pressure broadening is described.

Pressure broadening dominates at lower altitudes where the higher pressures result in a greater number of collisions. Additionally, the average speed of the molecules increases at

higher temperatures, resulting in a greater collision rate. Boltzmann statistics shows that the mean speed of particles with mass m in thermal equilibrium with temperature T is given by

$$\bar{v} = \sqrt{\frac{8kT}{\pi m}}. \tag{2.68}$$

Consider the movement of a single molecule within a gas and model the particles as spheres of radius r that collide elastically with each other. If the molecule moves with a speed given by Equation (2.68), the average time between collisions is

$$\tau = \left(An\bar{v}\right)^{-1}, \tag{2.69}$$

where n is the number of molecules per unit volume and A is the cross-sectional area in which a molecule will collide with another. A molecule will collide with another molecule if their centres are within $2r$ of each other. Therefore, the cross-sectional area is a circle with radius $2r$ and

$$\tau = \left(4\pi r^2 n\bar{v}\right)^{-1}. \tag{2.70}$$

The pressure broadened lineshape can be determined by inserting this expression for τ into Equation (2.67) and evaluating Equation (2.66). However, the HITRAN database provides Lorentzian HWHMs for each spectral line so that the masses and sizes of molecular species is not required in the radiative transfer model. The γ_L parameter depends on both temperature and pressure and is specified by HITRAN at standard temperature and pressure. In the HITRAN database, the pressure-broadened HWHM is split into γ_{self} resulting from collisions with molecules of the same species and γ_{air} resulting from collisions with neutral air particles. The HWHM can computed from these parameters by (Rothman et al., 1998),

$$\gamma_L(p, T) = \left(\frac{T_{\text{ref}}}{T}\right)^{n_{\text{air}}} \left(\gamma_{\text{air}}(p_{\text{ref}}, T_{\text{ref}})(p - p_{\text{self}}) + \gamma_{\text{self}}(p_{\text{ref}}, T_{\text{ref}})p_{\text{self}}\right), \tag{2.71}$$

where p_{self} is the partial pressure of the molecular species and n_{air} is a scaling parameter for the temperature dependence of the HWHM which is provided by HITRAN.

Doppler Broadening

Doppler broadening occurs due to the change in frequency of the radiation emitted by a moving molecule. The degree of Doppler broadening is characterized by using Boltzmann statistics to describe the mean velocity of gas particles. In an ideal gas containing N molecules,

Boltzmann statistics states that the fraction of molecules with mass m with speeds between v ad $v + dv$ is

$$\frac{dN(v)}{N} = \sqrt{\frac{m}{2\pi kT}} \exp\left(\frac{-mv^2}{2kT}\right) dv, \tag{2.72}$$

for motion in one dimension. At non-relativistic speeds, where $v \ll c$, the Doppler frequency shift is given by

$$f = f_0\left(1 - \frac{v}{c}\right), \tag{2.73}$$

where f_0 is the frequency of radiation in the reference frame of the moving molecule and f is the frequency seen an observer moving at speed v relative to the molecule. From Equation (2.73) it can be seen that

$$v = \frac{c(f - f_0)}{f_0}, \tag{2.74}$$

and

$$dv = \frac{c}{f_0}df. \tag{2.75}$$

Substituting these expressions into Equation (2.72) produces

$$\frac{dN(f)}{N} = \frac{1}{\sqrt{2\pi}\sigma} \exp\left(-\frac{(f - f_0)^2}{2\sigma^2}\right) df, \tag{2.76}$$

where

$$\sigma = \sqrt{\frac{f_0^2 kT}{mc^2}}. \tag{2.77}$$

This derivation shows that the doppler shifted frequencies have the form of a Gaussian distribution with mean frequency f_0 and standard deviation σ.

In spectroscopy, line shapes are expressed in terms of the half width at half maximum (HWHM), γ_D. A Gaussian distribution is symmetric about the mean, and the exponential term in Equation (2.76) has a maximum of 1, when $f = f_0$. Therefore, the HWHM is the difference, $f - f_0$, which causes the exponential term to be equal to $\frac{1}{2}$, or

$$\exp\left(-\frac{\gamma_D^2}{2\sigma^2}\right) = \frac{1}{2}, \tag{2.78}$$

which gives

$$\sigma = \frac{\gamma_D}{\sqrt{2\ln(2)}}. \tag{2.79}$$

31

The Doppler line shape, $\phi_D(\nu)$, describes the fraction of molecules that emit radiation at wavenumber ν. Therefore, ϕ_D is defined as

$$\phi_D(\Delta\nu) \equiv \frac{1}{N}\frac{dN(\nu)}{d\nu} = \sqrt{\frac{\ln(2)}{\pi}}\frac{1}{\gamma_D}\exp\left(-\frac{\ln(2)(\Delta\nu)^2}{\gamma_D^2}\right), \qquad (2.80)$$

where Equation (2.79) was inserted into Equation (2.76) and frequency was converted to wavenumber. At higher altitudes where fewer collisions occur, Doppler broadening is the dominate effect.

Voigt Lineshape

At altitudes where both Doppler and Lorentz broadening must be accounted for, the combination of both effects is achieved by a convolution of their line shapes:

$$\phi_V(\Delta\nu) = \int_{-\infty}^{\infty} \phi_D(\Delta\nu')\phi_L(\Delta\nu - \Delta\nu')d\Delta\nu'. \qquad (2.81)$$

This line shape is called the Voigt function and is the default line shape used by SASK-TRAN. It allows accurate modelling of broadening effects without needing to switch between Lorentz and Doppler line shapes at different pressure levels. During a single radiative transfer calculation, Equation (2.81) will be evaluated thousands of times for different spectral lines at various temperatures and pressures. Therefore, several efficient algorithms have been developed to compute this integral, with SASKTRAN using an algorithm designed by Kuntz (1997).

2.3.5 Absorption Cross Section

It is now possible to calculate a line-by-line absorption cross section $\sigma_a(\nu)$ for a wavenumber ν. The contribution from each spectral line is equal to the spectral line intensity multiplied by the line shape function. Summing over all spectral lines gives

$$\sigma_a(\nu) = \sum_i S_{lu,i}(T)\phi_V(\nu_{lu,i} - \nu, T, p). \qquad (2.82)$$

Which lines are included in the summation depends on the calculation. Typically, all spectral lines in a wavenumber window near ν are included. The optimal size of this window depends on the amount of broadening that is applied to nearby lines, which in turn depends on the

temperature and pressure at a given point. However, a window extending to include lines where $\nu_{lu,i}$ is within 50 cm^{-1} of ν is a good starting point. In practice there is a trade off between specifying a larger spectral window with longer computation times and reducing the size of the window at the cost of the accuracy of the model results. Selection of the spectral window size requires careful consideration of the broadening effects, spectral line intensities, and species involved in the cross section calculation. Further approximations may also be performed by excluding lines with comparatively small intensities.

2.4 LIFE Instrument

The Limb Imaging Fourier transform spectrometer Experiment (LIFE) is a balloon-based instrument developed at the University of Saskatchewan. It is an early prototype for a future satellite instrument. This instrument measures interferograms of light at thermal infrared wavelengths in the 7 to 14 μm range, which are converted to radiances using the techniques of Fourier transform spectroscopy. A detector consisting of a single row of photoconductors allows for simultaneous measurements from 16 different tangent altitudes. The concept for LIFE is similar to that of the Gimballed Limb Observer for Radiance Imaging of the Atmosphere (GLORIA), which instead implements a two-dimensional array of detectors (Friedl-Vallon et al., 2014). Both instruments use attached blackbodies of known temperature to calibrate their measurements.

2.4.1 Michelson Interferometer

The primary component of the LIFE optical system is a Michelson interferometer. A simple Michelson interferometer consists of two mirrors, a beam splitter, and a detector. The beam splitter separates incoming light along two paths. A mirror is placed perpendicular to each path so that the light is reflected back towards the beam splitter. At the beam splitter, the two light paths recombine and their intensity is measured by a detector. One of the mirrors is fixed and the other is adjustable, allowing the distance that light travels on one path to be varied. This configuration makes it possible to measure the intensity of light as a function of the path difference between the two arms of the detector. A diagram of a Michelson
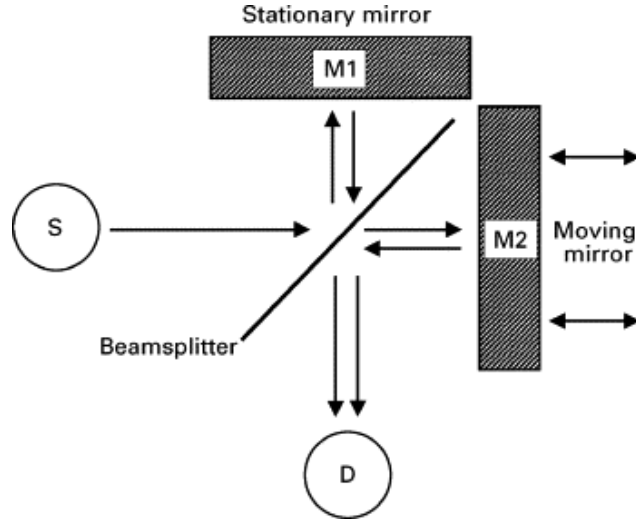
Figure 2.4: Diagram of a Michelson interferometer. S is a source of collimated light and D is a detector (Shaw and Mantsch, 1999).

interferometer is shown in Figure 2.4.

Consider a monochromatic light source with a wavelength λ_0. If the moveable mirror is positioned at a point where both paths are of equal distance, the two paths of light will interfere constructively because the phase difference between waves is zero. This mirror position is called the zero path difference (ZPD) where the intensity of the interference pattern is at a maximum. As the mirror is moved, the non-zero path difference results in a phase offset between the combining light waves. When the mirror is moved a distance $\lambda_0/4$ from the ZPD, the optical path difference (OPD) is now $\lambda_0/2$ because the light must travel from the beam splitter to the mirror and back to the beam splitter before recombining with the other path. At this mirror position, interference between the two paths is perfectly destructive and an intensity of zero is measured by the detector. Moving the mirror a distance $\lambda_0/2$ from the ZPD then results in an OPD of λ_0, such that the waves will once again interfere constructively. In general, as the mirror is moved further away from the ZPD point, there will be intensity peaks due to constructive interference when the OPD is $n\lambda_0$ for integer values of n. Similarly, intensity minimums will be measured for OPD values of $(n + 1/2)\lambda_0$.

Assume that the incoming light is perfectly collimated and can therefore be described as an electromagnetic plane wave. When the plane is incident on the beam splitter, it is divided into two plane waves with angular frequency ω_0 and amplitude A, assuming exactly 50% of

the incoming light passes through the beam splitter while the remaining 50% is reflected. Let the direction of propagation be z. The electric field equations for these plane waves are

$$E_1(z,t) = Ae^{i(k_0 z - \omega_0 t - \phi_1)},$$
$$E_2(z,t) = Ae^{i(k_0 z - \omega_0 t - \phi_2)}. \tag{2.83}$$

The wavenumber is given by k_0 and each wave has a phase ϕ. When the waves interfere with one another, the resulting plane wave is described by the superposition of their electric fields,

$$E(z,t) = E_1 + E_2 = Ae^{i(k_0 z - \omega_0 t)}(e^{-i\phi_1} + e^{-i\phi_2}). \tag{2.84}$$

The intensity measured by the detector is proportional to the square of the electric field,

$$I \propto A^2 e^{i(k_0 z - \omega_0 t)}(e^{-i\phi_1} + e^{-i\phi_2})e^{-i(k_0 z - \omega_0 t)}(e^{i\phi_1} + e^{i\phi_2}),$$
$$I \propto A^2 \left(2 + e^{i(\phi_2 - \phi_1)} + e^{-i(\phi_2 - \phi_1)}\right), \tag{2.85}$$
$$I \propto 2A^2(1 + \cos(\phi_2 - \phi_1)).$$

The phase difference, $\phi_2 - \phi_1$, is a result of the optical path difference. Therefore, it is equal to the number of radians per unit distance, k_0, multiplied by the optical path difference, x. Expressing the angular wavenumber, k_0, in terms of the spectroscopic wavenumber, $k_0 = 2\pi\nu_0$, results in an expression for the monochromatic intensity measured by the detector as a function of the path difference,

$$I_0(x) = I(\nu_0)(1 + \cos(2\pi\nu_0 x)), \tag{2.86}$$

where $I(\nu_0)$ is the intensity of the light source.

It is straightforward to extend the monochromatic form of Equation (2.86) to include more than a single wavelength, or wavenumber. The polychromatic interferogram is a superposition of the interferograms from all wavenumbers,

$$I_p(x) = \int_0^\infty I(\nu)(1 + \cos(2\pi\nu x))d\nu. \tag{2.87}$$

Equation (2.87) describes the interference pattern measured by a detector, which consists of a constant term, $I(\nu)$, multiplied by a modulating term that depends on the OPD and the wavelength of the incoming light. Subtracting the average intensity results in

$$I(x) = I_p(x) - \overline{I_p(x)} = \int_0^\infty I(\nu)\cos(2\pi\nu x)d\nu. \tag{2.88}$$

Equation (2.88) is particularly useful because it has the form of Fourier cosine transform. Therefore, it is possible to determine the spectral intensity, $I(\nu)$, by inverse Fourier transform,

$$I(\nu) = \int_0^\infty I(x) \cos(2\pi\nu x)\mathrm{d}x. \tag{2.89}$$

Equations (2.88) and (2.89) describe the theoretical foundation of Fourier transform spectroscopy, a technique which makes it possible to extract spectra from interferograms of light.

2.4.2 LIFE Optical Design

A commercial MB3000 interferometer manufactured by ABB is adapted for use in the LIFE optical system. The MB3000 uses the same concept as a traditional Michelson interferometer, but with a few changes to make the instrument more compact and mechanically stable. Instead of using a fixed mirror and a moving plane mirror, the incoming light is reflected back to the beam splitter from corner cubes attached to the arms of a rotating motor, enabling pendulum-like motion of the cubes about the fixed beam splitter. Rotating the system brings one reflecting cube closer to the beam splitter while the other cube is simultaneously moved further away. This configuration makes it possible to achieve larger path differences in a smaller range of motion. The reflecting corner cubes ensures that light is always reflected directly back towards the beam splitter, regardless of the positions of the rotating arms. A model of the MB3000 used in LIFE is shown in Figure 2.5, where dark blue lines trace the path of light through the interferometer. The MB3000 makes use of ABB patented designs to reduce the effect of instrument self emission on the measured signal (Buijs, 2012; Theriault, 2001). Self emissions refer to the thermal emissions from instrument components which can be measured by the detector and need to be removed in the measurement calibration.

After passing through the interferometer, light is focused onto a one dimensional array of 16 photodetectors. The detectors are constructed from mercury cadmium telluride (MCT), a photoconductive material that is sensitive to infrared wavelengths. MCT detectors are most sensitive to wavelengths in the 8 to 14 μm range, making them effective in the thermal infrared regime (Shen, 1994).
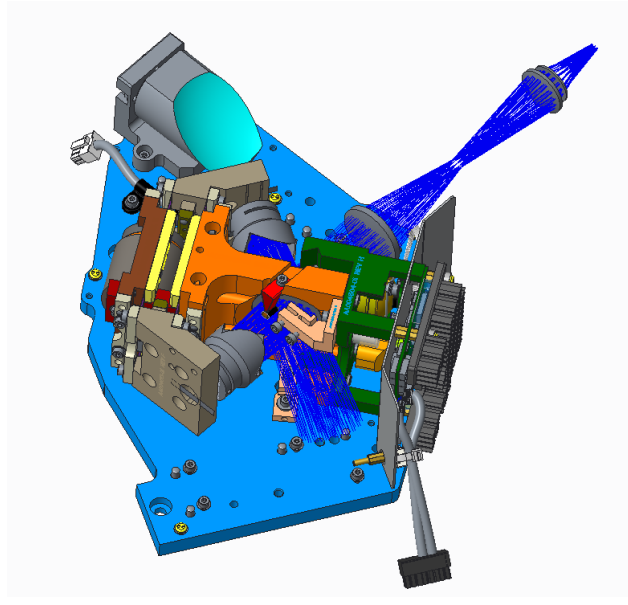
Figure 2.5: Model of the ABB MB3000 interferometer unit implemented by LIFE. Dark blue lines trace the path of light through the system.

2.4.3   Limb Imaging

Many existing remote sensing instruments that measure radiance through the atmospheric limb use a scanning technique to take measurements over a range of tangent altitudes. The scanning process takes time which results in horizontal separation between altitude points as the instrument observation platform travels during the scan. For example, the microwave limb sounder (MLS) on board the Aura satellite performs a complete vertical scan from the surface of the Earth to a tangent altitude of 90 km in 24.7 seconds from a spacecraft altitude of 705 km (Read et al., 2004). The tangent points of the vertical profile measured during this scan can have horizontal separations as large as 50 km due to the movement of the satellite. Recent instruments, such as GLORIA, use imaging techniques wherein measurements along multiple lines of sight are performed simultaneously by using an array of detectors. LIFE is designed to operate similarly to GLORIA by using an array of detectors to vertically image the atmospheric limb.

2.5 Retrieval Theory

The primary goal of remote sensing instruments is to determine the state of the atmosphere from measurements of spectral radiance. Retrieving a quantity, such as temperature or ozone density, from measurements requires knowledge of the physical relationship between the measurement and atmospheric state. However, it is difficult to directly solve for the desired quantity because this relationship is generally nonlinear, making it impossible to directly solve for atmospheric state. This section describes the application of inverse theory to solving this nonlinear problem. The discussion of inverse theory presented in this section follows the formulation by Rodgers (2000).

2.5.1 The Inverse Problem

Inverse theory deals with the problem of solving for a quantity, $\vec{x}$, given a measurement, $\vec{y}$. Note that $\vec{x}$ and $\vec{y}$ are vectors that do not need to contain the same number of elements. The inverse problem states that $\vec{x}$ and $\vec{y}$ are related by

$$\mathbf{f}(\vec{x}, \vec{b}) = \vec{y} + \epsilon, \tag{2.90}$$

where $\mathbf{f}$, called the forward function, describes the physical relationship between $\vec{x}$ and $\vec{y}$. Any additional information that affects the forward function but is not being solved for is contained in $\vec{b}$, and ϵ is the measurement error. To develop a framework for handling the nonlinear problem, first consider the linear solution for $\vec{x}$.

2.5.2 Linear Problems

If the system is assumed to be linear, Equation (2.90) can be rewritten as

$$\vec{y} = \mathbf{K}\vec{x}, \tag{2.91}$$

where $\mathbf{K}$ is a matrix. Measurement error is ignored for now and will be discussed in Section 2.5.3. If there are m measurements in $\vec{y}$, and n target quantities in $\vec{x}$, the dimensions of $\mathbf{K}$ are $m \times n$. In the simplest case where $m = n$, $\vec{x}$ can be solved for directly because $\mathbf{K}$ is a

square matrix and therefore invertible,

$$\vec{x} = \mathbf{K}^{-1}\vec{y}. \tag{2.92}$$

When $n > m$, the problem is underdetermined because there exists an infinite number of solutions that satisfy Equation (2.91). Finding the best solution in this case requires a more nuanced approach in which constraints must be placed on the solution. These constraints are often based on pre-existing knowledge about how the solution is expected to behave and which solutions are physically reasonable. For example, restrictions are often placed on the smoothness of the first and second derivatives of the solution, as discussed in Section 2.5.4.

In the final case where $m > n$ the problem is overdetermined and no exact solution exists. However, it is possible to determine a solution for $\vec{x}$ which best satisfies Equation (2.90). The general method is to define a cost function, χ^2, which increases as the difference between the measurements, $\vec{y}$, and the output of the forward function, $\mathbf{K}\vec{x}$, increases. A least squares difference is commonly used, resulting in a cost function of

$$\chi^2 = (\vec{y} - \mathbf{K}\vec{x})^T(\vec{y} - \mathbf{K}\vec{x}). \tag{2.93}$$

By setting the derivative with respect to the target variable, $\vec{x}$, to 0 it is possible to solve for the value of $\vec{x}$ that minimizes the cost function. The derivative of Equation (2.93) is

$$\nabla_{\vec{x}}\chi^2 = -\mathbf{K}^T(\vec{y} - \mathbf{K}\vec{x}) - (\vec{y} - \mathbf{K}\vec{x})^T\mathbf{K}. \tag{2.94}$$

Setting $\nabla_{\vec{x}}\chi^2$ equal to 0 and solving for $\vec{x}$ results in the least squares solution to the inverse problem,

$$\vec{x} = (\mathbf{K}^T\mathbf{K})^{-1}\mathbf{K}^T\vec{y}. \tag{2.95}$$

2.5.3 Measurement Uncertainty

Measurements contain uncertainty due to instrument noise. Therefore, each measurement y can be interpreted as a random variable with an associated probability density function, $P(y)$. From probability theory, the measurement has an expected value given by

$$\overline{y} = \int yP(y)\mathrm{d}y, \tag{2.96}$$

and variance given by

$$\sigma^2 = \int (y - \bar{y})^2 P(y) \mathrm{d}y. \tag{2.97}$$

Assuming a Gaussian distribution, the probability density function is

$$P(y) = \frac{1}{\sqrt{2\pi}\sigma} \exp\left[-\frac{-(y-\bar{y})^2}{2\sigma^2}\right]. \tag{2.98}$$

When multiple measurements are in consideration the scalar variance, σ^2, is replaced by the covariance matrix, $\mathbf{S}_y$, which is defined as

$$S_{y,ij} = \int (y_i - \overline{y_i})(y_j - \overline{y_j}) P(y) \mathrm{d}y, \tag{2.99}$$

for the element in the ith row and jth column. The Gaussian probability density function which describes this measurement vector then has the following form

$$P(\vec{y}) \sim \exp\left[-\frac{1}{2}(\vec{y}-\bar{\vec{y}})^T \mathbf{S}_y^{-1}(\vec{y}-\bar{\vec{y}})\right]. \tag{2.100}$$

The expected value $\bar{\vec{y}}$ can be estimated as $\mathbf{K}\vec{x}$ from Equation (2.91). This estimation produces an expression which describes the probability of obtaining measurement $\vec{y}$ for a given value of $\vec{x}$,

$$P(\vec{y}|\vec{x}) \sim \exp\left[-\frac{1}{2}(\vec{y}-\mathbf{K}\vec{x})^T \mathbf{S}_y^{-1}(\vec{y}-\mathbf{K}\vec{x})\right]. \tag{2.101}$$

In this probabilistic interpretation, the best solution to the inverse problem is one which maximizes the value of Equation (2.101). This is known as the maximum likelihood solution. Maximizing the value of $P(\vec{y}|\vec{x})$ can be achieved by minimizing the cost function,

$$\chi^2 = (\vec{y}-\mathbf{K}\vec{x})^T \mathbf{S}_y^{-1}(\vec{y}-\mathbf{K}\vec{x}). \tag{2.102}$$

As before, set $\nabla_{\vec{x}}\chi^2 = 0$ to determine the value of $\vec{x}$ which minimizes the cost function. The resulting maximum likelihood solution is

$$\vec{x} = (\mathbf{K}^T \mathbf{S}_y^{-1}\mathbf{K})^{-1}\mathbf{K}^T \mathbf{S}_y^{-1}\vec{y}. \tag{2.103}$$

The solution successfully incorporates measurement uncertainty into the least squares approach, but it is unable to handle cases where $\mathbf{K}^T \mathbf{S}_y^{-1}\mathbf{K}$ is not invertible. This cases occurs when the problem is underdetermined, for which the solution is to add additional information or constraints to the problem in a process known as regularization.

2.5.4   Regularization

The additional information is called a priori information and contains pre-existing knowledge about the solution, denoted $\vec{x}_a$. Introducing a priori information with covariance $\mathbf{S}_a$ adds an extra term to the cost function,

$$\chi^2 = (\vec{y} - \mathbf{K}\vec{x})^T \mathbf{S}_y^{-1} (\vec{y} - \mathbf{K}\vec{x}) + (\vec{x} - \vec{x}_a)^T \mathbf{S}_a^{-1} (\vec{x} - \vec{x}_a), \qquad (2.104)$$

and the solution is

$$\vec{x} = \vec{x}_a + (\mathbf{K}^T \mathbf{S}_y^{-1} \mathbf{K} + \mathbf{S}_a^{-1})^{-1} \mathbf{K}^T \mathbf{S}_y^{-1} (\vec{y} - \mathbf{K}\vec{x}_a). \qquad (2.105)$$

The process of adding a priori information is a form of regularization. Adding the $\mathbf{S}_a^{-1}$ term in Equation (2.105) ensures that $\mathbf{K}^T \mathbf{S}_y^{-1} \mathbf{K} + \mathbf{S}_a^{-1}$ is invertible. Several options exist for selecting appropriate values for $\vec{x}_a$ and $\mathbf{S}_a$. One option is to choose $\vec{x}_a$ to be the expected result or a result from similar experiments. For example, if $\vec{x}$ corresponds to an ozone density profile, $\vec{x}_a$ could be obtained from an atmospheric climatology. There are several drawbacks to this option, including potentially inaccurate climatologies and difficulty in determining an appropriate $\mathbf{S}_a$.

Tikhonov (1943) suggested a method where the derivative of the solution is constrained. Let $\mathbf{S}_a = \Gamma^T \Gamma$ where Γ is a matrix operator which computes the derivative of the solution $\vec{x}$. For example, using a finite difference method the matrix is

$$\Gamma = \alpha \begin{pmatrix} 1 & -1 & 0 & 0 & 0 & \dots \\ 0 & 1 & -1 & 0 & 0 & \dots \\ 0 & 0 & 1 & -1 & 0 & \dots \\ & & & & \ddots \end{pmatrix}, \qquad (2.106)$$

where α is a scalar parameter used to control the magnitude of the regularization. Similarly, the second derivative of the solution can be constrained by setting Γ to

$$\Gamma = \alpha \begin{pmatrix} -1 & 2 & -1 & 0 & 0 & \dots \\ 0 & -1 & 2 & -1 & 0 & \dots \\ 0 & 0 & -1 & 2 & -1 & \dots \\ & & & & \ddots \end{pmatrix}. \qquad (2.107)$$

In the retrieval of profiles of atmospheric species these derivatives are typically with respect to changes in altitude, as $\vec{x}$ is the concentration of the target species for a range of altitudes.

2.5.5 Nonlinear Problems

In linear systems it is possible to rewrite the inverse problem in the form of Equation (2.90). For nonlinear systems, this formulation is not possible and the forward function, $\mathbf{f}(\vec{x})$, is instead approximated using a forward model, $\mathbf{F}(\vec{x})$. The same process used in Sections 2.5.3 and 2.5.4 can be used to define the following cost function for nonlinear problems,

$$\chi^2 = (\vec{y} - \mathbf{F}(\vec{x}))^T \mathbf{S}_y^{-1}(\vec{y} - \mathbf{F}(\vec{x})) + (\vec{x} - \vec{x}_a)^T \mathbf{S}_a^{-1}(\vec{x} - \vec{x}_a). \tag{2.108}$$

As before, the cost function is minimized by setting $\nabla_{\vec{x}}\chi^2 = 0$,

$$\nabla_{\vec{x}}\chi^2 = -[\nabla_{\vec{x}}\mathbf{F}(\vec{x})]^T \mathbf{S}_y^{-1}[(\vec{y} - \mathbf{F}(\vec{x}))] + \mathbf{S}_a^{-1}(\vec{x} - \vec{x}_a) = 0. \tag{2.109}$$

Unlike the linear case, it is not possible to solve Equation (2.109) directly for $\vec{x}$. Newton's iterative method can be used to approximate the roots of this equation.

First, some definitions are required to simplify the following expressions. Define the matrix $\mathbf{K}$ as

$$\mathbf{K}(\vec{x}) = \nabla_{\vec{x}}\mathbf{F}(\vec{x}). \tag{2.110}$$

$\mathbf{K}(x)$ is called the Jacobian matrix and its calculation is discussed in Section 2.5.6. Let $g(\vec{x})$ be the function whose roots are being approximated. Substituting Equation (2.110) into (2.109) gives

$$g(\vec{x}) = -\mathbf{K}^T \mathbf{S}_y^{-1}[(\vec{y} - \mathbf{F}(\vec{x}))] + \mathbf{S}_a^{-1}(\vec{x} - \vec{x}_a) = 0. \tag{2.111}$$

Newton's method for improving the root approximation from the result of the previous iteration, $\vec{x}_i$, is

$$\vec{x}_{i+1} = \vec{x}_i - [\nabla_{\vec{x}}g(\vec{x}_i)]^{-1}g(\vec{x}_i). \tag{2.112}$$

Calculating the gradient of $g(\vec{x})$ results in

$$\nabla_{\vec{x}}g(\vec{x}) = \mathbf{K}^T \mathbf{S}_y^{-1}\mathbf{K} + \mathbf{S}_a^{-1} - [\nabla_{\vec{x}}\mathbf{K}^T]\mathbf{S}_y^{-1}[\vec{y} - \mathbf{F}(\vec{x}_i)]. \tag{2.113}$$

Note that the term $\nabla_{\vec{x}}\mathbf{K}^T$ in Equation (2.113) requires the computation of second order derivatives of $\mathbf{F}(\vec{x})$. Calculating or finding analytical expressions for these second order

derivatives can be difficult or impossible in many cases. The Gauss-Newton modification of Newton's method fixes this issue by assuming that $\nabla_{\vec{x}}\mathbf{K}^T = 0$, which is the case in linear systems. For systems that are only moderately nonlinear, the Gauss-Newton method provides a reasonably good approximation. Using this assumption and substituting Equations (2.111) and (2.113) into (2.112) produces

$$\vec{x}_{i+1} = \vec{x}_i + (\mathbf{K}_i^T \mathbf{S}_y^{-1} \mathbf{K}_i + \mathbf{S}_a^{-1})^{-1} [\mathbf{K}_i^T \mathbf{S}_y^{-1} [\vec{y} - \mathbf{F}(\vec{x}_i)] - \mathbf{S}_a^{-1}(\vec{x}_i - \vec{x}_a)]. \qquad (2.114)$$

Equation (2.114) is a key equation in nonlinear inverse theory and is the form often used when retrieving vertical profiles of target quantities from remote sensing experiments.

2.5.6 The Jacobian Matrix

Given m measurements and n target variables the Jacobian matrix, $\mathbf{K}$, defined in Equation (2.110) has dimensions of $m \times n$. The element in the ith row and jth column of $\mathbf{K}$ is

$$\mathbf{K}_{ij} = \frac{\partial \mathbf{F}(\vec{x})_i}{\partial \vec{x}_j}, \qquad (2.115)$$

which describes how the forward model approximation of measurement y_i is affected by changes in the state parameter x_j. Jacobians are extremely important in the iterative solution because they inform the solver whether the target parameters should be increased or decreased in the forward model to produce a result closer to the measurement.

It is possible to calculate the Jacobian using numerical methods, in which the forward model is run with the jth element of $\vec{x}$ perturbed by an amount δx_j. Using a forward difference approximation of the derivative, the Jacobian elements are

$$\mathbf{K}_{ij} \approx \frac{\mathbf{F}(x_1, ..., x_j + \delta x_j, ..., x_n)_i - \mathbf{F}(x_1, ..., x_j, ..., x_n)_i}{\delta x_j}. \qquad (2.116)$$

An important consideration when using this perturbation method is that the forward model must be run an additional n times, once for each element in $\vec{x}$. In complicated physical models this results in inconveniently large computation times. As a solution, many models implement analytic Jacobian which divide the Jacobian calculations into smaller pieces that can be calculated simultaneously with the primary model output. Typically, this method involves using the chain rule to split up the forward model derivatives. The use of analytic

Jacobians in a thermal infrared radiative transfer model is the primary focus of this thesis and the details of their implementation in the SASKTRAN framework are given in Chapter 4.

2.6   The SASKTRAN Radiative Transfer Framework

SASKTRAN is a set of software tools for configuring a model atmosphere and solving the radiative transfer equation. Its basic functionality is to return the calculated radiance after the user inputs a position, look direction, wavelength, and atmospheric state. SASKTRAN is developed in C++ using an object-oriented approach, making the code base highly modular and simplifying the development of new features. Additionally, a Python package has been developed as a wrapper around the C++ code. This package provides a user-friendly interface for interacting with SASKTRAN and is the primary method through which the software is utilized. The subject of this work involves the implementation of a new Thermal InfraRed (TIR) engine into the framework, including a core C++ implementation with Python wrappers.

2.6.1   Engines

In SASKTRAN, the main object which performs the radiative transfer calculation is known as an *engine*. There are several engines available, with each one utilizing different techniques for calculating the radiance.

The Successive Orders (SO) engine computes the radiance in Equation (2.9) using the original SASKTRAN algorithm described by Bourassa et al. (2008). As its name suggests, the successive orders technique described in Section 2.2.2 is used to simulate photons that undergo multiple scattering events before being scattered into the line of sight. To perform the numerical integration of Equation (2.9), the line of sight must be split into a number of segments, also known as cells. Atmospheric properties, such as gas densities, are considered constant within a given cell. The cells are determined by locating intersections between the line of sight and geometric objects used to partition the atmosphere into homogeneous layers. Usually, the atmosphere is represented by concentric spherical shells, with a typical spacing

of 1 km between shell borders. The process of determining these intersections is called ray tracing and produces a set of distances measured from the observer to the boundary of each spherical shell intersected by the line of sight. If the distances are labelled sequentially from s_1 to s_N, starting with s_1 closest to the observer, the radiance is

$$I = \sum_{j=1}^{N} e^{-\tau(s_j,0)} I_j, \tag{2.117}$$

where I_j is the radiance contribution from cell j, attenuated by $e^{-\tau(s_j,0)}$ where $\tau(s_j,0)$ is the optical depth between the observer and cell j. From the radiative transfer equation ((2.9)), the single cell contribution is

$$I_j = \int_{s_{j+1}}^{s_j} e^{-k(s)(s-s_j)} J(s)\mathrm{d}s. \tag{2.118}$$

In the SO engine, the extinction $k(s)$ and source function $J(s)$ are assumed to be constant across each cell. Their values are calculated at the midpoint of the cell, given by $(s_{j+1}+s_j)/2$.

The High Resolution (HR) engine calculates the radiance using the successive orders method and succeeds the SO engine as the primary SASKTRAN engine for calculations at visible and near infrared wavelengths. The engine includes a number of techniques to increase the accuracy of the numerical integration (Zawada et al., 2015). First, $k(s)$ is allowed to vary linearly with altitude across a cell, instead of being assumed constant. Similarly, instead of assuming a constant source term in each cell, a second order polynomial function is used to smoothly interpolate the source function across the segment. Lastly, an adaptive technique subdivides cells along the integration path if either the optical depth or the extinction gradient of a single segment exceed configurable thresholds. The extinction gradient is computed as

$$\frac{\min(k(s_j), k(s_{j+1}))}{\max(k(s_j), k(s_{j+1}))}. \tag{2.119}$$

Decreasing the path length through a cell reduces errors that arise from assuming a constant or linearly changing extinction and a constant or quadratic source function within each cell.

The Monte Carlo (MC) engine uses a different method for calculating the radiance in which the paths of photons are determined in reverse order, beginning at the observer. It was designed to test the accuracy of the HR engine by calculating an unbiased estimate of the radiance. The details of the MC engine implementation are described by Zawada et al. (2015).

The existing SASKTRAN engines are optimized for the visible and near infrared regimes and are capable of accurately and efficiently calculating the scattering of sunlight. The Thermal InfraRed (TIR) engine aims to extend SASKTRAN's capabilities to larger wavelengths. The development of this new engine is described in Chapter 3.

2.6.2   Interface

All SASKTRAN engines feature a similar interface, in which the user creates an engine object of the desired type and provides three main inputs: an *atmosphere*, *geometry*, and target *wavelengths*.

The atmosphere contains all of the species that will be relevant to the radiative transfer calculation. Each species must be described by a *climatology* and *optical property*. A climatology specifies the quantity of a species, such as the number density of scattering neutral particles, as a function of time and position. Typically, climatologies describe how the species varies with height but can also include variations in latitude, longitude, and time. An optical property defines the scattering and absorption properties of the species. For example, a valid optical property for the neutral air species is Rayleigh scattering. Optical properties for calculating infrared absorption cross sections implement the HITRAN database as discussed in Section 2.3.3.

The geometry contains all of the lines of sight for which to compute the radiance. A line of sight contains an observer position, time, and look direction. Lines of sight may be curved to account for refraction as a result of the varying refractive index of atmospheric air. The solar position may also be specified, or SASKTRAN may infer it from the times given in the lines of sight.

2.6.3   Internals

One of the goals in the development of the SASKTRAN radiative transfer framework is to create a reuseable set of tools which greatly simplifies the addition of new engines and provides a consistent user experience throughout the framework. An example of this idealogy is the ability to use the same climatology and optical property interfaces with different

engines. Internally, the core SASKTRAN code base provides a number of generic classes which provide functionality required by most radiative transfer algorithms, or engines. The components most relevant to the development of the TIR engine are described in the following sections.

Atmosphere Geometry

An important component of the radiative transfer model is the representation of Earth and its atmosphere. It is convenient to perform the calculation in a spherical geometry, in which the planetary surface is assumed to be a perfect sphere. However, the since the Earth is not perfectly spherical this assumption requires consideration of the variations in the planetary radius. For each radiative transfer calculation SASKTRAN selects a reference point on the surface of the Earth's geoid. In a limb-viewing geometry this reference point is directly below the tangent point. The spherical Earth used in the model is created with curvature equal to the true geoid at the reference point, also known as an osculating sphere.

Models have been developed to approximate the Earth by an ellipsoidal shape. The default reference ellipsoid used by the SASKTRAN internal coordinate system is the World Geodetic System (WGS) 1984 (Decker, 1986). WGS 84 has been utilized in Global Positioning Systems and is generally accurate to within 2 meters (True, 2004). Given that the modelled atmosphere is assumed to be homogeneous within layers that are typically 500 meters across in altitude, WGS 84 offers good precision.

Ray Tracing

Computing the radiative transfer integral numerically as in Equation (2.117) requires that the atmosphere be partitioned into sections in which atmospheric variables are assumed to be constant or varying according to some known function, as in the HR modifications to the extinction and source functions described in Section 2.6.1. In SASKTRAN, the layers are initially defined by concentric spherical shells. The spacing between shells is adjustable, but typically set to a value between 100 and 1000 meters.

Ray tracing is the process of dividing a line of sight into segments, or cells, for the numerical integration. Ignoring atmospheric refraction for the moment, the line of sight is a

straight line. Therefore, the intersection of this line with a spherical shell can be determined analytically. A point along the line of sight is defined as $\vec{r} + \hat{p}s$, where $\vec{r}$ is the vector from the origin to the observer, $\hat{p}$ is the unit vector in the observer's look direction, and s is the distance to the point from the observer. For a sphere with radius R centered on the origin of the coordinate system, the intersections will be the values of s which produce a magnitude of R, resulting in the following expression,

$$R = \|\vec{r} + \hat{p}s\|,$$
$$R = \sqrt{\|\vec{r}\|^2 + 2s\hat{p} \cdot \vec{r} + s^2}.$$
(2.120)

Solving for s:

$$s = -(\hat{p} \cdot \vec{r}) \pm \sqrt{(\hat{p} \cdot \vec{r})^2 - (\|\vec{r}\|^2 - R^2)}.$$
(2.121)

In general there are two intersection points, but with some special cases taken into consideration. For example, if the line of sight intersects the ground the second intersection may be discarded because the line of sight never reaches that point. The intersection is also discarded if s is negative, because this indicates a point in the opposite direction that the observer is looking. Lastly, complex s values indicate that there are no intersections.

While the spherical shells are able to accurately model vertical changes in atmospheric geometry, there can be issues associated with the long horizontal paths that are seen in limb viewing geometries. In particular, the horizontal path lengths through a cell created solely from spherical shell intersections become increasingly large near the tangent point. Over larger distances, errors due to the assumption about the extinction and atmospheric composition become amplified. With the development of the HR and MC engines additional geometric shapes were added to the ray tracing algorithm to improve accuracy near the tangent point. In particular, calculating the intersection of the ray with a cone whose apex is located at the coordinate system origin results in smaller path lengths near the tangent point.

So far we have assumed that the rays being traced are straight lines. However, when refraction due to the variations in the refractive index of air with altitude is considered the ray paths become curved. As altitude increases the density of air particles decreases exponentially, resulting in a decrease in the refractive index of air. At standard temperature

and temperature (STP) the refractive index is 1.000293, although there are small variations depending on wavelength (Hecht, 2002). Its value becomes closer to 1 as altitude is increased and approaches the vacuum of space. Therefore, ray paths will be curved towards the surface of the Earth. The result is that in a limb-viewing experiment the observer "sees" radiation from a lower tangent altitude than the straight line geometry of their look direction would suggest.

Since the atmospheric refractive index changes with altitude, it is difficult to analytically determine the intersection points of the curved line of sight with the geometric objects that construct the boundaries of the model atmosphere. In SASKTRAN, a piecewise method is used to trace the ray path through a refractive atmosphere. The algorithm uses equations developed by Thompson et al. (1982) to calculate the effective path length and deflection angle for each cell. Calculation of the path length accounts for the curved path of the ray through the cell, allowing for more precise calculation of the optical depth of each cell. The deflection angle describes how much the pointing direction of the ray changes through the cell. It is the angle between the vector defined by a straight path through the cell and the vector pointing from entry point to the exit point of the curved ray through the cell. Calculation of the deflection angle is necessary to determine the point where the ray exits each cell. When refraction is neglected it is sufficient to store the scalar distance s for each intersection, but in the refraction case the vector pointing to each intersection is saved.

3 ENGINE DEVELOPMENT

The existing engines in the SASKTRAN framework are capable of simulating radiative transfer in the ultraviolet, visible, and near-infrared spectral regimes by modelling multiply scattered sunlight. In this chapter, the extension of the framework to longer infrared wavelengths is described and consists of two main topics. Section 3.1 describes the addition of a thermal emission source to the existing High Resolution (HR) engine for radiance simulations that combine scattered sunlight and greenhouse gas emissions. With the addition of thermal emissions the HR engine could be used to model radiances in the thermal infrared regime, but computations of scattered light are time consuming. Furthermore, the HR engine does not compute analytic Jacobians for species absorbing and emitting radiation at infrared wavelengths. Therefore, this thesis includes the development of a new SASKTRAN Thermal InfraRed (TIR) engine for radiative transfer simulations that can ignore scattering of radiation from air particles and incorporates analytic Jacobian calculations for greenhouse gas species. The new TIR engine and its method of computing radiance are described in Section 3.2, while the details of the analytic Jacobian implementation are given in Chapter 4.

3.1 Combining Thermal Emissions and Solar Scattering in the SASKTRAN High Resolution Engine

Spectral measurements in the mid infrared, particularly between 3 and 5 μm, are significantly affected by both solar scattering and thermal emissions. Therefore, a thermal emission source function is implemented into the SASKTRAN C++ code to allow the modelling of this spectral regime. This solution is integrated into the existing framework for the existing HR engine, allowing thermal emissions to take advantage of its multiple scattering capabilities.

The groundwork for the implementation of thermal emissions in the HR engine was provided by Jensen (2015).

3.1.1   Implementation

When the source function, $J(s)$, is computed at a point on a radiative transfer path, s, a thermal emission source term is added to the solar scattering term,

$$J(s) = J_{\text{solar}}(s) + J_{\text{thermal}}(s).\tag{3.1}$$

The thermal radiation emitted by particles in the atmosphere can be approximated using Planck's function for describing the spectral radiance emitted by a black body with temperature T, derived in Appendix B. In SASKTRAN-HR, this function has the form,

$$J_{\text{thermal}}(s) = k_a(s)B(\lambda, T) = k_a(s)\frac{2c}{\lambda^4}\frac{1}{\exp\left(\frac{hc}{\lambda k T(s)}\right) - 1} \quad \left[\frac{\text{photons}}{\text{s cm}^3 \text{ nm sr}}\right],\tag{3.2}$$

where multiplication by the absorption, $k_a(s)$, accounts for the probability of spontaneous and induced emissions. The absorption is computed using parameters from the HITRAN database as described in Section 2.3.

Previously, sunlight entering the atmosphere was the only source of radiation in the HR engine, which allowed a simplification in the internal radiance units used by the model. The radiance units are normalized by the solar irradiance incident on the top of the atmosphere. With sun-normalized units, the radiance from solar scattering can be computed without the need to account for the solar spectrum. The intensity of the solar radiation that reaches Earth varies with the distance between the sun and Earth. Currently, the HR engine returns radiance results in these sun-normalized units, and it is left to the user to multiply by radiance by an appropriate solar spectrum. The use of sun-normalized units in the HR engine makes it necessary to first convert the thermal emission source term to sun-normalized units. This conversion is performed by dividing the thermal source function by a solar spectrum.

3.1.2 Verification

Comparison with Existing Model in the Thermal Infrared

To verify the correctness of the thermal emissions implementation, the radiance computed by SASKTRAN-HR is compared with another model, the Atmospheric Radiative Transfer Simulator (ARTS) (Buehler et al., 2018). ARTS is an open source radiative transfer model primarily developed by the University of Hamburg and Chalmers University. This model is designed for use with instruments measuring at millimeter and sub-millimeter wavelengths. However, ARTS can also model the thermal infrared regime because the underlying physics are the same, with the main source of radiation being thermal emissions from greenhouse gases (Eriksson et al., 2005). ARTS is compatible with the HITRAN database which simplifies the comparison as the molecular parameters needed to calculate absorption cross sections will be identical. This calculation is in the thermal infrared regime where scattered sunlight is negligible, making it a verification test of the thermal source added to the HR engine. It does not test the ability of SASKTRAN-HR to model the combination of solar and thermal sources.

The comparison was set up by creating a single nadir line of sight. An observer is placed at an altitude of 40 km and looks directly downwards at the surface of the Earth. A surface emissivity of 1 is assumed, and ozone is the only species included in the model atmosphere. The ozone density profile is taken from an Air Force Geophysics Laboratory (AFGL) database which provides profiles of atmospheric species for different seasons and latitudinal regions (Anderson et al., 1986). A midlatitude summer profile is chosen for use by both ARTS and SASKTRAN. In this test, the radiance is computed for a wavelength range of 12258 to 13483 nm with resolution of 0.01 nm. The results of the test are plotted in figure 3.1, which shows the raw radiance computed by both models along with the percent difference between the computed radiance. A zoomed in box in the radiance plot shows that spectra are nearly overlapping and the percent difference verifies that the results are agree to around 0.1% or lower.
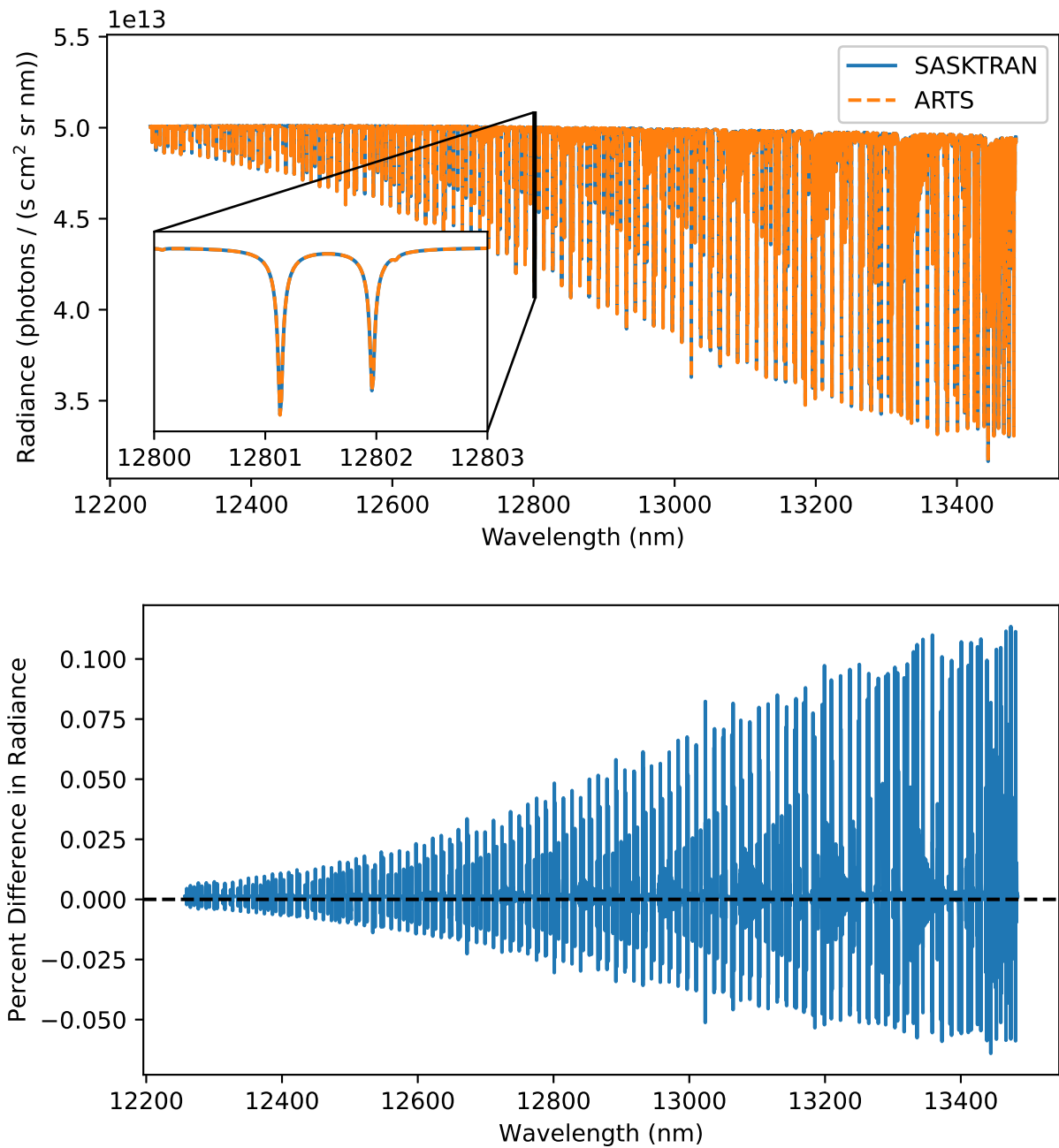
Figure 3.1: Comparison between SASKTRAN-HR and ARTS for a nadir line of sight. Top: simulated radiances with an inset zoomed in on the 12800 to 12803 nm portion of the spectra. Bottom: percent difference of SASKTRAN-HR radiance from ARTS radiance.
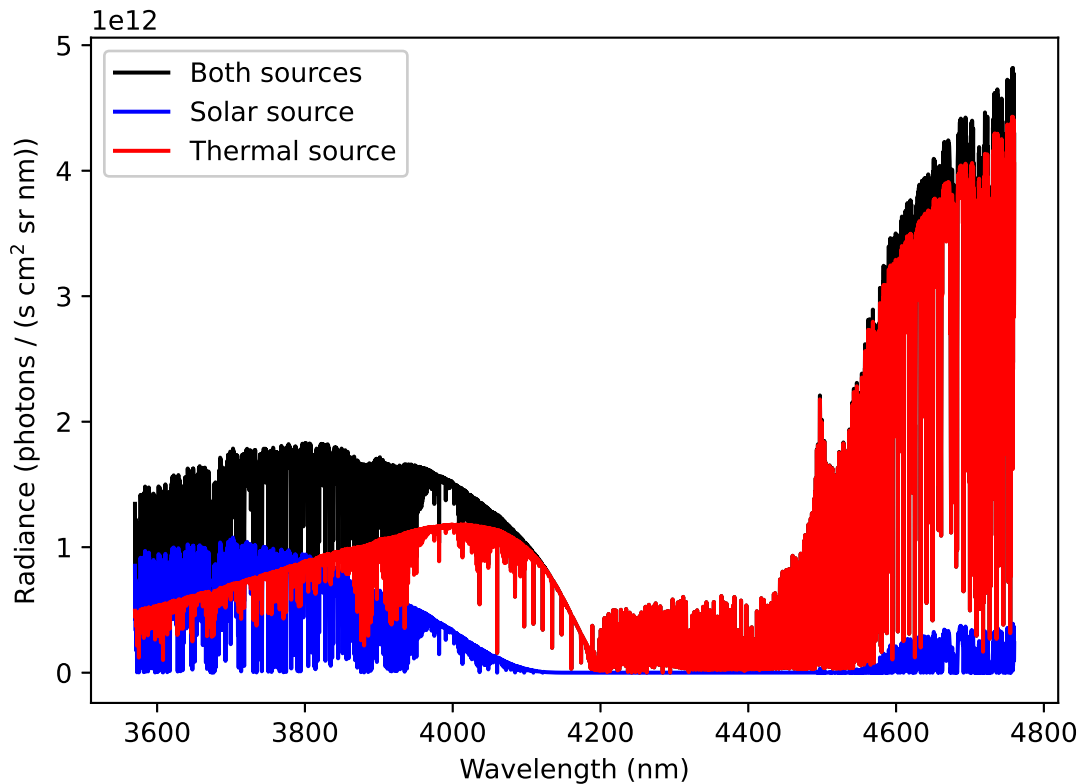
Figure 3.2: Comparison of SASKTRAN-HR radiances modelled by combining solar and thermal radiation sources with each source modelled individually.

Combining Solar and Thermal Sources in the Mid Infrared

With the accuracy of the thermal source verified, it is now possible to demonstrate the combination of thermal and solar sources in the HR engine. Figure 3.2 shows the results from three simulations: one where the only radiation source is scattered sunlight, one where the only source is from thermal emissions, and one with both sources included. This plot shows a spectral region where both results are of similar magnitude. It can be seen that thermal emissions result in a larger magnitude at longer wavelengths and the magnitude from solar scattering increases at shorter wavelengths, as expected. A crossing point between the spectra occurs near 4 μm. Between 4.1 μm and 4.5 μm the radiance is reduced due to carbon dioxide absorption. In this region the carbon dioxide absorption is large enough that the scattered sunlight becomes entirely absorbed and the spectrum is dominated by thermal emissions.
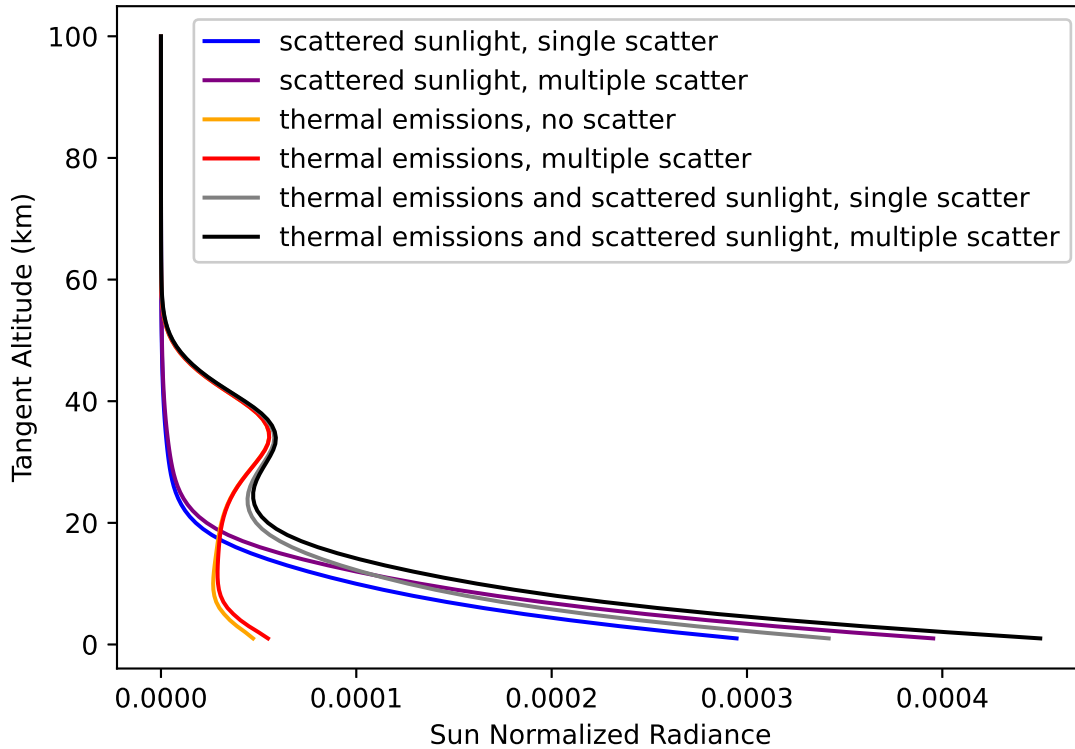
Figure 3.3: Comparison of the radiance profile computed SASKTRAN-HR with different combinations of source terms and scattering order. The radiance is computed at a single wavelength, 3128.6715 nm, at the center of an ozone spectral line.

It is important to consider that for a nadir line of sight the radiance due to the solar source term will be much greater than for a limb view because the reflection of sunlight from the Earth's surface contributes greatly to the nadir radiance. This is demonstrated in Figure 3.3 in which the limb radiance at a single wavelength as a function of tangent altitude is modelled. The wavelength chosen is the centre of a strong ozone spectral line. The plot shows that at higher altitudes thermal emissions dominate the signal while below 20 km scattered sunlight has a larger contribution. At lower altitudes, the higher density of neutral particles results in more scattering events. The peak near 35 km is a result of the large concentration of ozone in the stratosphere. Figure 3.4 shows the temperature and ozone density profiles input to SASKTRAN-HR for the simulations shown in Figure 3.3.
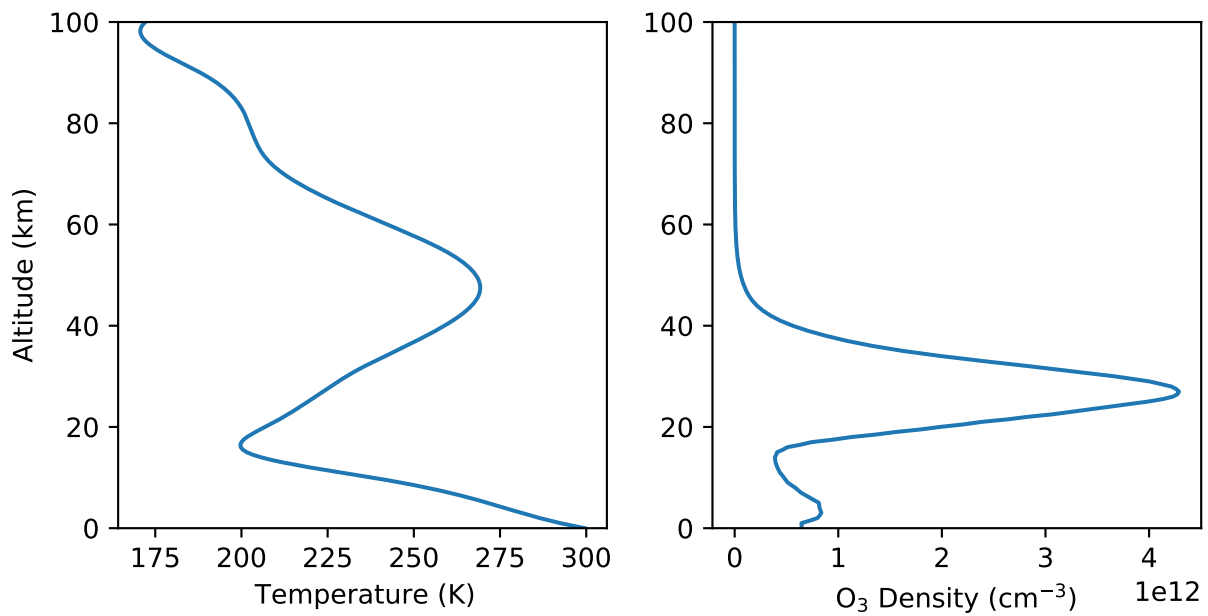
Figure 3.4: Temperature and ozone density profiles input to SASKTRAN-HR to calculate the radiance profiles shown in Figure 3.3.The temperature is provided by the MSIS-90 atmospheric model (Hedin, 1991) while ozone is from a climatology developed by McPeters et al. (1997)

3.2 Developing the SASKTRAN Thermal Infrared Engine

With the addition of thermal emissions, SASKTRAN-HR is capable of simulating radiances in the infrared, including the 7 to 14 μm range from which the LIFE instrument will measure. However, the HR engine is optimized for calculations involving scattering and a relatively low number of wavelengths. Infrared simulations require much higher wavelength resolution to accurately model the absorption cross sections which are complex due to the large number of ro-vibrational energy transitions in this regime. These factors motivated the creation of a new engine, named SASKTRAN Thermal InfraRed (TIR), to provide a fast and accurate forward model for the LIFE instrument. The creation of SASKTRAN-TIR is the primary focus of this thesis and contributes to the LIFE project and future infrared research projects involving the SASKTRAN framework.

3.2.1 Implementation of Radiative Transfer Theory

The differential form of the radiative transfer equation, derived in Section 2.2, is

$$\mathrm{d}I(s) = -I(s)k(s)\mathrm{d}s + J(s)k(s)\mathrm{d}s. \tag{3.3}$$

Since scattered sunlight can be ignored in the TIR regime, the source term, $J(s)$, is equal to the Planck function, $B(s)$, and the extinction, $k(s)$, is equal to the absorption, $k_a(s)$. For simplicity of notation, k will hereafter be used to represent absorption. Consider a small segment of the radiative transfer line of sight and assume a homogeneous atmospheric state within that segment. With this assumption atmospheric state parameters such as species concentrations and radiation source terms are constant across the segment of radiation propagation. The goal is to determine the change in radiation due to a combination of additive thermal emissions and molecular absorption as it is propagated across the segment. Figure 3.5 illustrates this concept, where the indices j and $j + 1$ indicate the start and end points of the segment. If the incoming radiance at point j, I_j, is known, the outgoing radiance at point $j + 1$ can be determined by rearranging Equation (3.3) and integrating across the path
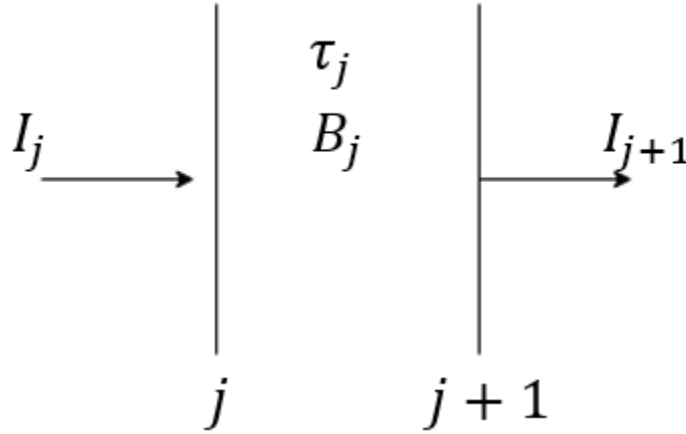
Figure 3.5: Radiative transfer through a homogeneous atmospheric segment

segment,

$$\int_{I_j}^{I_{j+1}} \frac{\mathrm{d}I(s)}{I(s) - B_j} = -\int_{s_j}^{s_{j+1}} k_j ds. \tag{3.4}$$

By assuming a homogeneous atmosphere across the segment, the source term, B_j, and the extinction, k_j, become constant and the expression can be integrated to get

$$\ln\left(\frac{I_{j+1} - B_j}{I_j - B_j}\right) = -k_j(s_{j+1} - s_j). \tag{3.5}$$

The right side of Equation (3.5) can be simplified by recognizing that $s_{j+1} - s_j$ is the length of the path segment, Δs_j. Therefore, the product $k_j \Delta s_j$ is the optical depth of the segment, τ_j, and Equation (3.5) can be rearranged to get an expression for the outgoing radiance of a homogeneous path segment, I_{j+1}, given the incoming radiance, I_j,

$$I_{j+1} = I_j e^{-\tau_j} + (1 - e^{-\tau_j})B_j. \tag{3.6}$$

Equation (3.6) is the basis of the radiative transfer algorithm implemented in the TIR engine. Given an initial radiance at the end of an observer's line of sight, I_0, the observed radiance is calculated by propagating the initial radiance segment by segment. If the line of sight is divided into N segments, the final result of the radiative transfer calculation will be I_N. The initial radiance is determined from the endpoint of the line of sight, which can be either the top of the atmosphere or the planetary surface. If the line of sight exits the atmosphere, the observer is looking into space where the initial radiance is the cosmic

background radiation, which can be modelled by a black body with a temperature of 2.725 K. However, the magnitude of the Planck function at this temperature in the TIR spectral region, when compared with the magnitude of radiance emitted from the atmosphere and surface of the Earth, is small enough that the initial radiance can be said to be essentially zero. In the second case where the line of sight ends at the ground, the initial radiance is determined by the surface emission. Using a black body model the surface emission is $\epsilon B(T_{\text{surf}})$ where ϵ is the emissivity of the ground and T_{surf} is the surface temperature. Therefore, the initial radiance becomes

$$I_0 = \begin{cases} B(T_{\text{cosmic}}) \approx 0, & \text{looking towards space} \\ \epsilon B(T_{\text{surf}}), & \text{looking towards surface} \end{cases}. \qquad (3.7)$$

The following sections describe the detailed steps in the TIR algorithm. First, the model atmosphere is set up by specifying parameters such as pressure, temperature, and number densities of gas species. In the second step absorption cross sections are computed and stored in a table as a function of wavelength, altitude, and, optionally, horizontal position. The third step splits the line of sight into segments where the atmosphere is assumed to be homogeneous, in a process known as ray tracing. The final step is to use Equation (3.6) iteratively to compute the modelled radiance.

Model Atmosphere Configuration

The user configures the TIR engine by inputting the lines of sight and wavelengths. Additionally, a number of optional settings can be customized which affect the speed and accuracy of the computation. Optional parameters include the spacing between the spherical shells which divide the atmosphere into homogeneous layers, enabling refractive ray tracing, and enabling two-dimensional variation in atmospheric parameters. By default, atmospheric parameters used by the model vary only with height. These parameters include species populations, temperature, pressure, and the absorption cross sections that result from these values. Enabling a two-dimensional atmosphere allows parameters to vary along the horizontal direction in addition to the vertical direction. In the TIR engine, the horizontal direction is interpreted as an angle measured between two vectors pointing from the origin of the model coordinate

system to two different points along the line of sight. The first vector is to a reference point from which all angles are measure while the second vector is to the current position along the line of sight where the atmosphere is being described. Since scattered radiance can be neglected, all radiance sources occur along the line of sight. Therefore, two dimensions are able to completely describe any vertical and horizontal variations in the atmosphere that have an effect on the observed radiance.

Important parameters are stored in an *atmospheric table* which contains the values of each parameter at discrete heights and, if specified, horizontal locations. The locations are set using a customizable spacing, with a default spacing of 500 m. In addition to storing species number densities, the table is used to hold precomputed values of absorption and the Planck function source term. When the value of a parameter is needed by the model, it is determined by interpolation between the nearest values defined in the atmospheric table. As a result, decreasing the spacing of the table reduces the interpolation error but requires increased computation time.

Absorption Calculation

After the dimensionality and contents of the atmosphere have been specified, absorption cross sections can be computed. As in the HR engine, the HITRAN database provides the parameters for computing line intensities. Recall from Section 2.3 that the the absorption cross section, σ_a, of a species in a spectral window is the sum of the spectral line intensity of each transition line within the window, $S_{lu,i}$, multiplied by the Voigt broadening function, ϕ_V,

$$\sigma_a(\nu) = \sum_i S_{lu,i}(T)\phi_V(\Delta\nu, T, p). \tag{3.8}$$

The line intensity is dependent on temperature, T. Additionally, the Voigt broadening is affected by temperature, pressure, p, and the difference, $\Delta\nu$, between the target wavenumber, ν, and the wavenumber corresponding to the energy required by the ith transition. The temperature and pressure can be extracted at any point in the specified atmosphere, allowing the cross sections to be stored in the atmospheric table. However, the quantity that is finally saved in the table is the absorption, k_a, computed by multiplying the cross sections of all

absorbing species by their number densities,

$$k_a = \sum_i \sigma_{a,i} n_{a,i}.$$ (3.9)

This absorption is computed for each point specified in the atmospheric table and at every wavelength required by the radiance calculation.

Ray Tracing

During model configuration, the user provides a list of lines of sight. Each line of sight contains the current position of the observer, a unit vector describing the look direction, and a time. The ray tracing step takes a line of sight and splits it into segments, which are referred to as *cells*. This splitting is achieved by calculating the intersection of the line of the sight with geometric objects that separate the model atmosphere into homogeneous portions. The most commonly used geometric objects are concentric, spherical shells, as discussed in Section 2.6.3. Recent improvements to SASKTRAN added geometric shapes such as cones and planes to the ray tracing algorithm (Zawada et al., 2015). When a limb-viewing LOS is desired, the new shapes allow for increased segmentation of the line of sight near the tangent point, where spherical shells would result in longer path segments in this region. Reducing the length of segments alleviates the inaccuracies introduced by assuming a homogeneous atmospheric composition across a segment.

There are two main cases to consider in the ray tracing algorithm: one where refraction is ignored and one where it is not. When refraction is ignored, the ray tracing procedure is greatly simplified because the propagation path is a straight line. The intersection points of a straight line with a geometric object are easy determine and can be calculated using known analytic equations. If refraction is considered, the line of sight will be curved due to changes in the index of refraction with altitude. The refractive index of air is greater at lower altitudes due to the increased air density.

Radiance Calculation

With the the atmospheric table specified and the line of sight split into cells, radiance can be propagated from the endpoint of the line of sight to the observer using Equation (3.6). In

a given cell, labelled with index j, the radiance, I_j, is the outgoing radiance computed for cell $j-1$. The source term, B_j, of the cell is the average value of the Planck function at the start and end points of the cell. Similarly, the extinction, k_j, is calculated as the average of the start and end values and is used to calculate the optical depth across the cell, τ_j,

$$\tau_j = k_j \Delta s_j, \tag{3.10}$$

where Δs is the path length of the cell.

3.2.2 Verification

The first test of the accuracy of SASKTRAN-TIR is to replicate the comparison with ARTS that was performed in Figure 3.1. The model atmosphere is identical to the previous comparison, with ozone being the only species present. Figure 3.6 shows the results of the TIR simulation, which produces a similar agreement of around 0.1%. While the HR engine achieved similar results, the main improvement provided by the TIR engine is a reduction in computation time. The radiance was calculated in approximately 16 seconds when using the TIR engine while the same calculation required several minutes with the HR engine.

The first test demonstrated accurate results for a nadir line of sight which produced an absorption spectrum. However, it is important to verify the accuracy of the TIR engine with lines of sight looking through the atmospheric limb as will be done with the LIFE instrument. Figure 3.7 shows the result of a limb radiance simulation, with an identical atmospheric setup to the previous nadir simulation. The observer is positioned at an altitude of 40 km with a line of sight that looks through the atmospheric limb to a tangent altitude of 20 km. A zoomed in portion of the plot shows that the radiance is now an emission spectrum as opposed to the absorption spectrum shown in the nadir simulation. In the nadir simulation, the observer was looking at the warm ground which results in a large initial radiance from the end of the line of sight. As the surface emission moves upwards towards the observer, radiation is absorbed by greenhouse gases. The opposite phenomenon is observed in the limb simulation, in which the radiance at the end of the line of sight is negligible and radiance is increased by thermal emissions from gas species along the line of sight. Both absorption and emission processes are present in all simulations, but depending on the observer geometry

one process will generally be more apparent in the spectrum.

The percent difference between the TIR engine and ARTS is greater in this scenario, reaching differences as great as 4%. A number of factors contribute to this increased difference. In the emission spectrum, the radiance approaches zero at some wavelengths, resulting in larger percentage differences. From the direct radiance differences plotted in Figure 3.8 it can be seen that differences in the limb simulation are of similar magnitude to the nadir case. Additional errors in the comparison can be a result of differences in ray tracing algorithms and interpolation methods used by each model. These variations become amplified in the limb measurement simulation as the path lengths of the segments in which the atmosphere is assumed to be homogeneous become larger.
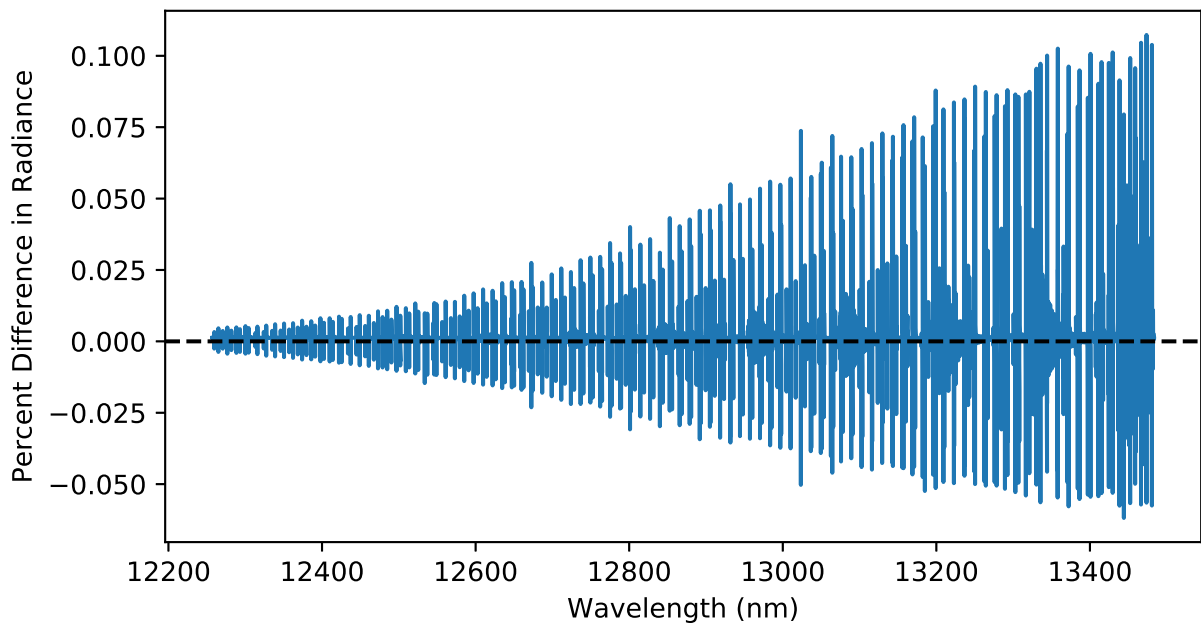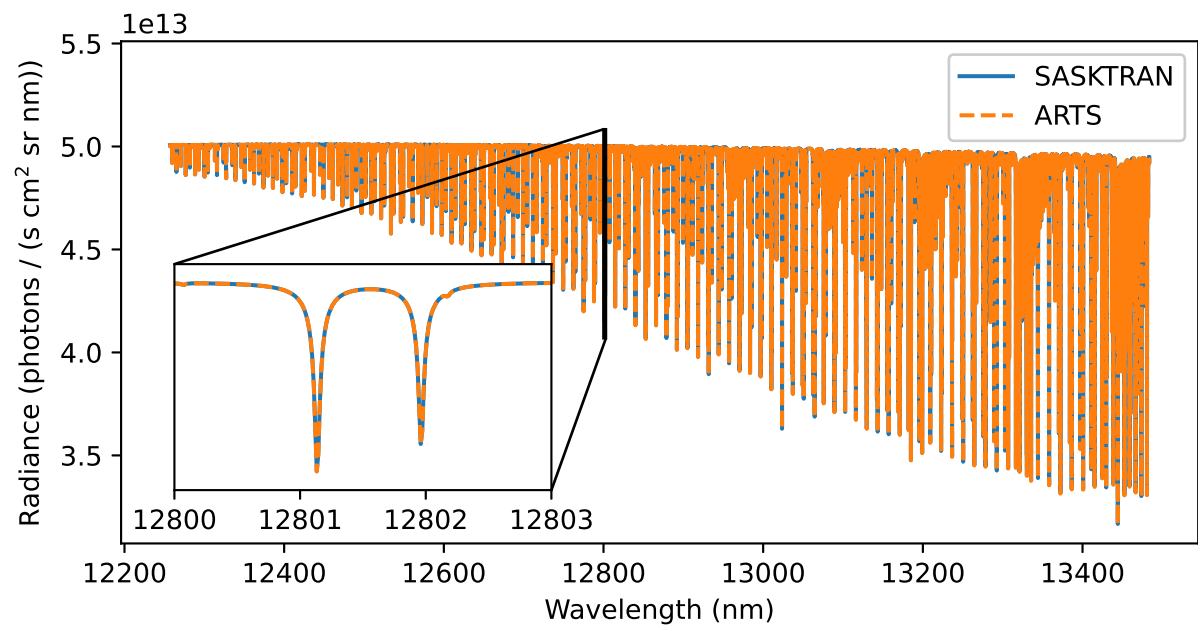
Figure 3.6: Comparison between SASKTRAN-TIR and ARTS for a nadir line of sight. Top: simulated radiances with an inset zoomed in on the 12800 to 12803 nm portion of the spectra. Bottom: percent difference of SASKTRAN-HR radiance from ARTS radiance.
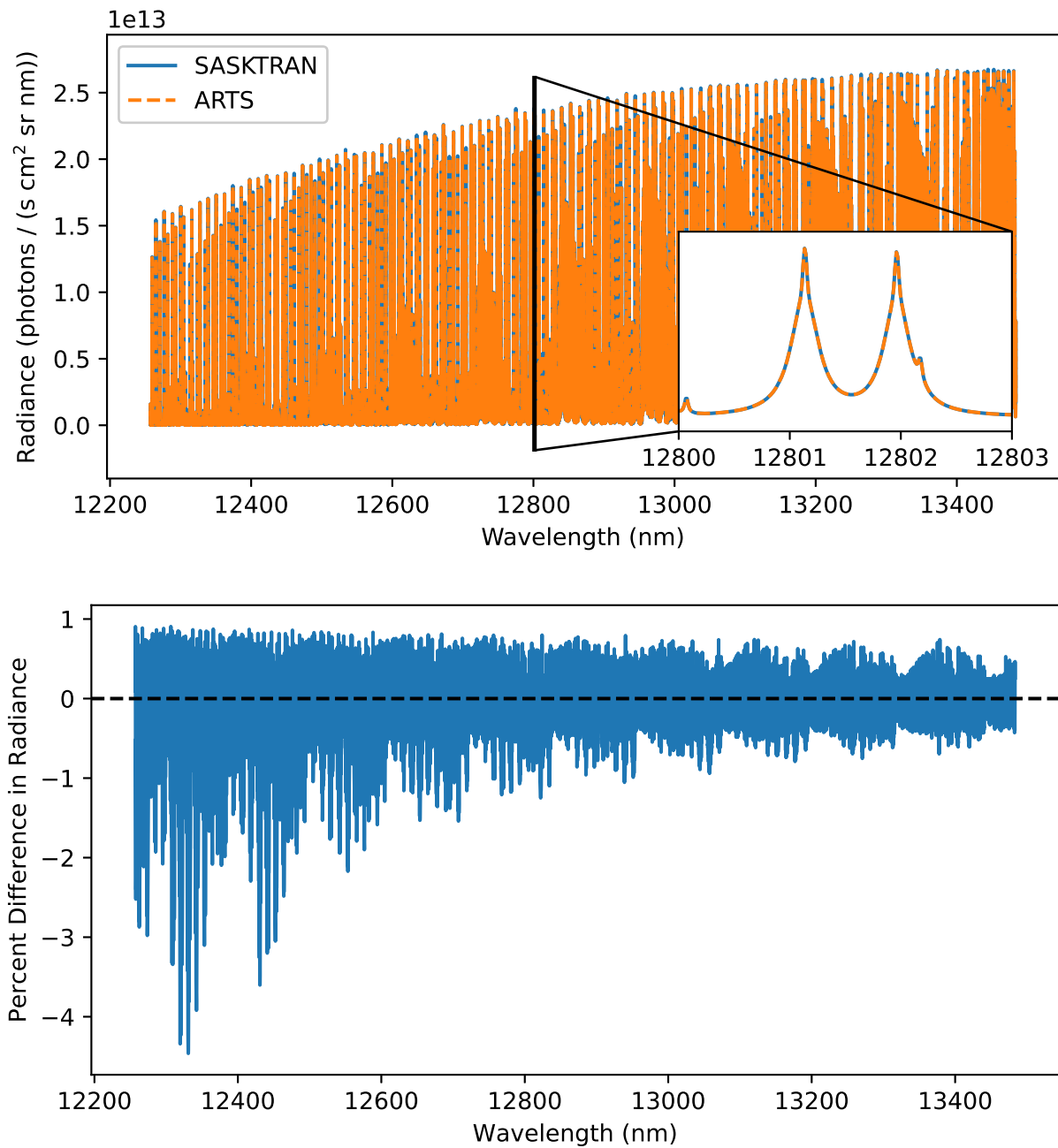
Figure 3.7: Comparison between SASKTRAN-TIR and ARTS for a limb line of sight. Top: simulated radiances with an inset zoomed in on the 12800 to 12803 nm portion of the spectra. Bottom: percent difference of SASKTRAN-HR radiance from ARTS radiance.
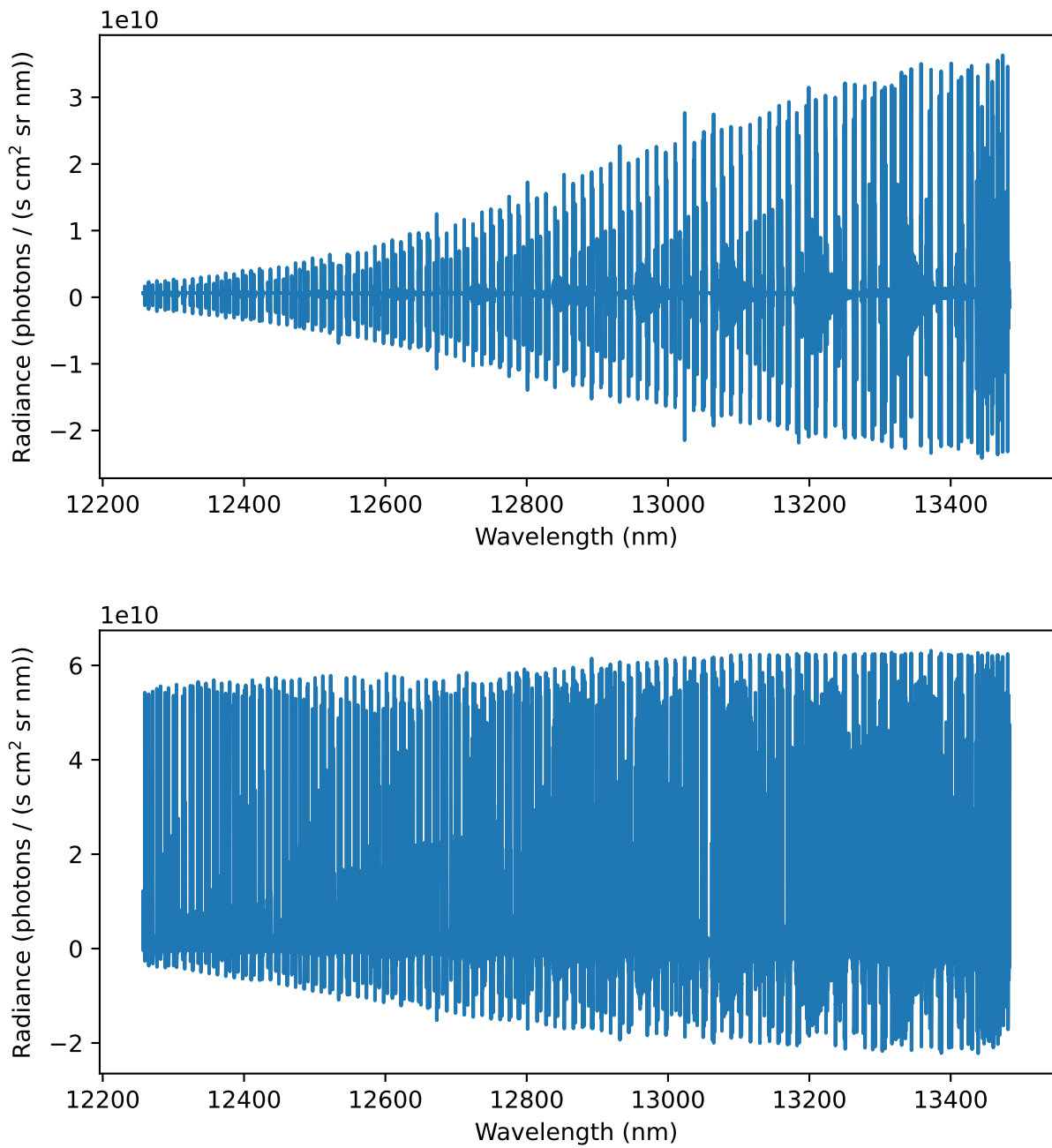
Figure 3.8: Difference between SASKTRAN-TIR and ARTS radiances for a nadir (top) and limb (bottom) line of sight.

4 SASKTRAN-TIR Jacobians

An important step in the retrieval process is to calculate the effect of changing an atmospheric state parameter, such as the number density of a species or the temperature, on the model output. The effect is characterized by computing the derivative of the modeled radiance with respect to these parameters. These derivatives are called *weighting functions* or *Jacobians*.

The simplest method of computing weighting functions is to perturb the desired parameter and run the model a second time, computing the derivative numerically from the difference in output radiance divided by the perturbation of the parameter. Calculating Jacobians using perturbation techniques is discussed in Section 2.5.6. Due to requiring multiple iterations of the model, this method is slow and computation time can be improved significantly by introducing analytical weighting functions into the engine. The analytical expressions reduce the weighting functions to equations where derivatives are taken of internal parameters, such as the optical depth, at integration points along the line of sight. Therefore, analytical weighting functions can be computed alongside the main radiative transfer integral, removing the need for successive model runs.

The SASKTRAN-TIR engine was described in Chapter 3. This engine was created to provide an engine optimized for clear sky TIR calculations by ignoring the effects of scattering, while also enabling the calculation of analytic Jacobians for retrieving atmospheric quantities. The second focus of this thesis is implementation of analytic Jacobians described in this chapter, which will be used to determine information about atmospheric constituents using remote sensing measurements performed by LIFE.

4.1 Implementation of Analytical Weighting Functions

The implementation of analytic weighting functions in SASKTRAN-TIR is a similar approach to ARTS and the Karlsruhe Optimized and Precise Radiative transfer Algorithm (KOPRA) (Eriksson et al., 2005; Hoepfner et al., 1998). A weighting function is defined as the change in the modelled radiance, I, with respect to an atmospheric parameter, x,

$$\frac{\partial I}{\partial x} = \sum_{j=1}^{N} \frac{\partial I}{\partial x_j} \frac{\partial x_j}{\partial x}. \tag{4.1}$$

The term $\partial x_j / \partial x$ describes the relative weighting of the perturbation at point j. The partial derivative of radiance with respect to the perturbation at this point can be expanded using the chain rule,

$$\frac{\partial I}{\partial x_j} = \frac{\partial I}{\partial \tau_j} \frac{\partial \tau_j}{\partial x_j} + \frac{\partial I}{\partial B_j} \frac{\partial B_j}{\partial x_j}. \tag{4.2}$$

The derivatives of I can now be determined from Equation (3.6), resulting in

$$\frac{\partial I}{\partial \tau_j} = (B_j - I_j)e^{-\tau_j} \prod_{i=j+1}^{N} e^{-\tau_i}, \tag{4.3}$$

and

$$\frac{\partial I}{\partial B_j} = (1 - e^{-\tau_j}) \prod_{i=j+1}^{N} e^{-\tau_i}. \tag{4.4}$$

The product at the end of Equations (4.3) and (4.4) is the result of attenuating from the current point to the observer. The remaining partial derivatives on the right hand side of Equation (4.2) are computed differently depending on what type of parameter x is. If x refers to the number density of an absorbing species, denoted n_x, the second term in Equation (4.2) becomes zero because the Planck function does not depend on gas concentrations. The derivative of optical depth can be expanded once again using the chain rule to get

$$\frac{\partial \tau_j}{\partial n_{x,j}} = \frac{\partial \tau_j}{\partial k_{a,j}} \frac{\partial k_{a,j}}{\partial n_{x,j}}. \tag{4.5}$$

Substituting the expressions for the optical depth and absorption in a single segment from Section 3.2.1 results in

$$\frac{\partial \tau_j}{\partial n_{x,j}} = \frac{\partial}{\partial k_j} (k_j \Delta s_j) \frac{\partial}{\partial n_{x,j}} \left(\sigma_{x,j} n_{x,j} + \overbrace{\sum_y \sigma_{y,j} n_{y,j}}^{\text{other species}} \right),$$
$$= \Delta s_j \sigma_{x,j}. \tag{4.6}$$

In the above expression the subscript a, signifying absorption, has been omitted to simplify the notation. The absorption contribution from the target species, x, is moved outside the summation to show that the final derivative depends only on the cross section of the target species.

The final expression for calculating the weighting function with respect to a species number density becomes

$$\frac{\partial I}{\partial n_x} = \sum_{j=1}^{N} e^{-\tau_j} \sigma_{x,j} \Delta s_j (B_j - I_j) \frac{\partial n_{x,j}}{\partial n_x} \prod_{i=j+1}^{N} e^{-\tau_i}. \tag{4.7}$$

Therefore, storing the values in Equation (4.7) with subscript j while computing the radiative transfer integral allows the weighting function to be calculated with minimal additional computation, with no need to run the model multiple times. Each of the terms, including the exponential therms, are already calculated as part of the iterative radiance calculation in Equation (3.6).

Often it is desirable to compute derivatives of radiance with respect to the volume mixing ratio (VMR), r_x, of a species, instead of its number density. Assuming an ideal gas, the volume mixing ratio is equal to the mole ratio of the species, which is the ratio of the number density of species x to the number density of all neutral air particles, n_{air},

$$r_x = \frac{n_x}{n_{\mathrm{air}}}. \tag{4.8}$$

To compute VMR weighting functions, the only change needed in the calculation is to replace the species density in Equation (4.6) with the product of the VMR and neutral air density, resulting in an optical depth derivative of

$$\frac{\partial \tau_j}{\partial r_{x,j}} = \Delta s_j \sigma_{x,j} n_{\mathrm{air},j}. \tag{4.9}$$

With the ideal gas assumption, the neutral air density can be determined from the atmospheric temperature, T, and pressure, p, by

$$n_{\mathrm{air}} = \frac{p}{k_B T}, \tag{4.10}$$

where k_B is the Boltzmann constant.

4.1.1 Temperature Weighting Functions

The atmospheric temperatures used in the model greatly impact the calculations of absorption cross sections and thermal emission sources. Temperature profiles may be input to the model using data from previous experimental results and climatologies. If accurate knowledge of the temperature profile is not available, it may be necessary to retrieve temperature from the measurement itself. The analytic expressions for computing temperature weighting functions are more complicated than gas densities because the source term and absorption cross section both have a temperature dependence.

Starting from Equation (4.2), the target, x, is now the temperature, T. The partial derivatives of I given by Equations (4.3) and (4.4) remain the same. The optical depth derivative can once again be expanded to

$$\frac{\partial \tau_j}{\partial T_j} = \frac{\partial \tau_j}{\partial k_{a,j}} \frac{\partial k_{a,j}}{\partial T_j}. \tag{4.11}$$

The first term in the expansion is unchanged from before, where

$$\frac{\partial \tau_j}{\partial k_{a,j}} = \Delta s_j, \tag{4.12}$$

while the second term is computed numerically. Calculating $\partial k_{a,j}/\partial T_j$ analytically is difficult due to the temperature dependence of the absorption cross section. As shown in Equation (2.82), both the spectral line intensities and line shape functions in the cross section calculation have a temperature dependence that would need to be calculated for every spectral line in the summation. Since analytic expressions would need to be implemented on a per-line basis, there would not be a significant improvement in computational efficiency.

The final part of the temperature Jacobian is the derivative of the source function with respect to temperature, which is simple to calculate analytically:

$$\frac{\partial B_j}{\partial T_j} = \frac{2hc^2}{\lambda^5 k T_j^2} \frac{e^{hc/\lambda k T_j}}{\left(e^{hc/\lambda k T_j} - 1\right)^2}. \tag{4.13}$$

4.2 Validation of Analytic Weighting Functions

The implementation of analytic weighting functions in the TIR engine is verified by comparison to a traditional perturbation method. Perturbed Jacobians are calculated using finite

differences. The model is run with an initial value of the target parameter, x, resulting in a calculated radiance, $I(x)$. Next, the parameter is perturbed by an amount, Δx, and the radiance is computed a second time. The value of the weighting function is then

$$\frac{\partial I}{\partial x} \approx \frac{I(x + \Delta x) - I(x)}{\Delta x}. \tag{4.14}$$

Figure 4.1 compares the analytic implementation with the perturbation method of Equation (4.14) for a single wavelength and line of sight. The profile indicates how the observed radiance would change if the amount of ozone was increased at a given altitude. Adding more ozone at higher altitudes causes an increase of thermal emissions, making the radiance larger. At some lower altitudes the increase in absorption from the added ozone is greater than the increased emissions, resulting in a decrease to the observed radiance.

To demonstrate the importance of analytic Jacobians, consider the result shown in Figure 4.1. There are 80 total Jacobian values shown, each spaced 500 m apart vertically. The perturbation method requires 80 additional simulations because the ozone profile can only be modified at one altitude for each run of the model, while all of the analytic Jacobians are computed in a single run of the model.

The figure shows that the analytic Jacobians are in good agreement with the numerical method. These numerical Jacobians, although much slower to compute, are known to be correct because the accuracy of the SASKTRAN-TIR radiance computation has been verified in Section 3.2.2. Therefore, Figure 4.1 demonstrates the correctness of the implemented analytic Jacobians for the given wavelength and line of sight. Small differences can be seen near the 12.5 km tangent altitude. The analytic Jacobian is smaller than the numerical result at 12.5 km and larger at 13 km.

To further explore the accuracy of the TIR weighting functions it is necessary to test a variety of wavelengths and lines of sight. Consider the carbon dioxide emission spectra shown in Figure 4.2, modelled using the TIR engine at a high wavelength resolution of 2.5×10^{-5} nm. From this plot three wavelengths are chosen to test the weighting function implementation, as indicated by the dashed vertical lines. The wavelengths are chosen to cover the range of radiance magnitudes, from the peak at the center of the spectral line to the minimum value near the edge of the plot.
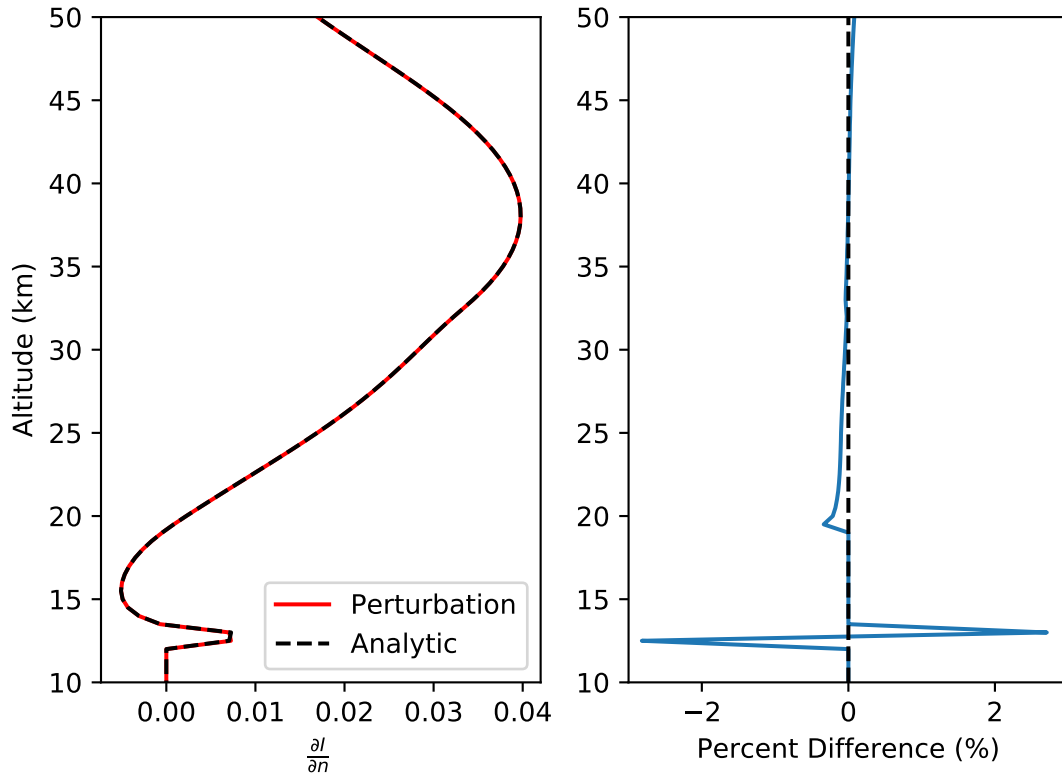
Figure 4.1: Comparison between analytic and perturbation calculation of an ozone weighting function with a wavelength of 10 μm and tangent altitude of 12.5 km.
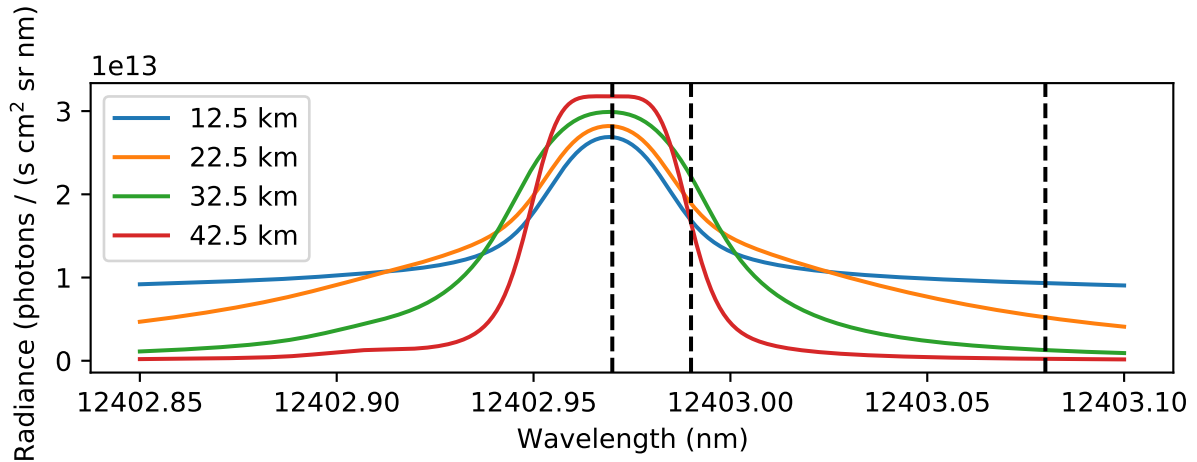
Figure 4.2: Simulated radiance of a CO_2 spectral line for tangent altitudes of 12.5, 22.5, 32.5, and 42.5 km. The dashed vertical lines indicate the selected wavelengths (12402.97, 12402.99, and 12403.08 nm) for the weighting functions shown in Figure 4.3.

72

The weighting functions that result from this selection of wavelengths and tangent altitudes are shown in Figure 4.3. Each row displays the results at different tangent altitude and each column represents a different wavelength. As in the ozone weighting function test, the left plot in each case compares the results from the analytic and perturbation methods while the right plot indicates the percent difference. The percent different is computed as $(w_a - w_p)/w_p \times 100\%$ where w_a are the analytic weighting functions and w_p are the perturbation weighting functions. In general, the two methods agree within one to two percent at most altitudes with larger differences occurring near the tangent altitudes. The difference is most noticeable at 12402.97 nm, near the center of the spectral line, especially towards higher tangent altitudes. When discussing the impact of these differences, it is important to consider the role of the Jacobians in the retrieval algorithm. The Jacobians inform the algorithm about the amount a parameter should be increased or decreased to produce a simulated radiance that more accurately reproduces an instrument measurement. If the Jacobian is not exactly correct, it may take more iterations of the radiative transfer model to achieve the desired result. However, the computation time of a retrieval process using analytic weighting functions will still be significantly faster than the perturbation method.
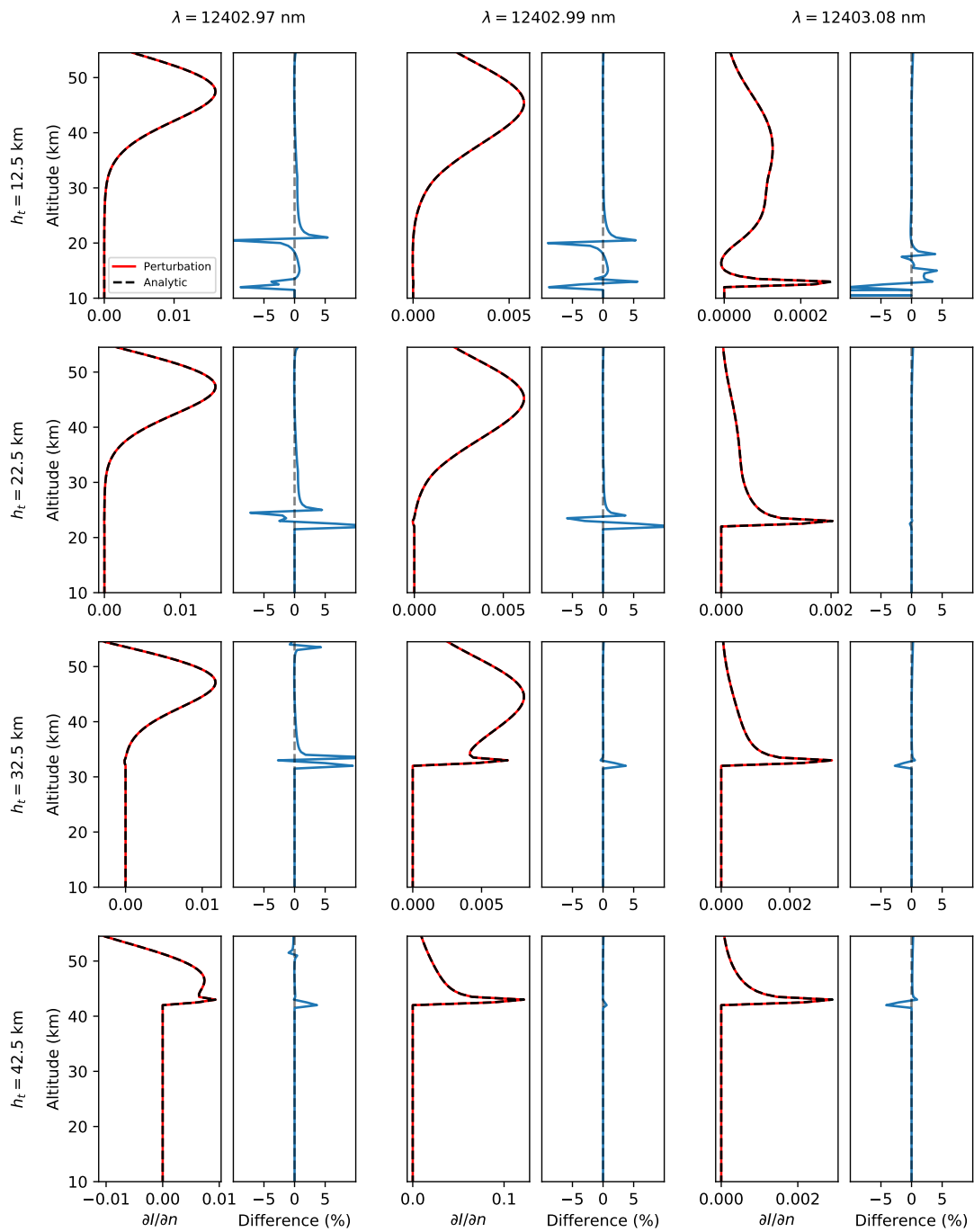
Figure 4.3: Weighting functions of CO_2 number density, $\partial I/\partial n$, for select wavelengths, λ, and tangent heights, h_t.

4.3 Improving Performance in Successive Iterations

The most time-consuming step in the TIR model is the calculation of absorption cross sections. Even small spectral windows contain thousands of spectral lines in which the voigt broadening must be computed for each set of pressure and temperature values in the atmospheric table. When retrieving profiles of atmospheric species it is necessary to iteratively run the model while using weighting functions to determine how to update the target parameter between each model iteration. Often the only parameter changed is the concentration of the target species. The viewing geometry, pressure, and temperature remain constant. In these scenarios the computation time can be significantly reduced in subsequent model iterations by storing certain variables in program memory. At each point in the atmospheric table, the TIR engine saves the total absorption, k, which results from all species, as well as the absorption cross sections, σ_x, of any species x for which weighting functions are calculated. If the only parameter changed is the number density of the target species, n_x, the absorption in subsequent model iterations can updated using

$$k = k_{\text{prev}} + \sum_x^{\text{target species}} \sigma_x \Delta n_x, \tag{4.15}$$

where Δn_x is the change in each target species number density from the previous iteration. This time saving step is only possible when the absorption cross sections remain constant. They must be recomputed if there are any changes to the temperature and pressure profiles.

As an example, consider the modelled radiance shown in Figure 3.7 which is calculated at 100,000 wavelengths. When the TIR engine is configured to compute ozone weighting functions at 100 altitudes between 0 and 100 km for each wavelength, the computation time is approximately 22 seconds. This calculation was performed on a system with a quad-core Intel i7-6700 processor, running in parallel on 8 threads. Without using the absorption cross section caching method described by (4.15), changing the ozone number density and running the model a second time will take an additional 22 seconds. When the caching method is used, the second calculation is performed in approximately 7 seconds, providing a significant performance improvement.

4.4 Summary

This chapter detailed the implementation of analytic Jacobian expressions into the newly created SASKTRAN-TIR engine. Expressions for computing the partial derivatives of modelled radiance with respect to greenhouse gas number densities and volume mixing ratios, as well as atmospheric temperatures were developed for SASKTRAN-TIR. The correctness of the implementation was verified by comparing the computation of analytic Jacobians of greenhouse gas number densities, specifically ozone and carbon dioxide, to Jacobians computed by numerical perturbation. While significantly slower to compute, the Jacobians computed by perturbation methods are known to be correct because the accuracy of the TIR was verified in Chapter 3 by comparison with an existing radiative transfer model, ARTS.

5 LIFE Simulations

Chapters 3 and 4 described the development and verification of the TIR engine, a model designed for retrieving profiles of atmospheric constituents from limb-based infrared measurements. In this chapter, the capabilities of the TIR engine are explored by returning to the motivation for its creation, the Limb Imaging FTS Experiment (LIFE). The goal is to demonstrate that, given a measurement, the TIR engine can successfully operate the forward model in a retrieval algorithm that produces vertical profiles of greenhouse gas populations. In the place of real measurements, a simulated measurement is created using SASKTRAN-TIR, where the model input represents the true atmosphere. One parameter, such as ozone number density, is selected as the retrieval target where the initial value is a guess that is different than the true value. Through an application of the inverse theory described in Section 2.5, the radiance and Jacobians are used to adjust the target parameter iteratively, until it converges to the profile used to generate the simulated measurement.

Section 5.1 describes the forward model of the LIFE instrument, in which radiances computed with high spectral resolution using SASKTRAN-TIR are transformed according to the physical operation and parameters of the Fourier transform spectrometer (FTS) used by LIFE. Results from the retrieval simulations using this forward model are discussed in section 5.2. The software suite developed in this chapter will be used by the LIFE team to analyze real data from the LIFE balloon campaign in Timmins and from future campaigns with new iterations of the instrument.

5.1 Measurement Simulations

LIFE performs measurements using a Fourier Transform Spectrometer (FTS). The FTS contains a Michelson interferometer which splits the incoming light along two paths and measures the resulting interference pattern on an infra-red sensitive photodetector. As described in

Section 2.4.1, interference patterns of light which can be transformed into spectral radiances by a Fourier transform.

5.1.1   Instrument Model

This section details the process of transforming the raw radiance simulated by SASKTRAN-TIR into the same form as a radiance measurement from the LIFE instrument. LIFE contains an array of 16 photodetectors, with optics designed such that each pixel measures the radiance at a different tangent altitude when the instrument is pointed through the atmospheric limb.

A radiance spectrum is obtained by taking the Fourier transform of the measured interferogram, as detailed in Section 2.4.1. The interferogram, $I(x)$, is a function of the path difference, x. Taking the Fourier transform of $I(x)$ produces the spectral radiance, $I(\nu)$, as a function of wavenumber, ν,

$$I(\nu) = \mathcal{F}[I(x)] = \int_{-\infty}^{\infty} I(x)e^{-i2\pi\nu x}\mathrm{d}x. \tag{5.1}$$

Taking the real part of this expression returns the cosine transform given by Equation (2.89) for a Michelson interferometer. The complex form is used here to account for both positive and negative optical path differences. Equation (5.1) represents the radiance if it were possible to measure an ideal interferogram for all path differences between negative and positive infinity. In reality, the measurement is constrained by the maximum path difference (MPD), L, of the interferometer. This is equivalent to multiplying the interferogram by a rectangular function which is equal to 1 in the interval $[-L, L]$ and is 0 otherwise. The precise definition of the rectangular function is

$$\Pi(t) = \begin{cases} 0, & |t| > \frac{1}{2} \\ \frac{1}{2}, & |t| = \frac{1}{2} \\ 1, & |t| < \frac{1}{2} \end{cases}. \tag{5.2}$$

Multiplying the infinite interferogram by the rectangular function produces the measured interferogram,

$$I_{\mathrm{LIFE}}(x) = I(x) \times \Pi\left(\frac{x}{2L}\right). \tag{5.3}$$

When the Fourier transform is performed to determine the spectral radiance, the rectangular function becomes a normalized sinc function, and the multiplication between two functions

of x becomes a convolution between two functions of ν, resulting in

$$I_{\mathrm{LIFE}}(\nu) = \mathcal{F}[I_{\mathrm{LIFE}}(x)] = I(\nu) * 2L \operatorname{sinc}(2L\nu). \qquad (5.4)$$

Note that $I(\nu)$ represents the spectrum that would be observed by an ideal FTS capable of path differences extending to negative and positive infinity. This is equivalent to the spectrum returned by a radiative transfer model with infinite spectral resolution. Therefore, Equation (5.4) can be used to produce simulated LIFE spectra from radiances modelled by SASKTRAN-TIR. The sinc function is called the instrument line shape (ILS) and encapsulates the effects of the instrument and measurement technique on the true radiance. Convolving the radiance with the sinc ILS indicates the measured spectral lines will be broadened as a result of the path difference limitation, resulting in a finite spectral resolution that the instrument can resolve.

Other Instrument Effects

A number of additional factors effect the radiance measured by LIFE. Factors such as apodization, sampling method, and aperture size should be accounted for by the model (Runge, 2018). Of these effects, apodization is of particular importance and is accounted for in the simulations presented in this chapter. Apodization refers to a post-processing technique performed on the measured interferograms designed to reduce ringing which results from discontinuities at the edges of the interferograms. The discontinuities arise at the MPD where the interferogram is cut off to zero. In the apodization technique, the interferogram is decreased to zero at the edges to reduce the ringing effect. The interferogram is multiplied by a windowing function to achieve this result. One example of a window suitable for apodization is the Hann window (Runge, 2018). An unfortunate side effect of this process is a broadening of the instrument line shape, resulting in a decrease in the spectral resolution of the measured spectra. The full effects of apodization are not implemented by the instrument model described in this chapter, but the broadening of the ILS is accounted for by modifying the MPD. The MPD, L, is replaced with an effective MPD which is the true MPD divided by an apodization factor, f_{apo},

$$L_{\mathrm{eff}} = \frac{L}{f_{\mathrm{apo}}}. \qquad (5.5)$$

Radiance Units

SASKTRAN-TIR returns spectra as a function of wavelength in nm, with radiance units of photon/(s cm^2 nm sr). In the thermal infrared regime spectra are typically discussed as a function of wavenumber in cm^{-1}. Additionally, the radiative power is often reported as Joules per seconds, or Watts, instead of photons per second. These changes result in radiance units of W/(cm^2 cm^{-1} sr), which is the form used throughout this chapter. Conversion from SASKTRAN-TIR units is performed by multiplying by the energy per photon, hc/λ, then transforming the spectral unit from wavelength to wavenumber. Recall that spectral radiance is a quantity that is described per spectral interval. Since wavelength and wavenumber are related by $\nu = 1/\lambda$, the equivalent wavenumber interval, $\mathrm{d}\nu$, for a wavelength interval, $\mathrm{d}\lambda$, is

$$|\mathrm{d}\nu| = \frac{\mathrm{d}\lambda}{\lambda^2}. \tag{5.6}$$

Therefore, the spectral conversion from wavelength to wavenumber is performed by multiplying the radiance by λ^2. Combining the energy and spectral conversions gives the following equation for converting from radiance units of [photon/(s m^2 m sr)] to [W/(m^2 m^{-1} sr)],

$$I(\nu) = I(\lambda)hc\lambda. \tag{5.7}$$

5.1.2 Simulation Parameters

The simulations in this chapter use values received from the LIFE hardware team at the University of Saskatchewan. The LIFE instrument has an MPD of 1.4 cm, but with an apodization factor of 1.6 the effective MPD is 0.875 cm, as per Equation (5.5). Figure 5.1 shows the resulting ILS, $2L_{\mathrm{eff}} \operatorname{sinc}(2L_{\mathrm{eff}}\nu)$, which provides an idea of the effect of the FTS measurement technique on the spectrum. The first zero-crossing occurs at $1/2L_{\mathrm{eff}}$, a value of 0.571 cm^{-1} which indicates the spectral resolution of LIFE. Resolving individual spectral lines in the thermal infrared regime often requires spectral sampling on the order of 10^{-3} cm^{-1} or smaller. Therefore, the spectral features displayed in LIFE radiance plots may contain be a combination of many spectral lines, potentially from different species, that become averaged together as a result of convolution with the ILS.
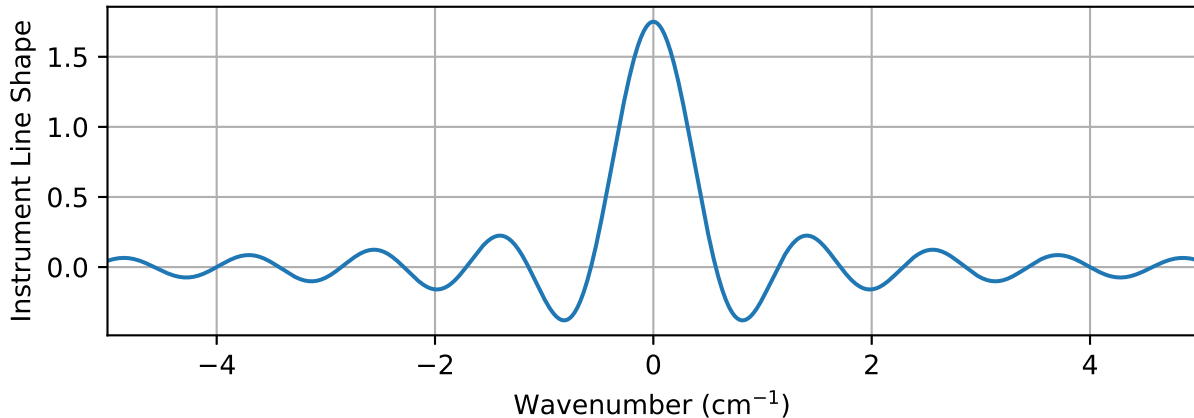
Figure 5.1: Instrument line shape implemented in the LIFE forward model.

The inputs required by SASKTRAN-TIR are a list of wavenumbers, lines of sight, and atmospheric composition. The wavenumber range is 700 to 1400 cm^{-1}, the range where the mercury cadmium telluride (MCT) detector implemented in LIFE is most responsive. Spectral spacing is set to 0.0005 cm^{-1}, small enough that individual spectral lines are modelled fully and to avoid missing narrow lines entirely. The same spectral resolution is used in the forward model for retrieving vertical profiles of greenhouse gases and temperatures from MIPAS infrared limb measurements (Höpfner et al., 2006). Sixteen lines of sight are created, one for each pixel in the detector array. Each line of sight originates from the same observer positioned at a typical balloon altitude of 40 km, but with each pixel measuring at a different tangent altitude. LIFE is designed with a 5.72° field of view (FOV). The pixels are spaced evenly across this FOV. In this measurement simulation, it is assumed that the look vector of the topmost pixel is horizontal, with the remaining look vectors spaced evenly to a maximum of 5.72° below the horizontal. This angular spacing results in the tangent altitudes displayed in Figure 5.2. Note that the spacing between each tangent altitude increases towards lower altitudes. Additionally, each pixel will capture a range of tangent altitudes over their vertical FOV, but for this simulation each pixel is assigned a single tangent altitude for simplicity.

81
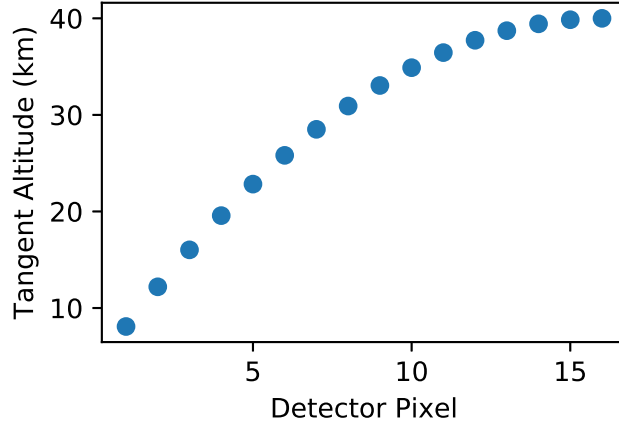
Figure 5.2: Tangent altitudes for each detector pixel in LIFE simulation. The imaged tangent altitudes will be spaced more tightly at higher altitudes.

5.1.3 Simulation Results

Figure 5.3 shows the results for a simulated LIFE measurement with a tangent altitude of 20 km, the 4th detector pixel in Figure 5.2. The simulated instrument radiance is plotted on top of the raw radiance modelled by SASKTRAN-TIR. A zoomed in portion of the spectrum, centered on a nitric acid emission line, shows how convolution with the instrument ILS results in a lower spectral resolution. Spectral lines become broadened and combine with each other, which must be considered in the process used to retrieve atmospheric species because lines from different species mix with each other.

In Figure 5.3, the simulated instrument radiance appears very smooth when looking at the magnified portion of the spectrum. The convolved radiance is still defined at the same points as the high resolution radiance. However, the real LIFE measurement is not as smooth because the number of data points is limited by the sampling rate as the path difference within the instrument is changed. The next step in the instrument model is to interpolate the radiance from the high resolution wavenumbers used in the model to the wavenumbers sampled by the instrument. Since the model spacing of 0.0005 cm^{-1} is significantly smaller than the instrument spacing of 0.35 cm^{-1}, a linear interpolation is sufficiently accurate. A portion of the radiance interpolated to the instrument samples is shown in Figure 5.4.

The final piece of the forward model is the inclusion of instrument noise. The overall
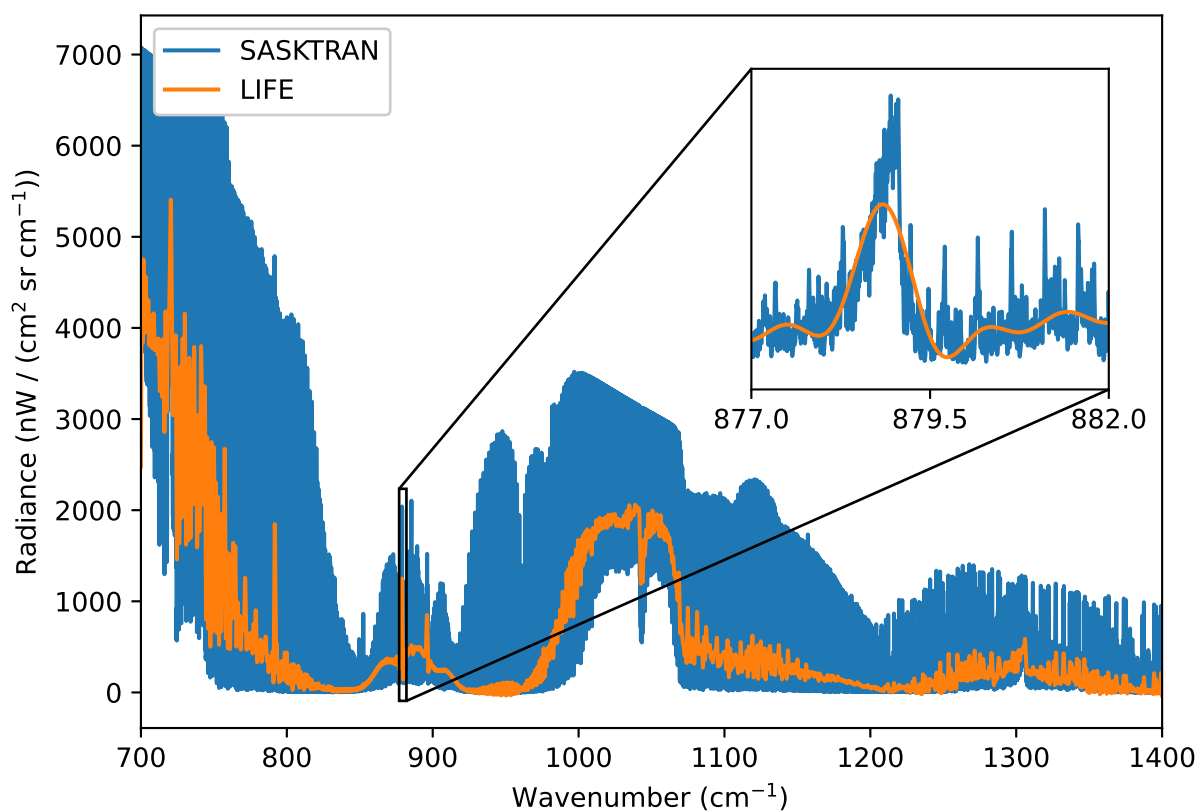
Figure 5.3: LIFE radiance simulation for a 20 km tangent altitude, with an inset zoomed in on the 877 to 882 cm^{-1} wavenumber range.
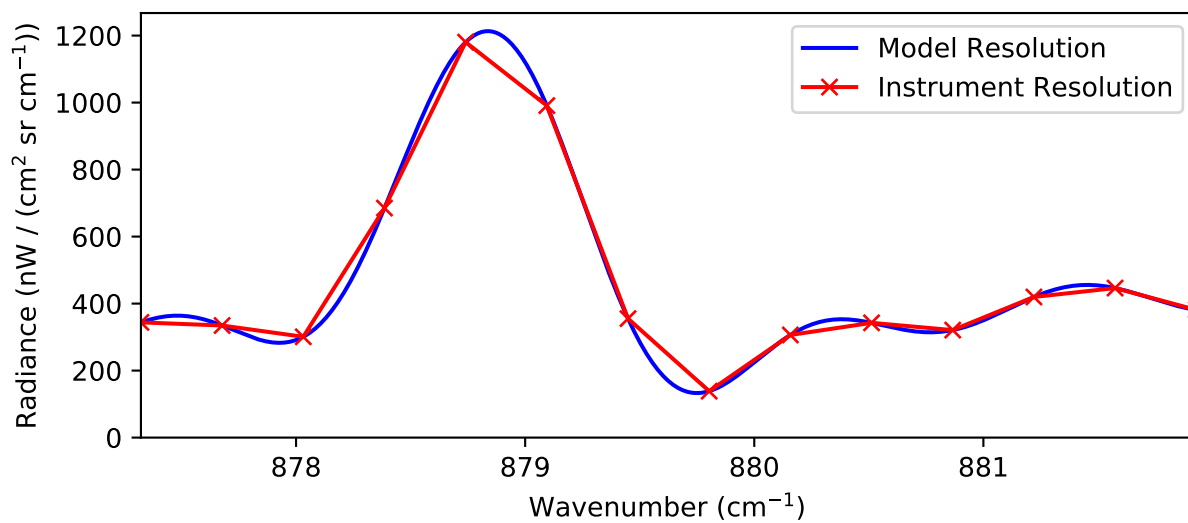
Figure 5.4: Interpolation from model resolution to instrument samples.

83

noise contribution is quantified by the noise equivalent spectral radiance (NESR), which describes the effect of noise in radiance units. NESR provides the noise floor for radiance measurements. Any signal below the NESR is undetectable due to the uncertainty introduced by noise. Figure 5.5 shows the simulated NESR for a pixel in the LIFE imager for the spectral range of the instrument. This NESR was modelled by Runge (2018) using a Monte-Carlo simulation. The addition of noise allows the measurement uncertainty be propagated through the retrieval algorithm in the error covariance, $\mathbf{S_y}$. The inclusion of measurement error is discussed in Section 2.5.3. As a result, the solution covariance, $\mathbf{S}$, describes the uncertainty in the retrieved parameter. In the retrieval of trace gas profiles, the square roots of each diagonal element of the solution covariance matrix are the standard deviation of the species concentration at each retrieval altitude.
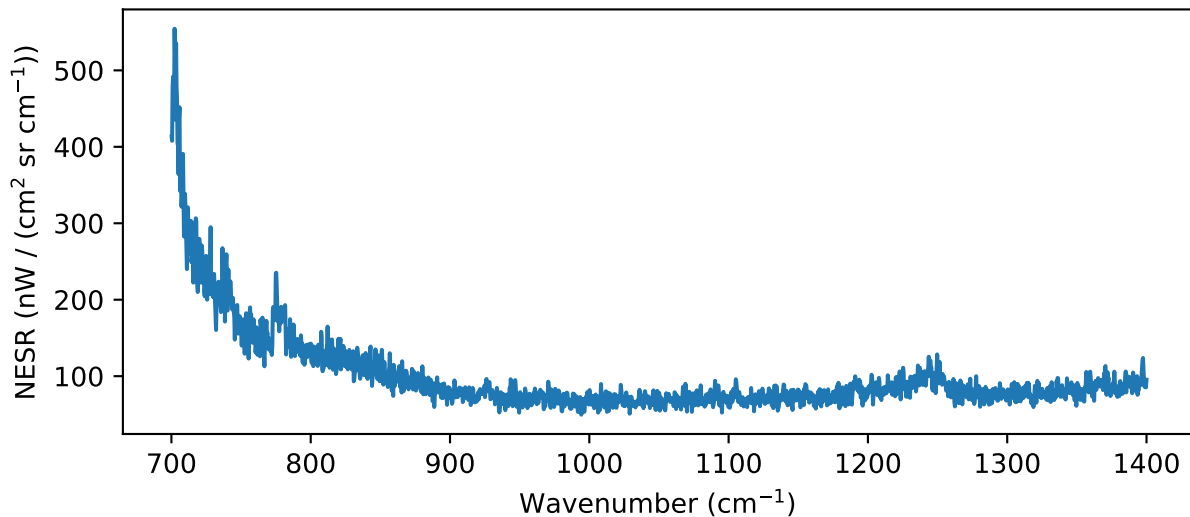
Figure 5.5: Noise equivalent spectral radiance modelled for LIFE (Runge, 2018).

5.2   Retrieval Simulations

In this section the forward model consisting of the SASKTRAN-TIR engine and LIFE instrument model is used to demonstrate the retrieval of trace gas profiles. The retrieval process begins with configuration of the TIR engine. Let the number density of the target species be n_x. The atmosphere is defined with profiles of temperature, T, pressure, p, and number

densities of any greenhouse gases that will effect the output. Number density profiles are distinguished between the target species, n_x, and all other species that have an effect on the radiance in the chosen microwindow, n_{other}. All of these parameters are input from a midlatitude summer climatology in the AFGL model atmosphere (Anderson et al., 1986). The wavenumber range is selected based on the retrieval species. Different species dominate the radiance at different spectral regions and it is desirable to select a spectral microwindow in which the target species has the greatest effect on the radiance. In the following tests, only the retrieval parameter is adjusted between model iterations. Therefore, the impact of other parameters on the retrieval should be minimized. Lines of sight are input for the sixteen tangent altitudes shown in Figure 5.2, with an observer positioned at a height of 40 km.

SASKTRAN-TIR uses these inputs to determine the radiance for the defined microwindow at a high spectral resolution, with a spacing of 0.0005 cm^{-1}. At the same time, the engine computes analytic weighting functions of the target species with the expressions developed in Chapter 4. For each line of sight and wavenumber, the weighting function is computed for a configurable range of retrieval altitudes. The retrieval altitudes are adjusted using the model interface, which provides access to additional settings such as the spacing between homogeneous atmospheric layers in the model. The radiance and weighting functions are passed to the LIFE instrument model. As described in Section 5.1, the instrument model applies the instrument line shape to the high resolution radiance. It is important to note that the weighting functions must also be passed through the instrument model, because they are derivatives of the radiance.

The modelled radiance and weighting functions are then passed to the retrieval algorithm, along with an instrument measurement. The goal of this retrieval process is to find the value of the target species which reproduces the measurement. In practice, the measurement is a real LIFE spectrum converted from a captured interferogram by Fourier transform. For this simulated retrieval the measurement is created with the same instrument model used in the retrieval. The simulated measurement uses a different value of n_x than the initial guess in the retrieval. A Gauss-Newton method, as detailed in Section 2.5.5, is utilized to determine how the target parameter should be updated to produce a simulated radiance more similar

to the measurement,

$$\vec{n}_{x,i+1} = \vec{n}_{x,i} + (\mathbf{K}_i^T \mathbf{S}_y^{-1} \mathbf{K}_i + \mathbf{S}_a^{-1})^{-1} [\mathbf{K}_i^T \mathbf{S}_y^{-1} [\vec{y} - \mathbf{F}(\vec{n}_{x,i})] - \mathbf{S}_a^{-1} (\vec{n}_{x,i} - \vec{n}_{x,a})]. \qquad (5.8)$$

The Gauss-Newton iteration is a result of minimizing χ^2, the output of the cost function,

$$\chi^2 = (\vec{y} - \mathbf{F}(\vec{n}_x))^T \mathbf{S}_y^{-1} (\vec{y} - \mathbf{F}(\vec{n}_x)) + (\vec{n}_x - \vec{n}_{x,a})^T \mathbf{S}_a^{-1} (\vec{n}_x - \vec{n}_{x,a}). \qquad (5.9)$$

The value of χ^2 decreases if the difference between the forward modelled radiance, $\mathbf{F}(\vec{x})$, and the measurement radiance, $\vec{y}$, becomes smaller. If convergence is achieved, the most recent value of $\vec{n}_x$ is returned as the retrieval result. If convergence is not achieved, the forward model is updated with the new $\vec{n}_x$ and another iteration is performed. This process that was created for testing SASKTRAN-TIR in a retrieval framework is summarized in Figure 5.6.

Instrument noise, characterized by the NESR, describes the uncertainty of the measurements, $\vec{y}$, and is contained within the measurement covariance, $\vec{S}_y$. For these simulations it is assumed that the errors from each pixel of the detector array are uncorrelated. Therefore, the only nonzero elements of $\vec{S}_y$ are the diagonal elements which contain the variance from each measurement. The NESR provides an estimate of the uncertainty for a single measurement, allowing a single measurement for a detector pixel, p, and wavenumber, ν, to be written as $y(p, \nu) \pm \mathrm{NESR}(p, \nu)$. However, retrievals are often performed using a measurement vector that is averaged from a large number of measurement samples. $\vec{y}$ is then constructed from the mean value of the measurements, with a standard deviation equal to the uncertainty of a single measurement divided by the square root of the number of measurements, N. The diagonal element of $\mathbf{S}_y$ corresponding to an element of the measurement vector, y_i, is then

$$S_{y,ii} = \left(\frac{\mathrm{NESR}(p_i, \nu_i)}{\sqrt{N}} \right)^2. \qquad (5.10)$$

5.2.1 Ozone Number Density Retrieval

These retrieval simulations demonstrate the ability to determine the ozone number density profile from LIFE measurements. A LIFE measurement is simulated using the instrument model with AFGL atmospheric profiles. Next, the forward model used in the retrieval is initialized with a nearly identical atmosphere, with the exception that a different ozone
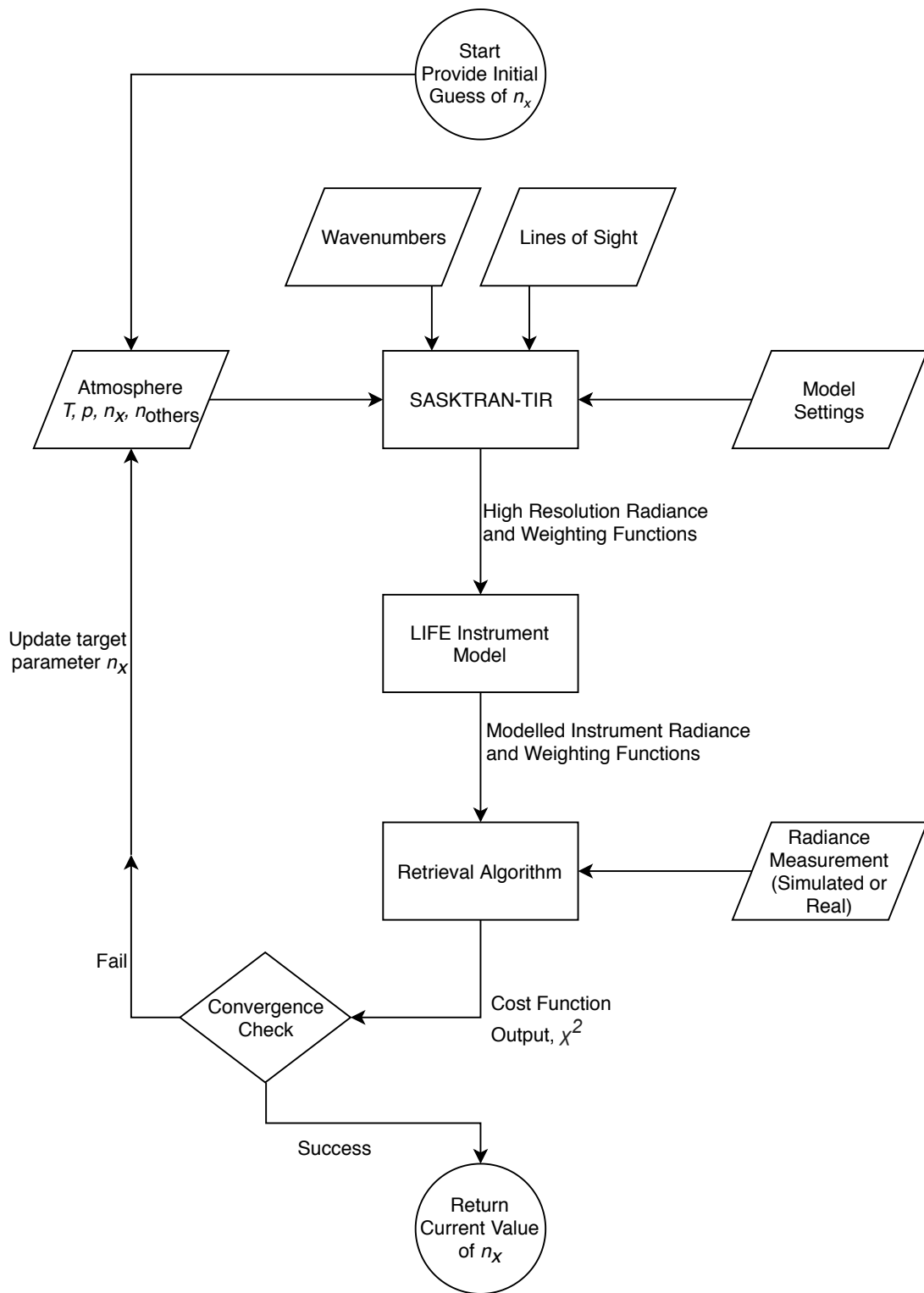
Figure 5.6: Flowchart of the retrieval process created for simulating retrievals from LIFE measurements using SASKTRAN-TIR.

number density profile is specified. The ozone profile is the initial guess of the retrieval vector, or the initial state vector, $\vec{n}_{x,0}$, in the Gauss-Newton iterative method described by Equation (5.8). Two retrieval tests are performed, with different initial guesses of the ozone profile, to investigate the impact of the initial guess on the retrieval. In the first test, the initial guess is the true ozone number density divided in half. The second test begins with an ozone density that is constant at all altitudes. Since the goal of this test is to test the Jacobian implementation solely for the number density of a single species, quantities such as temperature and pressure remain unchanged throughout the test. Sensitivity of the retrieval to pressure and temperature is beyond the scope of this thesis.

Microwindow Selection

The spectral microwindow is selected to minimize the impact of species other than ozone on the radiance. A microwindow of wavenumbers from 987.2 to 990.0 cm^{-1} is selected for this simulation. Figure 5.7 shows a typical output from the instrument model in this microwindow. The dotted black line indicates the radiance output when all species are included in the simulation, while the other lines show the simulated radiance for individual species. The figure shows that ozone dominates the signal at these wavenumbers, indicating that this microwindow is suitable for the retrieval of ozone. At lower altitudes carbon dioxide emissions have a noticeable effect on the signal, but their contribution is still small in comparison to ozone. However, if the atmospheric CO_2 concentration at the time and location of a real measurement were to increase significantly it could increase the effect on the radiance and would need to be taken into consideration when selecting a microwindow for ozone retrieval.

Ozone Retrieval 1: Starting from Half of True Profile

Often the first guess of a retrieval target is provided by a climatology because the magnitude and altitude variation of the true profile are likely to be similar. Here the initial guess is the profile taken from an ozone climatology then divided by 2, because the same climatology was also used to create the simulated measurement. Figure 5.8 shows the retrieved ozone profile in green, compared with the true ozone used to create the measurement vector in blue. The intermediate profiles from each Gauss-Newton iteration are plotted in black. A shaded green
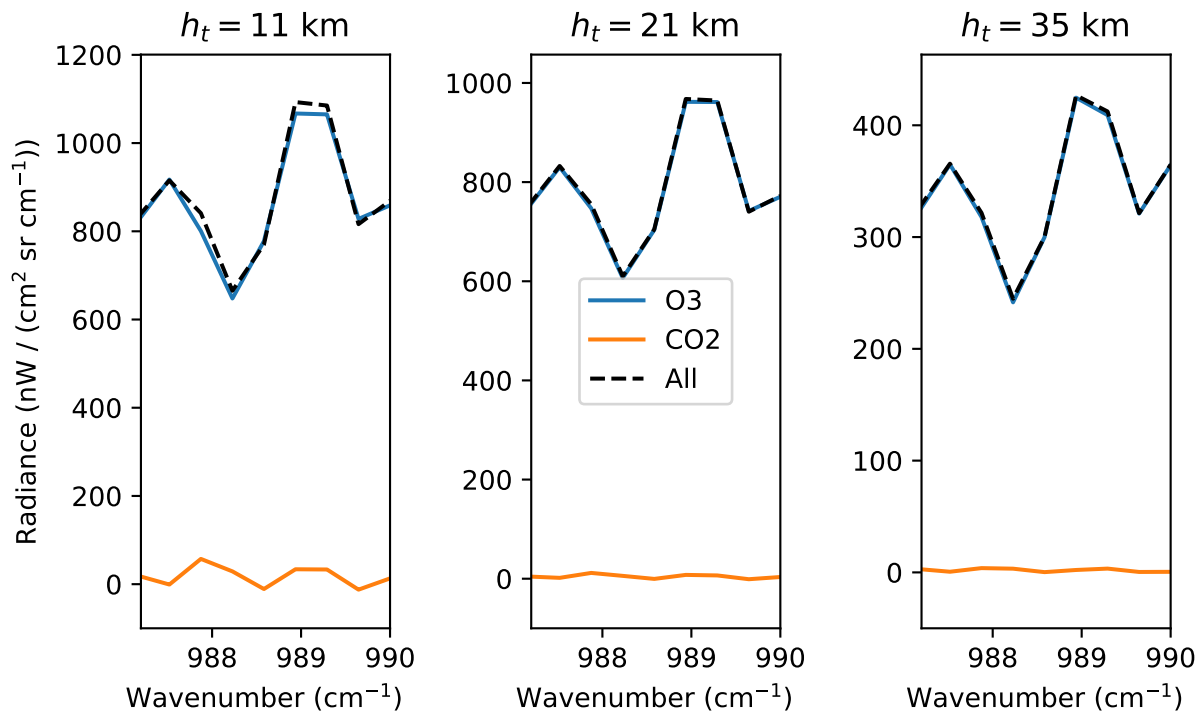
Figure 5.7: Simulated LIFE radiances in an ozone-dominated microwindow. Radiances simulated with only ozone and carbon dioxide are compared with a simulation in which all species are included. Tangent altitudes, h_t, of 11, 21, and 35 km are shown.

area indicates the standard deviation of the retrieved ozone, given by the square root of the diagonal elements of the solution covariance. The solution covariance, $\mathbf{S}$, that arises from the measurement covariance, $\mathbf{S_y}$, is given by

$$\mathbf{S} = ((\mathbf{K}^T\mathbf{S_y}^{-1}\mathbf{K} + \mathbf{S}_a^{-1})^T(\mathbf{K}^T\mathbf{S_y}^{-1}\mathbf{K} + \mathbf{S}_a^{-1}))^{-1}(\mathbf{K}^T\mathbf{S_y}^{-1}\mathbf{K} + \mathbf{S}_a^{-1})^T. \qquad (5.11)$$

Ten iterations of the retrieval algorithm were performed. The initial guess and the result after one iteration can be seen clearly on the left plot. They are both much smaller than the true profile. After two iterations, the profile becomes much closer to the true state. The final iteration shows good agreement, within 5%, for altitudes below 35 km. At higher altitudes the result becomes less accurate and it can be seen that with each iteration the retrieval alternates between underestimating and overestimating the true profile.

Techniques have been developed to address the overshooting issue, by adding a damping term to the iteration in Equation (2.114). The Levenberg-Marquardt algorithm is one such technique in which a damping term $\gamma\mathrm{diag}(\mathbf{K}_i^T\mathbf{S}_y^{-1}\mathbf{K}_i)$ is added to the iteration step (Marquardt, 1963). The positive parameter γ is used to adjust the amount of damping. The new form of the iteration is then

$$\vec{n}_{x,i+1} = \vec{n}_{x,i} + (\mathbf{K}_i^T\mathbf{S}_y^{-1}\mathbf{K}_i + \mathbf{S}_a^{-1} + \gamma\mathrm{diag}(\mathbf{K}_i^T\mathbf{S}_y^{-1}\mathbf{K}_i))^{-1}[\mathbf{K}_i^T\mathbf{S}_y^{-1}[\vec{y} - \mathbf{F}(\vec{n}_{x,i})] - \mathbf{S}_a^{-1}(\vec{n}_{x,i} - \vec{n}_{x,a})].$$
$$(5.12)$$

Introducing the Levenberg-Marquardt damping term with $\gamma = 20.0$ and increasing the number of iterations to 20 results in the retrieved ozone profile shown in Figure 5.8. The damping increases the number of iterations required to approach the true ozone profile, but with the end result that the result now shows excellent agreement at high altitudes. A side effect of the algorithm is a slightly greater error near 20 km as the damping now causes an undershooting of the true value. This problem may be alleviated through fine tuning of γ, increasing the number of iterations, or by modifying the retrieval algorithm so that γ is allowed to change between iterations. Modifications to assist in the determination of optical γ values are beyond the scope of this thesis but may be beneficial when real measurement data is incorporated in the retrieval algorithm. Regardless, the test shows the ability to retrieve the ozone profile when a reasonable initial guess is provided, which varies in altitude similarly to the true ozone profile.
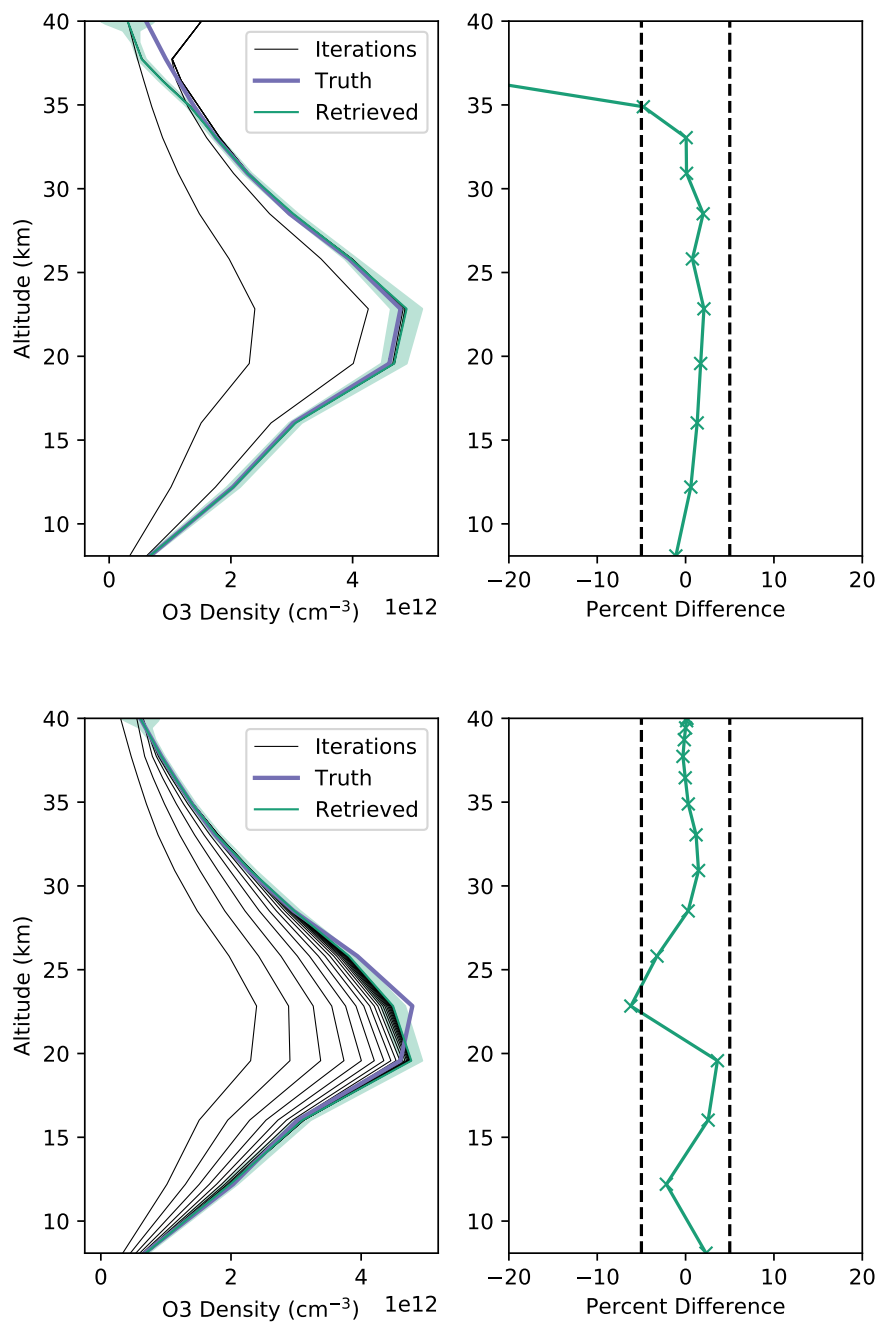
Figure 5.8: Top: Simulated retrieval of ozone number density. The initial guess is the true profile divided by 2. Note that the retrieval grid, indicated by markers on the percent difference line, is the sixteen tangent altitudes from the LIFE measurement. Bottom: Same retrieval performed with Levenberg-Marquardt damping.
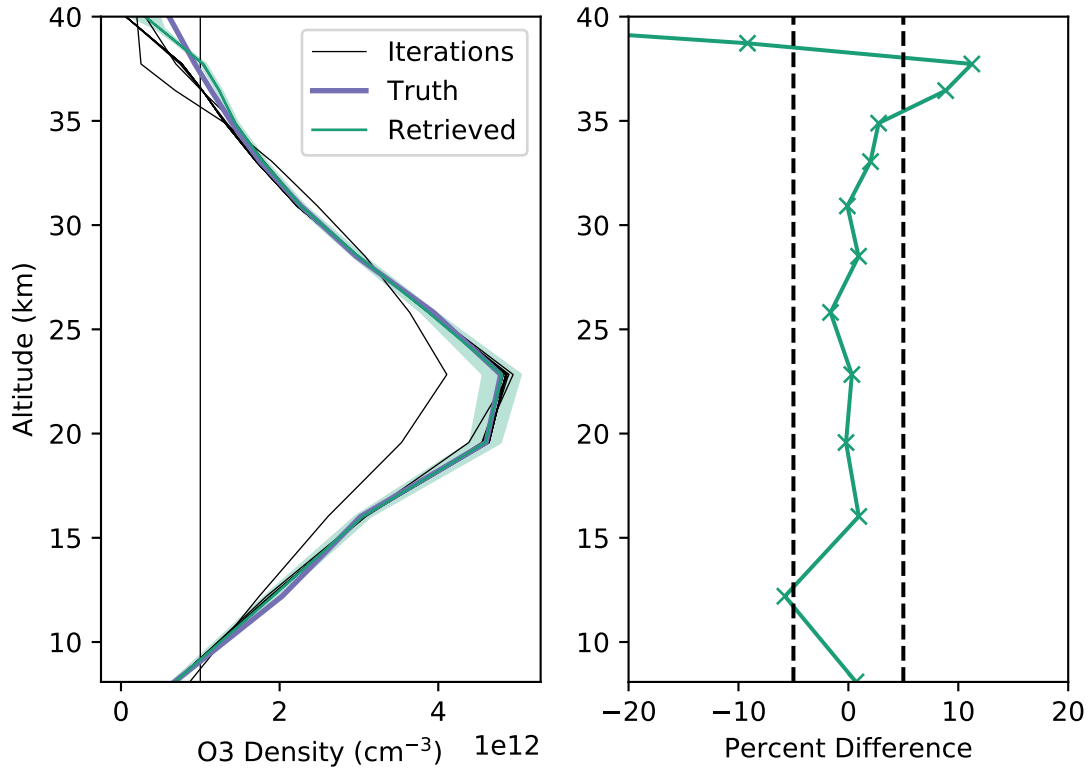
Figure 5.9: Ozone number density retrieval with a constant initial guess of 10^{12} cm^{-3}.

Ozone Retrieval 2: Starting from Constant Number Density

This test demonstrates the ability of the retrieval to determine the shape of the profile from a constant value. It shows how the weighting functions apply differing perturbations at each altitude to recreate the structure of the true profile. With the exception of the initial guess, the retrieval uses the same climatologies, lines of sight, and microwindow as the previous simulation. Similarly to the previous test, a damping parameter of $\gamma = 0.05$ is applied in each of the 20 iterations. The retrieved profile is shown in Figure 5.9 and agrees within 5% in the middle altitudes with larger errors occurring at the top and bottom of the profile. In general, the retrieval is able to determine the shape of the ozone profile. However, this test demonstrates how the initial guess can effect or bias the result of the retrieval.
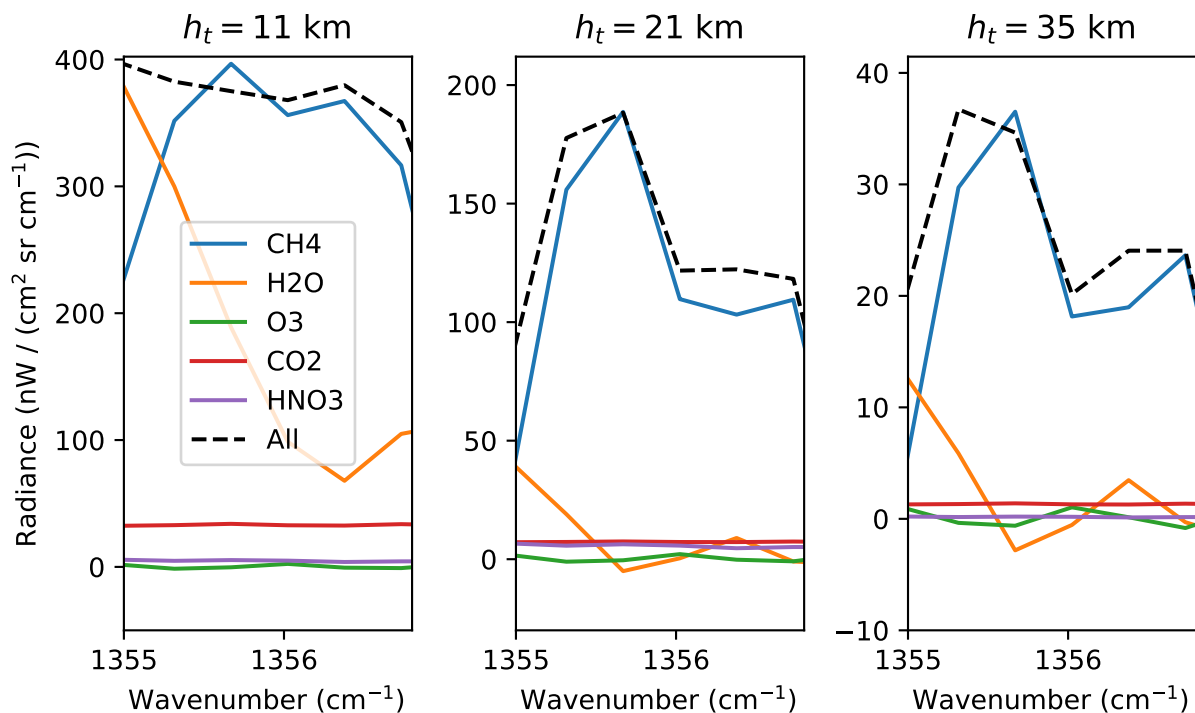
Figure 5.10: Simulated LIFE radiances in an methane-dominated microwindow, compared with individual radiances from methane, water vapour, ozone, carbon dioxide, and nitric acid. Tangent altitudes, h_t, of 11, 21, and 35 km are shown.

5.2.2 Methane VMR Retrieval

It is important to test the retrieval with different target species. Each species' atmospheric abundance and spectral features require different considerations when performing the retrieval. In this test the ability of the model to retrieve a methane profile is evaluated. A microwindow of wavenumbers in the range 1355.0 to 1356.8 cm^{-1} is chosen, and typical radiances for this range are shown in Figure 5.10. The radiance is this microwindow is smaller than the ozone microwindow in Figure 5.7, and at higher altitudes is on the order of the NESR in Figure 5.5. This is important to keep in mind when examining the uncertainty of the retrieved profile.

While ozone number density peaks in the stratosphere, typically near 20 km, concentration of methane is generally in constant proportion with the total atmospheric air density. The methane number density decreases exponentially with altitude with the overall air density. Therefore, the VMR is often retrieved instead of number density. Figure 5.11 shows a retrieval
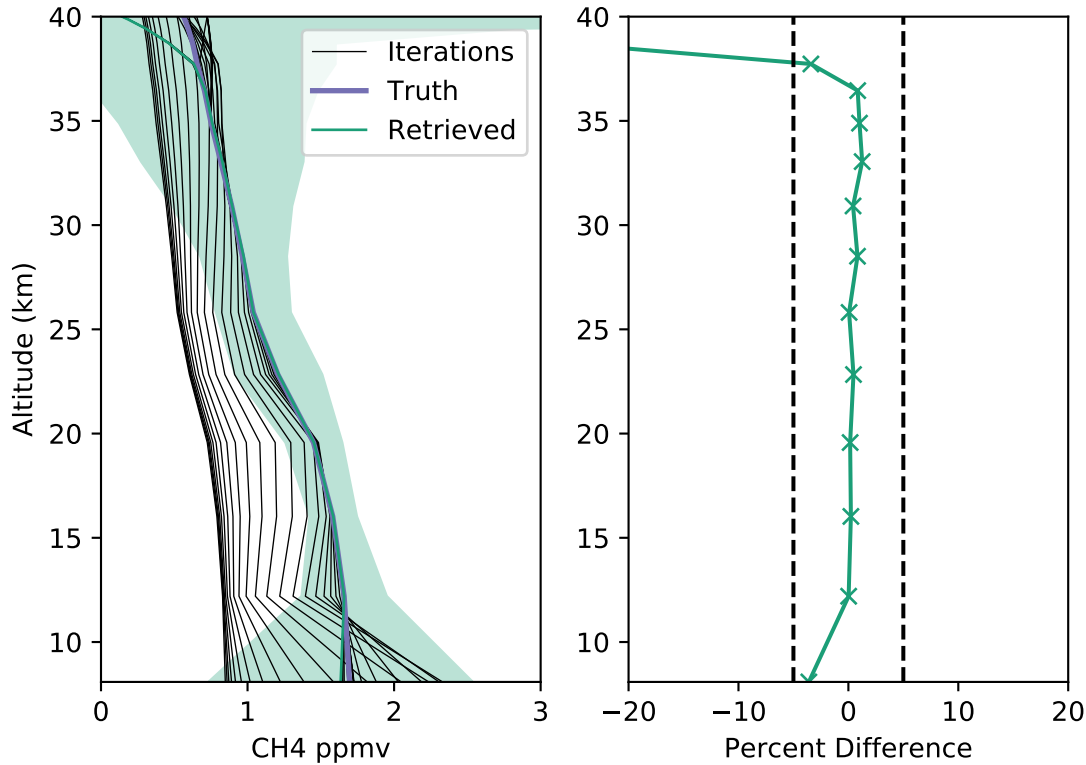
Figure 5.11: Simulated retrieval of methane VMR. The initial guess is half the value of the true methane profile and Levenberg-Marquardt damping is applied.

of methane VMR, in parts per million by volume (ppmv), from a simulated measurement. Similar to previous tests, the initial guess is set to half of the true methane profile and a Levenberg-Marquardt damping term is added in the retrieval. The retrieved VMR shows good agreement with the true profile at high altitudes with some larger variations towards lower altitudes. This error could be a result of the greater abundance of water vapour at lower altitudes and its increased impact on the measured radiance, as seen in Figure 5.10. Additionally, the uncertainty in the result is much greater than in the ozone tests because the radiances are smaller and approach a similar magnitude to the NESR. The result is promising, and shows that a methane retrieval is feasible and could likely be improved with further optimization of the retrieval parameters and microwindow.
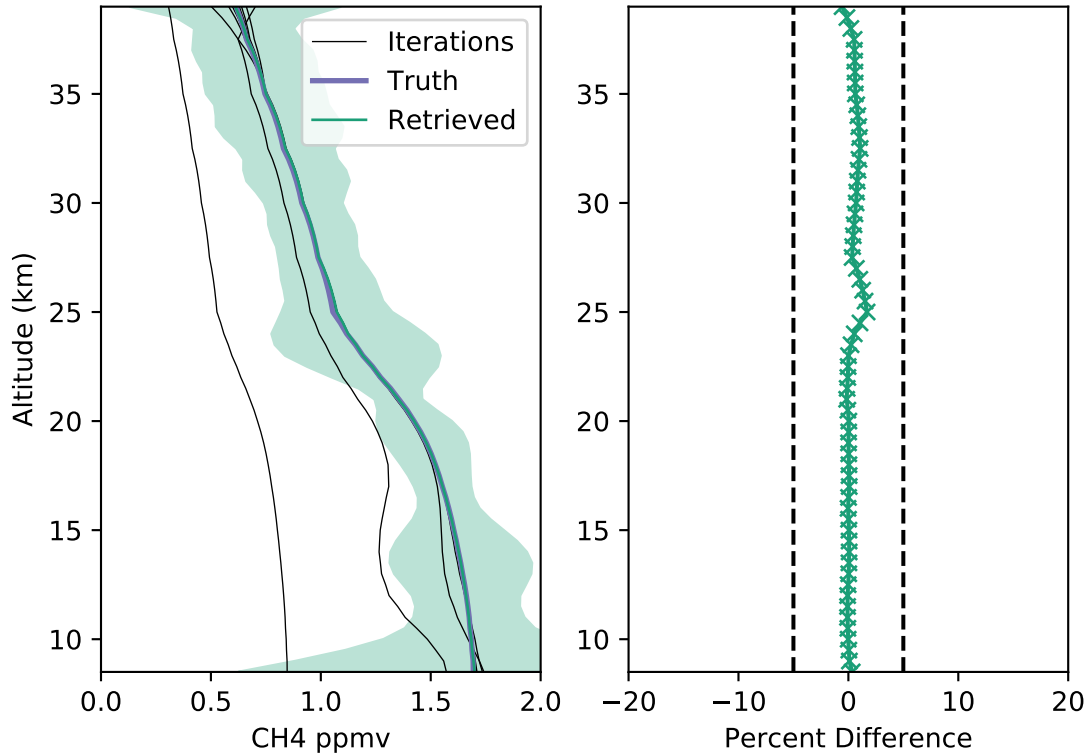
Figure 5.12: Simulated retrieval of methane VMR on a 500 m grid, using second-order Tikhonov regularization. The initial guess is set at half the value of the true methane VMR.

Methane Retrieval with Tikhonov Regularization

In the next simulation, the altitudes at which the methane VMR is retrieved are changed from the 16 altitudes imaged by the LIFE sensor array to an evenly spaced grid at a resolution of 500 m. Recall from Section 2.5.2 that the problem is underdetermined when the number of measurements is fewer than the number of parameters being retrieved. The measurements alone do not provide enough information to determine the VMR profile and regularization is required to constrain the solution. Using a second order Tikhonov regularization, as described in Section 2.5.4, makes it possible to obtain methane VMR on a 500 m grid. Figure 5.12 shows the methane profile obtained with this method.

The retrieved methane shows strong agreement with the true profile. This result is an important proof of concept for LIFE retrievals and demonstrates that profiles may be retrieved

at more vertical samples than given by the 16 detector pixels. The ability to retrieve the true profile shows that the analytic Jacobian calculations in the TIR engine are producing correct results.

6 Conclusion

6.1 Summary and Conclusions

In September 2019, the LIFE instrument was mounted on a high-altitude balloon and launched from Timmins, Ontario. LIFE successfully captured vertical images of the atmosphere with a Fourier transform spectrometer. To obtain useful information about the structure and composition of the atmosphere from these interferograms it was necessary to develop a fast, computationally efficient infrared model for the SASKTRAN radiative transfer framework that is capable of calculating analytic Jacobians. Creation of an infrared engine compatible with the SASKTRAN framework greatly simplifies interfacing with existing software components developed by the University of Saskatchewan atmospheric research group. These components include climatologies, optical properties, retrieval algorithms, and data trend analysis software. Additionally, the new engine must be computationally efficient and capable of performing rapid successive calculations in a retrieval algorithm.

The SASKTRAN-TIR engine accomplishes these goals by providing a radiative transfer model that implements an iterative algorithm, shown in Equation (3.6), to calculate the propagation of radiation along a line sight. Chapter 3 describes the details of the TIR engine. Along the line of sight, thermal emissions from greenhouse gases increase the radiance while absorption by these same gases decreases the radiance. Absorption cross sections are calculated using parameters from the HITRAN database. SASKTRAN-TIR is shown to produce results that agree with the ARTS model for both nadir and limb observations, as seen in Figures 3.6, 3.7, and 3.8. This agreement indicates that the TIR engine is capable of accurately modelling radiance measurements. In addition to the new TIR engine, modifications are made to the HR engine that make it possible to perform radiative transfer calculations in the mid infrared where the radiation due to both scattered sunlight and ther-

mal emissions are similar in magnitude. The addition of a thermal emission radiation source to SASKTRAN-HR was shown to be correct by a comparison with the ARTS model as seen in Figure 3.1.

As described in Chapter 4, the TIR engine calculates analytic Jacobians in parallel with radiance to enable the fast retrieval of profiles of greenhouse gas composition. Analytic expressions for computing the derivative of the observed radiance with respect to the number density or VMR of a gas species are developed (see Equation (4.7) for the number density Jacobian and (4.9) for the modification needed to compute VMR Jacobians). The accuracy of these Jacobians is verified by a comparison with significantly slower perturbation methods. This comparison can be seen in Figures 4.1 and 4.3 which show strong agreement between the two methods. In combination with the model verifications in Chapter 3, these results show that SASKTRAN-TIR is an accurate forward model which also computes the Jacobians required in the retrieval of greenhouse gas profiles from thermal infrared observations.

In Chapter 5, the feasibility of applying the TIR engine and its analytic Jacobians to measurements from the LIFE instrument is demonstrated. An instrument model is developed which transforms high resolution radiances computed by SASKTRAN-TIR into lower resolution radiances by convolution with the LIFE instrument line shape. By applying a Gauss-Newton iterative retrieval algorithm with the LIFE instrument forward model, profiles of ozone and methane are successfully retrieved from simulated measurements. The retrieval simulations highlight several important considerations for continued work on LIFE retrievals in the coming years. For example, selecting an appropriate spectral microwindow in which the target species has a significant impact on the radiance and contributions from other species are minimized is essential for accurate retrievals. Another modification that is often applied to the retrieval is a Levenberg-Marquardt damping technique, as demonstrated by the ozone retrieval simulation shown in Figure 5.8. This simulation illustrates how damping prevented the retrieved profile from repeatedly overshooting the solution at higher altitudes, but it is also necessary to consider how the retrieved profile near 25 km becomes overdamped and does not reach the true solution. Fine tuning of the damping parameter may reduce the error in the retrieved profile.

In the simulated retrievals of methane, the VMR of the species is retrieved instead of

number density. For many species, the VMR experiences very small changes with altitude and remains fairly stable. Additionally, methane VMR was retrieved on a constant grid with 500 m vertical spacing, as opposed to the previous retrievals at the 16 tangent altitudes imaged by LIFE. A second-order Tikhonov regularization was applied to retrieve the methane profile shown in Figure 5.12, which shows good agreement with the true profile used to create the simulated measurement. These simulations show that the framework is suitable for use by the LIFE team in the analysis of real data.

The SASKTRAN-TIR engine with analytic Jacobian calculations and the LIFE retrieval framework developed in this thesis are an important tool for future research projects related to LIFE and infrared remote sensing at the University of Saskatchewan. In the coming years this software will be used in retrievals of atmospheric composition using measurements from the prototype LIFE instrument and future iterations, contributing to an increased knowledge of the composition of the UTLS atmospheric region.

6.2 Future Work

There are two main areas in which work on this project may be continued. First, there are several areas in which the features and physical accuracy of the TIR engine may be enhanced. A more rigorous verification of the performance and capabilities is desirable. Second, the primary continuation of this work will be in the retrieval of constituent profiles using real measurements from the LIFE instrument. This work will be performed by other members of the LIFE team in the near future using real data from the 2019 LIFE campaign in Timmins and for the many variations of the LIFE project in the coming years.

6.2.1 Engine Development

The TIR engine was developed with the assumption of Local Thermodynamic Equilibrium (LTE). Models have such as KOPRA have incorporated non-LTE modifications in the calculation of thermal emission source functions and absorption cross sections, but note that it is generally safe to assume LTE for altitudes below the mesosphere (Funke and Höpfner, 2000). Since LIFE measures from a balloon platform near 40 km, the tangent altitudes are in the

troposphere and stratosphere and there would be little benefit from non-LTE additions. If the TIR engine were to be utilized for satellite measurements with higher tangent altitudes, it may be necessary to consider non-LTE effects.

Currently, SASKTRAN calculates absorption cross sections in a line-by-line mode where a wavenumber window determines the spectral lines that are included in the calculation. For some species, particularly water vapour and carbon dioxide for thermal infrared simulations, the cross section calculations can be improved by including a baseline continuum. For carbon dioxide, the continuum results from the contribution of a large number of distant broadened spectral lines that accumulate to have a noticeable effect on the cross section in the target microwindow (Echle and Höpfner, 2000). In SASKTRAN, it is possible to account for these far off lines by making the wavenumber window larger at the cost of significantly slower radiance computations. Carbon dioxide absorption and emission dominates atmospheric absorption in the 560 to 790 cm^{-1} range (Bignell et al., 1963). Extending the wavenumber window of thermal infrared calculations to include this range be necessary, particularly if the retrieval microwindow is towards the lower 700 cm^{-1} end of the LIFE measurement window. A precomputed table of carbon dioxide absorption for a range of wavenumbers and temperatures may be implemented, which is the method used by KOPRA for accounting for any spectral lines outside a 25 cm^{-1} window around the calculation range (Echle and Höpfner, 2000). Water vapour is another species for which a continuum can be applied to in the infrared regime. The CKD water vapour continuum (Mlawer et al., 1999) models the baseline absorption and has been used in the retrieval of ozone profiles from MIPAS infrared measurements (Glatthor et al., 2006).

To determine if the additions described in this section will have an impact on radiance simulations in the thermal infrared it will be necessary to perform further tests and comparisons with existing models. A good initial test is enabling continuum absorption in ARTS and comparing the accuracy and computation speed of the simulation to one performed in SASKTRAN-TIR with no continuum. If there are significant differences, it may be necessary to incorporate continuum absorption in SASKTRAN.

6.2.2   LIFE Retrievals

In Chapter 5 it was shown that ozone and methane profiles could be retrieved from simulated LIFE measurements. A profile of methane ppmv was successfully retrieved with a resolution of 500 m, from a simulated image containing 16 lines of sight. The next step is to perform retrievals using real measurements from the LIFE campaign. This process will be significantly more difficult to the larger number of unknown factors and sources of error present. There will be uncertainties in the tangent altitudes imaged and the contents of all atmospheric species, not only the targeted retrieval species. Two major areas to consider are the selection of microwindows and the atmospheric temperature input to the model.

The atmospheric temperature has an effect on the broadening of spectral lines and, more importantly, the magnitude of the thermal emission source function. The amount of radiation that is added at any point along a line of sight is highly dependent on the temperature at that location. Therefore, it is important that the atmospheric state of SASKTRAN contains a correct temperature profile or the retrievals will be incorrect. Temperatures may be obtained from a climatology model such as the ECMWF ERA reanalysis which is already implemented in SASKTRAN (Berrisford et al., 2011). An alternative approach is to first use LIFE measurements to retrieve a temperature profile, then input that profile into the model during the retrieval of gas profiles. Temperature retrievals can be performed using microwindows with significant contributions from carbon dioxide spectral lines because the carbon dioxide composition has been determined to high accuracy (Krisch et al., 2017). This approach has the advantage of determining the temperature for the exact time and location of the measurement, provided that the retrieved temperature is correct.

References

Anderson, G. P., Clough, S. A., Kneizys, F., Chetwynd, J. H., and Shettle, E. P. (1986). AFGL atmospheric constituent profiles (0-120 km). Technical report, U.S. Air Force Geophysics Laboratory.

Bates, D. (1984). Rayleigh scattering by air. *Planetary and Space Science*, 32(6):785–790.

Berrisford, P., Dee, D., Poli, P., Brugge, R., Fielding, K., Fuentes, M., Kallberg, P., Kobayashi, S., Uppala, S., and Simmons, A. (2011). The ERA-interim archive, version 2.0.

Bignell, K., Saiedy, F., and Sheppard, P. (1963). On the atmospheric infrared continuum. *JOSA*, 53(4):466–479.

Bourassa, A., Degenstein, D., and Llewellyn, E. (2008). SASKTRAN: A spherical geometry radiative transfer code for efficient estimation of limb scattered sunlight. *Journal of Quantitative Spectroscopy and Radiative Transfer*, 109(1):52 – 73.

Bourassa, A. E., Degenstein, D. A., Gattinger, R. L., and Llewellyn, E. J. (2007). Stratospheric aerosol retrieval with optical spectrograph and infrared imaging system limb scatter measurements. *Journal of Geophysical Research: Atmospheres*, 112(D10).

Buehler, S. A., Mendrok, J., Eriksson, P., Perrin, A., Larsson, R., and Lemke, O. (2018). ARTS, the atmospheric radiative transfer simulator – version 2.2, the planetary toolbox edition. *Geoscientific Model Development*, 11(4):1537–1556.

Buijs, H. L. (2012). Beamsplitter configuration for optical subtraction of self emission with fourier transform spectrometer in dual input port mode.

Decker, B. L. (1986). World geodetic system 1984. Technical report, Defense Mapping Agency Aerospace Center St Louis Afs Mo.

Echle, G. and Höpfner, M. (2000). Parameterization of continua caused by gaseous constituents. *The Karlsruhe Optimized and Precise Radiative Transfer Algorithm (KOPRA)*, pages 89–94.

Endemann, M. (1999). MIPAS instrument concept and performance. In *Proceedings of the European Symposium on Atmospheric Measurements from Space*, volume 1, pages 29–43.

Eriksson, P., Buehler, S., Emde, C., Sreerekha, T., Melsheimer, C., and Lemke, O. (2005). ARTS user guide.

Friedl-Vallon, F., Gulde, T., Hase, F., Kleinert, A., Kulessa, T., Maucher, G., Neubert, T., Olschewski, F., Piesch, C., Preusse, P., Rongen, H., Sartorius, C., Schneider, H., Schönfeld, A., Tan, V., Bayer, N., Blank, J., Dapp, R., Ebersoldt, A., Fischer, H., Graf, F., Guggenmoser, T., Höpfner, M., Kaufmann, M., Kretschmer, E., Latzko, T., Nordmeyer, H., Oelhaf, H., Orphal, J., Riese, M., Schardt, G., Schillings, J., Sha, M. K., Suminska-Ebersoldt, O., and Ungermann, J. (2014). Instrument concept of the imaging fourier transform spectrometer GLORIA. *Atmospheric Measurement Techniques*, 7(10):3565–3577.

Funke, B. and Höpfner, M. (2000). Non-LTE and radiative transfer. *The Karlsruhe Optimized and Precise Radiative Transfer Algorithm (KOPRA), edited by: Stiller, GP, Wissenschaftliche Berichte FZKA*, 6487:101–106.

Glatthor, N., Von Clarmann, T., Fischer, H., Funke, B., Gil-López, S., Grabowski, U., Höpfner, M., Kellmann, S., Linden, A., López-Puertas, M., et al. (2006). Retrieval of stratospheric ozone profiles from MIPAS/ENVISAT limb emission spectra: a sensitivity study.

Gordon, I. E., Rothman, L. S., Hill, C., Kochanov, R. V., Tan, Y., Bernath, P. F., Birk, M., Boudon, V., Campargue, A., Chance, K., et al. (2017). The HITRAN2016 molecular spectroscopic database. *Journal of Quantitative Spectroscopy and Radiative Transfer*, 203:3–69.

Griessbach, S., Hoffmann, L., Höpfner, M., Riese, M., and Spang, R. (2013). Scattering in infrared radiative transfer: A comparison between the spectrally averaging model JURASSIC and the line-by-line model KOPRA. *Journal of Quantitative Spectroscopy and Radiative Transfer*, 127:102–118.

Hecht, E. (2002). *Optics*. Addison Wesley, 4th ed edition.

Hedin, A. E. (1991). Extension of the MSIS thermosphere model into the middle and lower atmosphere. *Journal of Geophysical Research: Space Physics*, 96(A2):1159–1172.

Hoepfner, M., Stiller, G. P., Kuntz, M., von Clarmann, T., Echle, G., Funke, B., Glatthor, N., Hase, F., Kemnitzer, H., and Zorn, S. (1998). Karlsruhe optimized and precise radiative transfer algorithm: II. Interface to retrieval applications. In Wang, J., Wu, B., Ogawa, T., and hua Guan, Z., editors, *Optical Remote Sensing of the Atmosphere and Clouds*, volume 3501, pages 186 – 195. International Society for Optics and Photonics, SPIE.

Höpfner, M., Larsen, N., Spang, R., Luo, B. P., Ma, J., Svendsen, S., Eckermann, S. D., Knudsen, B., Massoli, P., Cairo, F., et al. (2006). MIPAS detects antarctic stratospheric belt of NAT PSCs caused by mountain waves.

Hulley, G. C., Hook, S. J., Abbott, E., Malakar, N., Islam, T., and Abrams, M. (2015). The ASTER global emissivity dataset (ASTER GED): Mapping Earth's emissivity at 100 meter spatial scale. *Geophysical Research Letters*, 42(19):7966–7976.

Jensen, K. (2015). The inclusion of thermal emissions within the SASKTRAN framework. Master's thesis, University of Saskatchewan.

Joos, F. and Spahni, R. (2008). Rates of change in natural and anthropogenic radiative forcing over the past 20,000 years. *Proceedings of the National Academy of Sciences*, 105(5):1425–1430.

Krisch, I., Preusse, P., Ungermann, J., Dörnbrack, A., Eckermann, S. D., Ern, M., Friedl-Vallon, F., Kaufmann, M., Oelhaf, H., Rapp, M., et al. (2017). First tomographic observations of gravity waves by the infrared limb imager GLORIA. *Atmos. Chem. Phys*, 17(14):937–14.

Kuntz, M. (1997). A new implementation of the Humlicek algorithm for the calculation of the Voigt profile function. *Journal of Quantitative Spectroscopy and Radiative Transfer*, 57(6):819 – 824.

Llewellyn, E., Lloyd, N., Degenstein, D., Gattinger, R., Petelina, S., Bourassa, A., Wiensz, J., Ivanov, E., McDade, I., Solheim, B., et al. (2004). The OSIRIS instrument on the Odin spacecraft. *Canadian Journal of Physics*, 82(6):411–422.

Marquardt, D. W. (1963). An algorithm for least-squares estimation of nonlinear parameters. *Journal of the Society for Industrial and Applied Mathematics*, 11(2):431–441.

McEvoy, A., Markvart, T., Castañer, L., Markvart, T., and Castaner, L. (2003). *Practical handbook of photovoltaics: fundamentals and applications*. Elsevier.

McPeters, R. D., Labow, G. J., and Johnson, B. J. (1997). A satellite-derived ozone climatology for balloonsonde estimation of total column ozone. *Journal of Geophysical Research: Atmospheres*, 102(D7):8875–8885.

Mie, G. (1908). Beiträge zur optik trüber medien, speziell kolloidaler metallösungen. *Annalen der physik*, 330(3):377–445.

Mlawer, E., Clough, S., Brown, P., and Tobin, D. (1999). Recent developments in the water vapor continuum. In *Proceedings of the ninth ARM science team meeting*, pages 1–6.

Read, W. G., Shippony, Z., and Snyder, W. (2004). Microwave limb sounder (mls) forward model algorithm theoretical basis document. Technical Report JPL D-18130, Jet Propulsion Laboratory.

Riese, M., Friedl-Vallon, F., Spang, R., Preusse, P., Schiller, C., Hoffmann, L., Konopka, P., Oelhaf, H., von Clarmann, T., and Höpfner, M. (2005). Global limb radiance imager for the atmosphere (GLORIA): scientific objectives. *Advances in Space Research*, 36(5):989–995.

Riese, M., Oelhaf, H., Preusse, P., Blank, J., Ern, M., Friedl-Vallon, F., Fischer, H., Guggenmoser, T., Höpfner, M., Hoor, P., et al. (2014). Gimballed limb observer for radiance imaging of the atmosphere (GLORIA) scientific objectives. *Atmospheric measurement techniques*, 7(7):1915–1928.

Rodgers, C. D. (2000). *Inverse methods for atmospheric sounding: theory and practice*, volume 2. World scientific.

Rothman, L. S., Rinsland, C., Goldman, A., Massie, S., Edwards, D., Flaud, J., Perrin, A., Camy-Peyret, C., Dana, V., Mandin, J.-Y., et al. (1998). The HITRAN molecular spectroscopic database and HAWKS (HITRAN atmospheric workstation): 1996 edition. *Journal of quantitative spectroscopy and radiative transfer*, 60(5):665–710.

Runge, E. (2018). Limb imaging fourier transform spectrometer experiment (LIFE). Master's thesis, University of Saskatchewan.

Shaw, R. A. and Mantsch, H. H. (1999). Near-IR spectrometers. In Lindon, J. C., editor, *Encyclopedia of Spectroscopy and Spectrometry*, pages 1451 – 1461. Elsevier, Oxford.

Shen, S. (1994). Comparison and competition between MCT and QW structure material for use in IR detectors. *Microelectronics Journal*, 25(8):713–739.

Theriault, J.-M. (2001). Fourier-transform spectrometer configuration optimized for self emission suppression and simplified radiometric calibration.

Thompson, D. A., Pepin, T. J., and Simon, F. W. (1982). Ray tracing in a refracting spherically symmetric atmosphere. *JOSA*, 72(11):1498–1501.

Tikhonov, A. (1943). On the stability of inverse problems. *Dokl. akad. nauk sssr*, 39(5):195–198.

True, S. (2004). Planning the future of the world geodetic system 1984. In *PLANS 2004. Position Location and Navigation Symposium (IEEE Cat. No. 04CH37556)*, pages 639–648. IEEE.

Williams, D. R. (2016). Planetary fact sheets. *NASA Goddard Space Flight Center*.

Yokota, T., Yoshida, Y., Eguchi, N., Ota, Y., Tanaka, T., Watanabe, H., and Maksyutov, S. (2009). Global concentrations of CO2 and CH4 retrieved from GOSAT: First preliminary results. *Sola*, 5:160–163.

Zawada, D. J., Dueck, S. R., Rieger, L. A., Bourassa, A. E., Lloyd, N. D., and Degenstein, D. A. (2015). High-resolution and monte carlo additions to the SASKTRAN radiative transfer model. *Atmospheric Measurement Techniques*, 8(6):2609–2623.

imekov, M., Jacquemart, D., Rothman, L. S., Gamache, R. R., and Goldman, A. (2006). Einstein A-coefficients and statistical weights for molecular absorption transitions in the HITRAN database. *Journal of Quantitative Spectroscopy and Radiative Transfer*, 98(1):130 – 155.

Appendix A

Surface Temperature of the Earth

In this Appendix, the surface temperature is derived for an Earth with no atmosphere as a demonstration of the principles of radiative balance. Radiative balance describes an equilibrium situation in which the energy lost by the planet through radiation is equal to energy gained by incident radiation from the sun. In thermal equilibrium, the planet can be approximated as a black body with surface temperature T_p. Absorption and emission of radiation by the atmosphere is ignored.

Modelling the solar radiation as a black body, the Stefan-Boltzmann law states the radiant energy emitted per unit time and surface area, known as the solar radiant flux F_s, is equal to

$$F_s = \sigma T_s^4 \tag{A.1}$$

where T_s is the surface temperature of the sun and σ is the Stefan-Boltzmann constant. Let d_p be the distance between Earth and the sun and R_s be the radius of the sun. If the sun radiates uniformly in all directions, the solar energy flux arriving at the surface of the planet, F_p, is scaled by the surface area of the sun divided by the surface area of a sphere with radius d_p,

$$F_p = \frac{4\pi R_s^2}{4\pi d_p^2} F_s = \frac{R_s^2}{d_p^2} \sigma T_s^4 \tag{A.2}$$

Some of this radiation is absorbed by the planetary surface and the remainder is reflected, quantified by the albedo, a. The albedo of a surface is defined as the ratio of radiant flux that is reflected by the surface to the total flux incident on the surface,

$$a = \frac{F_{\text{reflected}}}{F_{\text{incident}}} \tag{A.3}$$

In this problem, the incident flux is radiation that reaches the planet, F_p. Therefore, aF_P describes the radiation that is reflected by the surface which does not add to the energy of the Earth system, and $(1-a)F_p$ is the radiation absorbed by the Earth. The total energy flux to the planetary surface is

$$F_{\text{in}} = (1-a)F_p = (1-a)\frac{R_s^2}{d_p^2} \sigma T_s^4 \tag{A.4}$$

Description	Variable	Value
Sun effective temperature	T_s	5772 K
Sun mean radius	R_s	695.7×10^3 km
Planetary albedo	a	0.306
Earth orbit radius	d_p	149.6×10^6 km

Table A.1: Parameters of the Earth and Sun (Williams, 2016)

The effective area that incoming solar radiation sees is a circle with radius R_p, where R_p is the radius of the Earth. Therefore, the total radiative power input to the planet is

$$P_{\text{in}} = \pi R_p^2 F_{\text{in}} = \pi R_p^2 (1-a) \frac{R_s^2}{d_p^2} \sigma T_s^4 \tag{A.5}$$

Modelling Earth as a black body, the radiant flux emitted by the planet is given by the Stefan-Boltzmann law as

$$F_{\text{out}} = \sigma T_p^4 \tag{A.6}$$

where T_p is the average temperature of Earth's surface. It is assumed that the planet rotates quickly enough so that solar radiation is distributed across the entire surface and is reradiated uniformly. Under this assumption, the Earth radiates uniformly across the entire surface area of the planet, $4\pi R_p^2$. Therefore, the outward radiative power is

$$P_{\text{out}} = 4\pi R_p^2 F_{\text{out}} = 4\pi R_p^2 \sigma T_p^2 \tag{A.7}$$

For radiative balance, the total input radiative power is equal to the total output power. Setting Equation (A.5) equal to (A.7) and solving for the planetary surface temperature results in

$$T_p = T_s \left[\frac{1}{4} \frac{R_s^2}{d_p^2} (1-a) \right]^{1/4} \tag{A.8}$$

Evaluating this expression using the parameter listed in Table A.1 results in a surface temperature of 254 K, much colder than the actual average temperature, 288 K. The reason for this discrepancy is that the atmosphere and greenhouse effect have been neglected, which results in a warming effect.

Appendix B

Planck Function

The Planck function describes the radiant energy that is emitted by a black body. It is important component in infrared radiative transfer because it quantifies emissions from greenhouse gases, the primary radiation source in the thermal infrared regime. This Appendix provides a derivation of the Planck function.

Consider a cube with a side length of L, which contains some electromagnetic radiation. The goal is to determine the energy density in an interval between frequencies f and $f + \mathrm{d}f$ of the radiation contained within this cube of volume L^3. Begin by counting the number of modes of oscillation in the volume. Assuming periodic electromagnetic radiation, the sides of the cube impose a zero-amplitude boundary condition. In the x direction, this condition restricts wavelengths to

$$\lambda_x = \frac{2L}{n_x} \tag{B.1}$$

where n_x is a positive integer. The corresponding permitted wavenumbers, $k_x = 2\pi/\lambda_x$, are then given by

$$k_x = \frac{\pi n_x}{L} \tag{B.2}$$

Solving for n_x and differentiating both sides gives

$$\mathrm{d}n_x = \frac{L}{\pi}\mathrm{d}k_x \tag{B.3}$$

which describes the number of modes of oscillation in the wavenumber interval k_x to $k_x + \mathrm{d}k_x$.

The next step is to consider all three dimensions of the box. Let N be the total number of modes in the volume, then

$$\mathrm{d}N = \mathrm{d}n_x\mathrm{d}n_y\mathrm{d}n_z = \frac{L^3}{\pi^3}\mathrm{d}k_x\mathrm{d}k_y\mathrm{d}k_z \tag{B.4}$$

where Equation (B.3) was subbed in for each dimension. The term $\mathrm{d}k_x\mathrm{d}k_y\mathrm{d}k_z$ describes a three-dimensional volume in k-space. It is the volume contained between the spherical shells with radius k and $k + \mathrm{d}k$, where $k = \sqrt{k_x^2 + k_y^2 + k_z^2}$. This volume is equal to $4\pi k^2 \mathrm{d}k$, but must also be divided by 8 because only the positive octant of k-space is required. As

shown in Equation (B.2), each dimension of k depends on a positive integer and therefore will always be positive. Substituting the k-space volume into Equation (B.4) gives $L^3/(2\pi^2)k^2\mathrm{d}k$. However, this expression is not quite correct because each mode of oscillation can have two independent polarizations. Therefore, the number of modes is multiplied by 2, resulting in

$$\mathrm{d}N = \frac{L^3 k^2}{\pi^2}\mathrm{d}k \tag{B.5}$$

Now it is possible determine the number of modes in the interval of frequencies from f to $f + \mathrm{d}f$. Wavenumber can be written as $k = 2\pi f/c$ where c is the speed of light. The corresponding differential expression is $\mathrm{d}k = 2\pi c^{-1}\mathrm{d}f$. Substituting these expressions into Equation (B.5) and dividing by L^3 gives the number of modes per unit volume,

$$\frac{\mathrm{d}N}{L^3} = \frac{8\pi f^2}{c^3}\mathrm{d}f \tag{B.6}$$

The density of modes given by Equation (B.6) can be used to determine the energy density of this electromagnetic radiation. Classically, each mode of oscillation has an average energy equal to kT, where k is the Boltzmann constant and T is the temperature, assuming thermodynamic equilibrium. The oscillator has average kinetic and potential energies that are both equal to $kT/2$. Therefore, the energy density, $u(f)$, will be equal to the number of modes given by Equation (B.6) multiplied by the average energy of each mode, kT, which gives

$$u(f) = \frac{8\pi f^2}{c^3}kT \tag{B.7}$$

Equation (B.7) is also called the Rayleigh-Jeans law. However, while the Rayleigh-Jeans law appears correct at lower frequencies, it becomes unphysical at larger frequencies, resulting in

$$\int_0^\infty u(f)\mathrm{d}f \to \infty \tag{B.8}$$

The problem presented at higher frequencies was known as the ultraviolet catastrophe, and was solved by Max Planck who theorized that the energies of the oscillation modes were quantized and therefore had allowed energies, E_n, equal to a multiple of the energy of a single photon,

$$E_n = nhf \tag{B.9}$$

where n is a positive integer and h is Planck's constant, equal to $6.62607015 \times 10^{-34}[\mathrm{J}\cdot\mathrm{s}]$.

Let $p(n)$ be the expected number of modes with energy E_n. Therefore, the average energy, U, due to the radiation contained in the box is

$$U = \sum_{n=0}^{\infty} E_n p(n) \tag{B.10}$$

From Boltzmann statistics, $p(n)$ is

$$p(n) = \frac{e^{-\beta E_n}}{Z} \tag{B.11}$$

where $\beta = (kT)^{-1}$ and Z is the partition function given by

$$Z = \sum_{n=0}^{\infty} e^{-\beta E_n} \tag{B.12}$$

Inserting Equations (B.11) and (B.12) into (B.10) produces

$$\begin{aligned}
U &= \frac{\sum_{n=0}^{\infty} E_n e^{-\beta E_n}}{\sum_{n=0}^{\infty} e^{-\beta E_n}} \\
&= \frac{\sum_{n=0}^{\infty} nhf e^{-\beta nhf}}{\sum_{n=0}^{\infty} e^{-\beta nhf}} \\
&= hf \frac{\sum_{n=0}^{\infty} n x^n}{\sum_{n=0}^{\infty} x^n}
\end{aligned} \tag{B.13}$$

where $x = e^{-hf\beta}$. There are now two infinite series that evaluate to the following finite expressions:

$$\sum_{n=0}^{\infty} x^n = \frac{1}{1-x} \tag{B.14}$$

and

$$\sum_{n=0}^{\infty} n x^n = \frac{x}{(x-1)^2} \tag{B.15}$$

Substituting these forms into Equation (B.13) gives

$$\begin{aligned}
U &= hf(1-x)\frac{x}{(x-1)^2} \\
&= hf\frac{x}{1-x} \\
&= \frac{hf}{x^{-1}-1} \\
&= \frac{hf}{e^{hf\beta}-1}
\end{aligned} \tag{B.16}$$

Now, the energy density in the box, assuming quantized energy levels, is the result of multiplying the density of modes given by Equations (B.6) by the average energy of each mode given by (B.16),

$$u(f) = \frac{8\pi h f^3}{c^3} \frac{1}{e^{hf/kT} - 1} \left[\frac{\text{J}}{\text{m}^3 \cdot \text{Hz}} \right] \tag{B.17}$$

Planck's solution to the energy density within the box no longer blows up at large frequencies, thereby solving the ultraviolet catastrophe. Instead, integrating the energy density over all frequencies results in

$$\int_0^\infty u(f)\mathrm{d}f \propto T^4 \tag{B.18}$$

as predicted by the Stefan-Boltzmann law.

Next, consider a small hole in the box which allows the light inside the box to radiate isotropically. Let $B_f(T)$ be the radiant energy that is emitted from this hole for light in the frequency interval f to $f + \mathrm{d}f$. B_f, is the quantity which describes radiation from energy density, $u(f)$, travelling with speed, c, in a direction. Therefore,

$$B_f(T) = u(f) \times c \times \frac{1}{4\pi} \tag{B.19}$$

where division by 4π accounts for the isotropic distribution of the radiation from the source point. Inserting the expression for $u(f)$ from Equation (B.17) produces the frequency form of Planck's law,

$$B_f(T) = \frac{2h f^3}{c^2} \frac{1}{e^{hf/kT} - 1} \left[\frac{\text{W}}{\text{sr} \cdot \text{m}^2 \cdot \text{Hz}} \right] \tag{B.20}$$

Planck's law may also be written in terms of wavelength or wavenumber, however it is important to remember that B_f applies to a frequency interval $\mathrm{d}f$. Therefore, the corresponding wavenumber form, B_ν, and wavelength form, B_λ, are given given by

$$B_f\mathrm{d}f = B_\nu\mathrm{d}\nu,$$
$$B_f\mathrm{d}f = -B_\lambda\mathrm{d}\lambda \tag{B.21}$$

Note that a negative sign is introduced when converting to wavelength because λ decreases as f increases. The following expressions relating the spectral quantities are obtained from their definitions:

$$f = c\nu \implies \mathrm{d}f = c\mathrm{d}\nu,$$
$$f = \frac{c}{\lambda} \implies \mathrm{d}f = -\frac{c}{\lambda^2}\mathrm{d}\lambda \tag{B.22}$$

Substituting the wavenumber conversions into Equation (B.20) gives

$$B_\nu(T) = 2hc^2\nu^3 \frac{1}{e^{hc\nu/kT} - 1} \quad \left[\frac{\text{W}}{\text{sr} \cdot \text{m}^2 \cdot \text{m}^{-1}}\right] \tag{B.23}$$

Similarly, the wavelength version of the Planck function is found to be

$$B_\lambda(T) = \frac{2hc^2}{\lambda^5} \frac{1}{e^{hc/\lambda kT} - 1} \quad \left[\frac{\text{W}}{\text{sr} \cdot \text{m}^2 \cdot \text{m}}\right] \tag{B.24}$$

Additionally, B_λ can be expressed in terms of the photon flux per unit area and unit solid angle by dividing by the photon energy, hc/λ, resulting in

$$B_{\lambda,\text{photon}}(T) = \frac{2c}{\lambda^4} \frac{1}{e^{hc/\lambda kT} - 1} \quad \left[\frac{\text{photon}}{\text{s} \cdot \text{sr} \cdot \text{m}^2 \cdot \text{m}}\right] \tag{B.25}$$